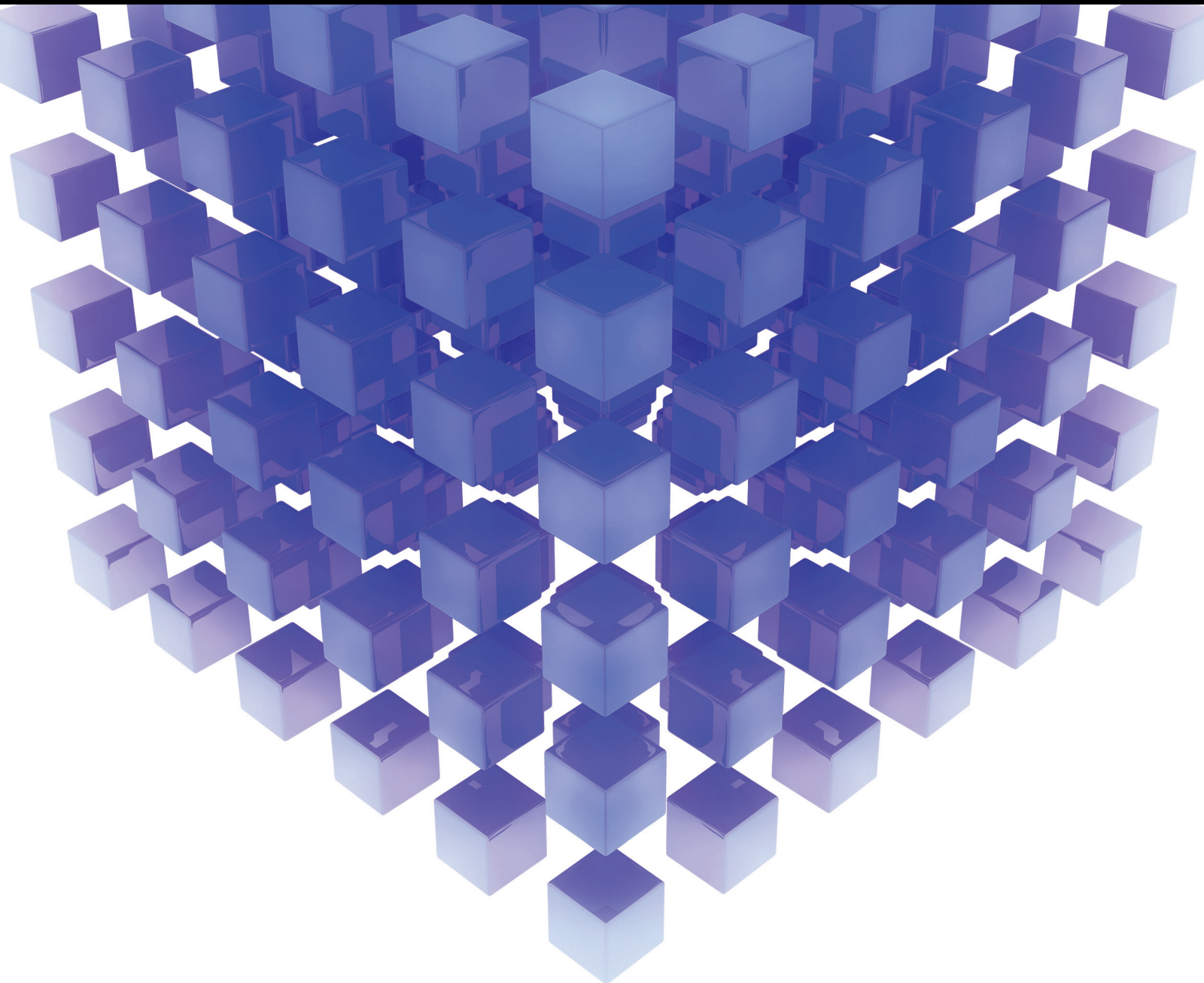


Mathematical Problems in Engineering

Optimization with Surrogate Models: Flow and Heat Transfer Applications

Lead Guest Editor: Arshad Afzal

Guest Editors: Kwang-Yong Kim, Krishnamurty Muralidhar, Abdus Samad,
and Ernesto Benini





Optimization with Surrogate Models: Flow and Heat Transfer Applications

Mathematical Problems in Engineering

Optimization with Surrogate Models: Flow and Heat Transfer Applications

Lead Guest Editor: Arshad Afzal

Guest Editors: Kwang-Yong Kim, Krishnamurty Muralidhar,
Abdus Samad, and Ernesto Benini



Copyright © 2019 Hindawi. All rights reserved.

This is a special issue published in “Mathematical Problems in Engineering.” All articles are open access articles distributed under the Creative Commons Attribution License, which permits unrestricted use, distribution, and reproduction in any medium, provided the original work is properly cited.

Editorial Board

- Mohamed Abd El Aziz, Egypt
AITOUCHE Abdelouhab, France
Leonardo Acho, Spain
José A. Acosta, Spain
Daniela Addressi, Italy
Paolo Adesso, Italy
Claudia Adduce, Italy
Ramesh Agarwal, USA
Francesco Aggogeri, Italy
Juan C. Agüero, Australia
Ricardo Aguilar-Lopez, Mexico
Tarek Ahmed-Ali, France
Elias Aifantis, USA
Muhammad N. Akram, Norway
Guido Ala, Italy
Andrea Alaimo, Italy
Reza Alam, USA
Nicholas Alexander, UK
Salvatore Alfonzetti, Italy
Mohammad D. Aliyu, Canada
Juan A. Almendral, Spain
José Domingo Álvarez, Spain
Cláudio Alves, Portugal
J. P. Amezcua-Sanchez, Mexico
Lionel Amodeo, France
Sebastian Anita, Romania
Renata Archetti, Italy
Felice Arena, Italy
Sabri Arik, Turkey
Francesco Aristodemo, Italy
Fausto Arpino, Italy
Alessandro Arsie, USA
Edoardo Artioli, Italy
Fumihiko Ashida, Japan
Farhad Aslani, Australia
Mohsen Asle Zaem, USA
Romain Aubry, USA
Matteo Aureli, USA
Richard I. Avery, USA
Viktor Avrutin, Germany
Francesco Aymerich, Italy
Sajad Azizi, Belgium
Michele Baccocchi, Italy
Seungik Baek, USA
Adil Bagirov, Australia
Khaled Bahlali, France
Laurent Bako, France
Pedro Balaguer, Spain
Stefan Balint, Romania
Ines Tejado Balsera, Spain
Alfonso Banos, Spain
Jerzy Baranowski, Poland
Roberto Baratti, Italy
Andrzej Bartoszewicz, Poland
David Bassir, France
Chiara Bedon, Italy
Azeddine Beghdadi, France
Denis Benasciutti, Italy
Ivano Benedetti, Italy
Rosa M. Benito, Spain
Elena Benvenuti, Italy
Giovanni Berselli, Italy
Giorgio Besagni, Italy
Michele Betti, Italy
Jean-Charles Beugnot, France
Pietro Bia, Italy
Carlo Bianca, France
Simone Bianco, Italy
Vincenzo Bianco, Italy
Vittorio Bianco, Italy
Gennaro N. Bifulco, Italy
David Bigaud, France
Antonio Bilotta, Italy
Paul Bogdan, USA
Guido Bolognesi, UK
Rodolfo Bontempo, Italy
Alberto Borboni, Italy
Paolo Boscariol, Italy
Daniela Boso, Italy
Guillermo Botella-Juan, Spain
Boulaïd Boulkroune, Belgium
Fabio Bovenga, Italy
Francesco Braghin, Italy
Ricardo Branco, Portugal
Maurizio Brocchini, Italy
Julien Bruchon, France
Matteo Bruggi, Italy
Michele Brun, Italy
Vasilis Burganos, Greece
Tito Busani, USA
Raquel Caballero-Águila, Spain
Filippo Cacace, Italy
Pierfrancesco Cacciola, UK
Salvatore Caddemi, Italy
Roberto Caldelli, Italy
Alberto Campagnolo, Italy
Eric Campos-Canton, Mexico
Marko Canadija, Croatia
Salvatore Cannella, Italy
Francesco Cannizzaro, Italy
Javier Cara, Spain
Ana Carpio, Spain
Caterina Casavola, Italy
Sara Casciati, Italy
Federica Caselli, Italy
Carmen Castillo, Spain
Inmaculada T. Castro, Spain
Miguel Castro, Portugal
Giuseppe Catalanotti, UK
Nicola Caterino, Italy
Alberto Cavallo, Italy
Gabriele Cazzulani, Italy
Luis Cea, Spain
Song Cen, China
Miguel Cerrolaza, Venezuela
M. Chadli, France
Gregory Chagnon, France
Ludovic Chamoin, France
Ching-Ter Chang, Taiwan
Qing Chang, USA
Michael J. Chappell, UK
Kacem Chehdi, France
Peter N. Cheimets, USA
Xinkai Chen, Japan
Luca Chiapponi, Italy
Francisco Chicano, Spain
Nicholas Chileshe, Australia
Adrian Chmielewski, Poland
Ioannis T. Christou, Greece
Hung-Yuan Chung, Taiwan
Simone Cinquemani, Italy
Roberto G. Citarella, Italy

Joaquim Ciurana, Spain
John D. Clayton, USA
Francesco Clementi, Italy
Piero Colajanni, Italy
Giuseppina Colicchio, Italy
Vassilios Constantoudis, Greece
Enrico Conte, Italy
Francesco Conte, Italy
Alessandro Contento, USA
Mario Cools, Belgium
José A. Correia, Portugal
Jean-Pierre Corriou, France
J.-C. Cortés, Spain
Carlo Cosentino, Italy
Paolo Crippa, Italy
Andrea Crivellini, Italy
F. R. B. Cruz, Brazil
Erik Cuevas, Mexico
Maria C. Cunha, Portugal
Peter Dabnichki, Australia
Luca D'Acierno, Italy
Weizhong Dai, USA
Andrea Dall'Asta, Italy
Purushothaman Damodaran, USA
Bhabani S. Dandapat, India
Farhang Daneshmand, Canada
Giuseppe D'Aniello, Italy
Sergey Dashkovskiy, Germany
Fabio De Angelis, Italy
Samuele De Bartolo, Italy
Abílio De Jesus, Portugal
Pietro De Lellis, Italy
Alessandro De Luca, Italy
Stefano de Miranda, Italy
Filippo de Monte, Italy
M. do Rosário de Pinho, Portugal
Michael Defoort, France
Alessandro Della Corte, Italy
Xavier Delorme, France
Laurent Dewasme, Belgium
Angelo Di Egidio, Italy
Roberta Di Pace, Italy
Ramón I. Diego, Spain
Yannis Dimakopoulos, Greece
Zhengtao Ding, UK
M. Djemai, France
Alexandre B. Dolgui, France

Georgios Dounias, Greece
Florent Duchaine, France
George S. Dulikravich, USA
Bogdan Dumitrescu, Romania
Horst Ecker, Austria
Saeed Eftekhari Azam, USA
Ahmed El Hajjaji, France
Antonio Elipe, Spain
Fouad Erchiqui, Canada
Anders Eriksson, Sweden
R. Emre Erkmen, Canada
G. Espinosa-Paredes, Mexico
Leandro F. F. Miguel, Brazil
Andrea L. Facci, Italy
Giacomo Falcucci, Italy
Giovanni Falsone, Italy
Hua Fan, China
Nicholas Fantuzzi, Italy
Yann Favennec, France
Fiorenzo A. Fazzolari, UK
Giuseppe Fedele, Italy
Roberto Fedele, Italy
Arturo J. Fernández, Spain
Jesus M. Fernandez Oro, Spain
Massimiliano Ferraioli, Italy
Massimiliano Ferrara, Italy
Francesco Ferrise, Italy
Eric Feulvarch, France
Barak Fishbain, Israel
S. Douwe Flapper, Netherlands
Thierry Floquet, France
Eric Florentin, France
Alessandro Formisano, Italy
Francesco Franco, Italy
Elisa Francomano, Italy
Tomonari Furukawa, USA
Juan C. G. Prada, Spain
Mohamed Gadala, Canada
Matteo Gaeta, Italy
Mauro Gaggero, Italy
Zoran Gajic, USA
Erez Gal, Israel
J. Gallardo-Alvarado, Mexico
Ugo Galvanetto, Italy
Akemi Gálvez, Spain
Rita Gamberini, Italy
Maria L. Gandarias, Spain

Arman Ganji, Canada
Zhiwei Gao, UK
Zhong-Ke Gao, China
Giovanni Garcea, Italy
Luis Rodolfo Garcia Carrillo, USA
Jose M. Garcia-Aznar, Spain
Akhil Garg, China
Alessandro Gasparetto, Italy
Gianluca Gatti, Italy
Oleg V. Gendelman, Israel
Stylianos Georgantzinou, Greece
Fotios Georgiades, UK
Parviz Ghadimi, Iran
Mergen H. Ghayesh, Australia
Georgios I. Giannopoulos, Greece
Agathoklis Giaralis, UK
Pablo Gil, Spain
Anna M. Gil-Lafuente, Spain
Ivan Giorgio, Italy
Gaetano Giunta, Luxembourg
Alessio Gizzi, Italy
Jefferson L.M.A. Gomes, UK
Emilio Gómez-Déniz, Spain
Antonio M. Gonçalves de Lima, Brazil
David González, Spain
Chris Goodrich, USA
Rama S. R. Gorla, USA
Kannan Govindan, Denmark
Antoine Grall, France
George A. Gravvanis, Greece
Fabrizio Greco, Italy
David Greiner, Spain
Simonetta Grilli, Italy
Jason Gu, Canada
Federico Guarracino, Italy
Michele Guida, Italy
Zhaoxia Guo, China
José L. Guzmán, Spain
Quang Phuc Ha, Australia
Petr Hájek, Czech Republic
Weimin Han, USA
Zhen-Lai Han, China
Thomas Hanne, Switzerland
Mohammad A. Hariri-Ardebili, USA
Xiao-Qiao He, China
Luca Heltai, Italy
Nicolae Herisanu, Romania

Alfredo G. Hernández-Díaz, Spain	Nam-Il Kim, Republic of Korea	Ezequiel López-Rubio, Spain
M.I. Herreros, Spain	Jan Koci, Czech Republic	Vassilios C. Loukopoulos, Greece
Eckhard Hitzer, Japan	Ioannis Kostavelis, Greece	Jose A. Lozano-Galant, Spain
Paul Honeine, France	Sotiris B. Kotsiantis, Greece	haiyan Lu, Australia
Jaromir Horacek, Czech Republic	Manfred Krafczyk, Germany	Gabriel Luque, Spain
Muneo Hori, Japan	Frederic Kratz, France	Valentin Lychagin, Norway
András Horváth, Italy	Petr Krysl, USA	Antonio Madeo, Italy
S. Hassan Hosseinnia, Netherlands	Krzysztof S. Kulpa, Poland	José María Maestre, Spain
Gordon Huang, Canada	Shailesh I. Kundalwal, India	Alessandro Magnani, Italy
Sajid Hussain, Canada	Jurgen Kurths, Germany	Fazal M. Mahomed, South Africa
Asier Ibeas, Spain	Cedrick A. K. Kwimiy, USA	Noureddine Manamanni, France
Orest V. Iftime, Netherlands	Kyandoghere Kyamakya, Austria	Paolo Manfredi, Italy
Przemyslaw Ignaciuk, Poland	Davide La Torre, Italy	Didier Maquin, France
Giacomo Innocenti, Italy	Risto Lahdelma, Finland	Giuseppe Carlo Marano, Italy
Emilio Insfran Pelozo, Spain	Hak-Keung Lam, UK	Damijan Markovic, France
Alessio Ishizaka, UK	Giovanni Lancioni, Italy	Francesco Marotti de Sciarra, Italy
Nazrul Islam, USA	Jimmy Lauber, France	Rui Cunha Marques, Portugal
Benoit Iung, France	Antonino Laudani, Italy	Rodrigo Martínez-Bejar, Spain
Benjamin Ivorra, Spain	Hervé Laurent, France	Guiomar Martín-Herrán, Spain
Payman Jalali, Finland	Aimé Lay-Ekuakille, Italy	Denizar Cruz Martins, Brazil
Mahdi Jalili, Australia	Nicolas J. Leconte, France	Benoit Marx, France
Łukasz Jankowski, Poland	Dimitri Lefebvre, France	Elio Masciari, Italy
Samuel N. Jator, USA	Eric Lefevre, France	Franck Massa, France
Juan C. Jauregui-Correa, Mexico	Marek Lefik, Poland	Paolo Massioni, France
Reza Jazar, Australia	Yaguo Lei, China	Alessandro Mauro, Italy
Khalide Jbilou, France	Kauko Leiviskä, Finland	Fabio Mazza, Italy
Piotr Jędrzejowicz, Poland	Thibault Lemaire, France	Laura Mazzola, Italy
Isabel S. Jesus, Portugal	Roman Lewandowski, Poland	Driss Mehdi, France
Linni Jian, China	Chen-Feng Li, China	Roderick Melnik, Canada
Bin Jiang, China	Jian Li, USA	Pasquale Memmolo, Italy
Zhongping Jiang, USA	Yang Li, China	Xiangyu Meng, USA
Emilio Jiménez Macías, Spain	Huchang Liao, China	Jose Merodio, Spain
Ningde Jin, China	En-Qiang Lin, USA	Alessio Merola, Italy
Xiaoliang Jin, USA	Zhiyun Lin, China	Mahmoud Mesbah, Iran
Liang Jing, Canada	Peide Liu, China	Luciano Mescia, Italy
Dylan F. Jones, UK	Peter Liu, Taiwan	Laurent Mevel, France
Palle E. Jorgensen, USA	Wanquan Liu, Australia	Mariusz Michta, Poland
Vyacheslav Kalashnikov, Mexico	Bonifacio Llamazares, Spain	Aki Mikkola, Finland
Tamas Kalmar-Nagy, Hungary	Alessandro Lo Schiavo, Italy	Giovanni Minafò, Italy
Tomasz Kapitaniak, Poland	Jean Jacques Loiseau, France	Hiroyuki Mino, Japan
Julius Kaplunov, UK	Francesco Lolli, Italy	Pablo Mira, Spain
Haranath Kar, India	Paolo Lonetti, Italy	Dimitrios Mitsotakis, New Zealand
Konstantinos Karamanos, Belgium	Sandro Longo, Italy	Vito Mocella, Italy
Krzysztof Kecik, Poland	António M. Lopes, Portugal	Sara Montagna, Italy
Jean-Pierre Kenne, Canada	Sebastian López, Spain	Roberto Montanini, Italy
Ch. M. Khaliq, South Africa	Pablo Lopez-Crespo, Spain	Francisco J. Montáns, Spain
Do Wan Kim, Republic of Korea	Luis M. López-Ochoa, Spain	Luiz H. A. Monteiro, Brazil

Gisele Mophou, France
Rafael Morales, Spain
Marco Morandini, Italy
Javier Moreno-Valenzuela, Mexico
Simone Morganti, Italy
Caroline Mota, Brazil
Aziz Moukrim, France
Dimitris Mourtzis, Greece
Emiliano Mucchi, Italy
Josefa Mula, Spain
Jose J. Muñoz, Spain
Giuseppe Muscolino, Italy
Marco Mussetta, Italy
Hakim Naceur, France
Alessandro Naddeo, Italy
Hassane Naji, France
Mariko Nakano-Miyatake, Mexico
Keivan Navaie, UK
AMA Neves, Portugal
Luís C. Neves, UK
Dong Ngoduy, New Zealand
Nhon Nguyen-Thanh, Singapore
Tatsushi Nishi, Japan
Xesús Nogueira, Spain
Ben T. Nohara, Japan
Mohammed Nouari, France
Mustapha Nourelfath, Canada
Włodzimierz Ogryczak, Poland
Roger Ohayon, France
Krzysztof Okarma, Poland
Mitsuhiro Okayasu, Japan
Alberto Olivares, Spain
Enrique Onieva, Spain
Calogero Orlando, Italy
Alejandro Ortega-Moñux, Spain
Sergio Ortobelli, Italy
Naohisa Otsuka, Japan
Erika Ottaviano, Italy
Pawel Packo, Poland
Arturo Pagano, Italy
Alkis S. Paipetis, Greece
Roberto Palma, Spain
Alessandro Palmeri, UK
Pasquale Palumbo, Italy
Weifeng Pan, China
Jürgen Pannek, Germany
Elena Panteley, France
Achille Paolone, Italy
George A. Papakostas, Greece
Xosé M. Pardo, Spain
Vicente Parra-Vega, Mexico
Manuel Pastor, Spain
Petr Páta, Czech Republic
Pubudu N. Pathirana, Australia
Surajit Kumar Paul, India
Sitek Paweł, Poland
Luis Payá, Spain
Alexander Paz, Australia
Igor Pažanin, Croatia
Libor Pekař, Czech Republic
Francesco Pellicano, Italy
Marcello Pellicciari, Italy
Haipeng Peng, China
Mingshu Peng, China
Zhengbiao Peng, Australia
Zhi-ke Peng, China
Marzio Pennisi, Italy
Maria Patrizia Pera, Italy
Matjaz Perc, Slovenia
A. M. Bastos Pereira, Portugal
Ricardo Perera, Spain
Francesco Pesavento, Italy
Ivo Petras, Slovakia
Francesco Petrini, Italy
Lukasz Pieczonka, Poland
Dario Piga, Switzerland
Paulo M. Pimenta, Brazil
Antonina Pirrotta, Italy
Marco Pizzarelli, Italy
Vicent Pla, Spain
Javier Plaza, Spain
Kemal Polat, Turkey
Dragan Poljak, Croatia
Jorge Pomares, Spain
Sébastien Poncet, Canada
Volodymyr Ponomaryov, Mexico
Jean-Christophe Ponsart, France
Mauro Pontani, Italy
Cornelio Posadas-Castillo, Mexico
Francesc Pozo, Spain
Christopher Pretty, New Zealand
Luca Pugi, Italy
Krzysztof Puszynski, Poland
Giuseppe Quaranta, Italy
Vitomir Racic, Italy
Jose Ragot, France
Carlo Rainieri, Italy
Kumbakonam Ramamani Rajagopal, USA
Ali Ramazani, USA
Higinio Ramos, Spain
Alain Rassinoux, France
S.S. Ravindran, USA
Alessandro Reali, Italy
Jose A. Reinoso, Spain
Oscar Reinoso, Spain
Fabrizio Renno, Italy
Nidhal Rezg, France
Ricardo Riaza, Spain
Francesco Riganti-Fulginei, Italy
Gerasimos Rigatos, Greece
Francesco Ripamonti, Italy
Jorge Rivera, Mexico
Eugenio Roanes-Lozano, Spain
Bruno G. M. Robert, France
Ana Maria A. C. Rocha, Portugal
José Rodellar, Spain
Luigi Rodino, Italy
Rosana Rodríguez López, Spain
Ignacio Rojas, Spain
Alessandra Romolo, Italy
Debasish Roy, India
Gianluigi Rozza, Italy
Jose de Jesus Rubio, Mexico
Rubén Ruiz, Spain
Antonio Ruiz-Cortes, Spain
Ivan D. Rukhlenko, Australia
Mazen Saad, France
Kishin Sadarangani, Spain
Andrés Sáez, Spain
Mehrdad Saif, Canada
John S. Sakellariou, Greece
Salvatore Salamone, USA
Vicente Salas, Spain
Jose Vicente Salcedo, Spain
Nunzio Salerno, Italy
Miguel A. Salido, Spain
Roque J. Saltarén, Spain
Alessandro Salvini, Italy
Sylwester Samborski, Poland
Ramon Sancibrian, Spain
Giuseppe Sanfilippo, Italy

Vittorio Sansalone, France
José A. Sanz-Herrera, Spain
Nickolas S. Sapidis, Greece
Evangelos J. Sapountzakis, Greece
Luis Saucedo-Mora, Spain
Marcelo A. Savi, Brazil
Andrey V. Savkin, Australia
Roberta Sbulati, Italy
Gustavo Scaglia, Argentina
Thomas Schuster, Germany
Oliver Schütze, Mexico
Lotfi Senhadji, France
Junwon Seo, USA
Joan Serra-Sagrsta, Spain
Gerardo Severino, Italy
Ruben Sevilla, UK
Stefano Sfarra, Italy
Mohamed Shaat, Egypt
Mostafa S. Shadloo, France
Leonid Shaikhet, Israel
Hassan M. Shanechi, USA
Bo Shen, Germany
Suzanne M. Shontz, USA
Babak Shotorban, USA
Zhan Shu, UK
Nuno Simões, Portugal
Christos H. Skiadas, Greece
Konstantina Skouri, Greece
Neale R. Smith, Mexico
Bogdan Smolka, Poland
Delfim Soares Jr., Brazil
Alba Sofi, Italy
Francesco Soldovieri, Italy
Raffaele Solimene, Italy
Jussi Sopanen, Finland
Marco Spadini, Italy
Bernardo Spagnolo, Italy
Paolo Spagnolo, Italy
Ruben Specogna, Italy
Vasilios Spitas, Greece
Sri Sridharan, USA
Ivanka Stamova, USA
Rafał Stanisławski, Poland
Florin Stoican, Romania
Salvatore Strano, Italy
Yakov Strelniker, Israel
Guangyong Sun, China
Ning Sun, China
Sergey A. Suslov, Australia
Thomas Svensson, Sweden
Andrzej Swierniak, Poland
Andras Szekrenyes, Hungary
Kumar K. Tamma, USA
Yang Tang, Germany
Hafez Tari, USA
Alessandro Tasora, Italy
Sergio Teggi, Italy
Ana C. Teodoro, Portugal
Alexander Timokha, Norway
Gisella Tomasini, Italy
Francesco Tornabene, Italy
Antonio Tornambe, Italy
Javier Martinez Torres, Spain
Mariano Torrisi, Italy
George Tsiatas, Greece
Antonios Tsourdos, UK
Federica Tubino, Italy
Nerio Tullini, Italy
Andrea Tundis, Italy
Emilio Turco, Italy
Mustafa Tutar, Spain
Ilhan Tuzcu, USA
Efstratios Tzirtzilakis, Greece
Filippo Ubertini, Italy
Francesco Ubertini, Italy
Mohammad Uddin, Australia
Hassan Ugail, UK
Giuseppe Vairo, Italy
Eusebio Valero, Spain
Pandian Vasant, Malaysia
Marcello Vasta, Italy
Carlos-Renato Vázquez, Mexico
M. E. Vázquez-Méndez, Spain
Josep Vehi, Spain
Martin Velasco Villa, Mexico
K. C. Veluvolu, Republic of Korea
Fons J. Verbeek, Netherlands
Franck J. Vernerey, USA
Georgios Veronis, USA
Vincenzo Vespri, Italy
Renato Vidoni, Italy
V. Vijayaraghavan, Australia
Anna Vila, Spain
Rafael J. Villanueva, Spain
Francisco R. Villatoro, Spain
Uchechukwu E. Vincent, UK
Gareth A. Vio, Australia
Francesca Vipiana, Italy
Stanislav Vitek, Czech Republic
Thuc P. Vo, UK
Jan Vorel, Czech Republic
Michael Wynnycky, Sweden
Hao Wang, USA
Liliang Wang, UK
Shuming Wang, China
Yongqi Wang, Germany
Roman Wan-Wendner, Austria
Jaroslaw Wąs, Poland
P.H. Wen, UK
Waldemar T. Wójcik, Poland
Changzhi Wu, Australia
Desheng D. Wu, Sweden
Hong-Yu Wu, USA
Yuqiang Wu, China
Michalis Xenos, Greece
Guangming Xie, China
Xue-Jun Xie, China
Gen Q. Xu, China
Hang Xu, China
Joseph J. Yame, France
Xinggang Yan, UK
Jixiang Yang, Canada
Mijia Yang, USA
Yongheng Yang, Denmark
Luis J. Yebra, Spain
Peng-Yeng Yin, Taiwan
Qin Yuming, China
Elena Zaitseva, Slovakia
Arkadiusz Zak, Poland
Daniel Zaldivar, Mexico
Francesco Zammori, Italy
Vittorio Zampoli, Italy
Rafał Zdunek, Poland
Ibrahim Zeid, USA
Huaguang Zhang, China
Kai Zhang, China
Qingling Zhang, China
Xianming Zhang, Australia
Xuping Zhang, Denmark
Zhao Zhang, China
Yifan Zhao, UK



Jian G. Zhou, UK
Quanxin Zhu, China

Mustapha Zidi, France
Gaetano Zizzo, Italy

Zhixiang Zou, Germany

Contents

Optimization with Surrogate Models: Flow and Heat Transfer Applications

Arshad Afzal , Kwang-Yong Kim, Krishnamurthy Muralidhar, Abdus Samad , and Ernesto Benini
Editorial (2 pages), Article ID 7194257, Volume 2019 (2019)

A Three-Dimensional Simulation of Particle Distribution in a Separator and Structure Optimization with the Statistical Approach of Taguchi Method

Jinjin Liu , Kai Liu, Tong Zhao , and Zhuofei Xu 
Research Article (10 pages), Article ID 7439245, Volume 2018 (2019)

Parameter Optimization and Prediction Model of Induction Heating for Large-Diameter Pipe

Xiurong Fang , Jia Lu, Junfeng Wang, and Jinhui Yang
Research Article (12 pages), Article ID 8430578, Volume 2018 (2019)

A Parametric Study and Optimization of an Air Conditioning System for a Heat-Loaded Room

Qinghe Yao , Hang Bai, Trevor Hocksun Kwan, and Kiwamu Kase
Research Article (10 pages), Article ID 2385691, Volume 2018 (2019)

Design Optimization of the Centrifugal Pumps via Low Fidelity Models

M. Hamid Siddique, Arshad Afzal , and Abdus Samad 
Review Article (14 pages), Article ID 3987594, Volume 2018 (2019)

Editorial

Optimization with Surrogate Models: Flow and Heat Transfer Applications

Arshad Afzal ¹, Kwang-Yong Kim,² Krishnamurthy Muralidhar,¹
Abdus Samad ³, and Ernesto Benini⁴

¹Department of Mechanical Engineering, Indian Institute of Technology Kanpur, Uttar Pradesh 208016, India

²Department of Mechanical Engineering, Inha University, Incheon 22212, Republic of Korea

³Department of Ocean Engineering, Indian Institute of Technology Madras, Chennai 600036, India

⁴Department of Industrial Engineering, Università di Padova, Padova 35131, Italy

Correspondence should be addressed to Arshad Afzal; aafzal@iitk.ac.in

Received 3 January 2019; Accepted 3 January 2019; Published 7 February 2019

Copyright © 2019 Arshad Afzal et al. This is an open access article distributed under the Creative Commons Attribution License, which permits unrestricted use, distribution, and reproduction in any medium, provided the original work is properly cited.

Optimization methods are now recognized to be vital in the design of fluid flow equipment and processes. Design optimization based on computational fluid dynamics (CFD) analysis has become a reliable tool for fluid flow and heat and mass transfer applications due to the rapid increase in computing power. However, to avoid expensive CFD simulations for entire design process, surrogate models are used to reduce the computational burden with a reliable representation of CFD data. The aim of the special issue was to bring together contributions from engineers, mathematicians, and computer scientists working on basic research and practical applications in engineering optimization. A substantial number of papers were submitted, and a total of 4 original research papers which covered the application of optimization techniques to flow and heat transfer problems are published in the special issue.

Q. Yao et al. studied an air conditioning system using Reynolds averaged Navier-Stokes equations and performed optimization to determine the optimal air supply directions that would provide the most stable velocity field and temperature distribution. However, the influence on cooling rate and energy utilization coefficient was found to be negligible. X. Fang et al. conducted parameter optimization of induction heating of large-diameter pipes based on the magnetic-thermal coupling in the heating process by sequential coupling method. The influence of heating process parameters like current frequency, current density, and air gap on the temperature of inner and outer walls of the

pipe was obtained using orthogonal arrays. The optimal parameters were obtained using neural network and genetic algorithm. J. Liu et al. conducted three-dimensional numerical simulations based on Eulerian-Lagrangian approach to investigate particles distribution in a separator. The discrete phase method (DPM) was applied to monitor the motion of particles. Based on the numerical analysis, the structure of separator was optimized using Taguchi method, and the optimal structure was evaluated based on signal-to-noise ratio (SNR).

Finally, the review paper by M. H. Siddique et al. presented the application of surrogate-based optimization in the context of turbomachines. The authors provided a brief overview of the technique along with its historical applications and trends in recent use. A substantial number of research articles were cited that involve the use of surrogate models for optimization of centrifugal pumps.

Conflicts of Interest

The editors declare that they have no conflicts of interest regarding the publication of this special issue.

Acknowledgments

We would like to take this opportunity to express our appreciation to all the authors for submitting their papers and contributing to the success of this special issue. We also

want to thank all the reviewers for dedicating their time and helping to improve the quality of the submitted papers and professional staff at Mathematical Problems in Engineering Editorial office for providing invaluable assistance.

Arshad Afzal
Kwang-Yong Kim
Krishnamurthy Muralidhar
Abdus Samad
Ernesto Benini

Research Article

A Three-Dimensional Simulation of Particle Distribution in a Separator and Structure Optimization with the Statistical Approach of Taguchi Method

Jinjin Liu ¹, Kai Liu,¹ Tong Zhao ¹ and Zhuofei Xu ²

¹School of Mechanical and Precision Instrument Engineering, Xi'an University of Technology, Xi'an 710048, China

²Faculty of Printing Packaging Engineering and Digital Media Technology, Xi'an University of Technology, Xi'an 710048, China

Correspondence should be addressed to Tong Zhao; tongzhao@xaut.edu.cn

Received 4 June 2018; Revised 16 October 2018; Accepted 24 October 2018; Published 27 November 2018

Guest Editor: Arshad Afzal

Copyright © 2018 Jinjin Liu et al. This is an open access article distributed under the Creative Commons Attribution License, which permits unrestricted use, distribution, and reproduction in any medium, provided the original work is properly cited.

A three-dimensional numerical simulation combining discrete phase method (DPM) and porous media based on the theory of Euler-Lagrange has been employed to investigate particles distribution in a separator. The DPM model is applied to monitor the movement of individual particles and calculate the contact force between them in the separator. The simulation results display the migration feature of dust particles over time and the distribution of particles on the surface element in porous region and reveal that the flow field influences the distribution uniformity of the particles in porous area directly. Based on the analysis, the structure of separator is optimized by the Taguchi method. An orthogonal relation motion has been established. The optimal solution is achieved by the calculation of the weight relationship. The calculated optimal structure is evaluated by the signal to noise (SNR). The result reveals that the values of SNR in case are eligible. As a result, the research of the separator points out a useful and improvable method for the parameter optimization of structure design.

1. Introduction

Coal, as the primal fossil fuel, has played an important role in national economy, such as the areas of electricity, heating, and transportation. Coal resource can be divided into high rank coal and low rank coal. Among them, low rank coal is not only characterized by the high moisture content but also the high volatility which can cause an explosion easily [1]. Meanwhile, high temperature gas containing dust is generated during burning, which causes serious pollution. Therefore, particles elimination is necessary before blowdown. Separator is important equipment in the filtration and removal process of low rank coal. Its core component is the filter core, which has the characteristics of a high temperature resistance and pressure resistance, strong corrosion resistance, and high filtration efficiency.

In this paper, multiphase flow model is chosen for simulation analysis of the model combined with computational fluid dynamics (CFD). The commonly used mathematical models that have been raised so far can be grouped into

two categories: one is the continuum-continuum approach, as represented by Euler-Euler model [2, 3], and the other is the continuum discrete approach [4] represented by the Euler-Lagrange model. The flow field of gas is treated as a continuum phase by Navies-Stokes equations in computational cell scale while the flow field of particles is treated as a discrete phase based on DPM. The physical status of individual particles, such as the trajectory in space, is obtained by the calculation of continuum phase of the air. A two-phase model of gas-solid flow is used to simulate the coupling of porous media module.

Many scholars have studied the porous media model in the different structure. Wu [5] and Boysen [6] simulated the process of adsorption in porous. Yu Liming et al. [7] used CFD-DEM to simulate the process of pressure variation during filtration process. Wang et al. [8] researched the separation efficiency of particles with different sizes in the gas-solid flow. Zhao Tong et al. [9] researched the gas-solid flow whose particle movement and distribution are in a down-flow fluidized bed with CFD-DEM. M. Haim et al.

[10] researched the particle-gas flows whose effect of the inlet conditions is on the numerical solutions. Xi Gao et al. [11] made a research on the evaluation of an enhanced filtered drag model compared with other eight different drag models in the three-dimensional simulations of gas-solid fluidized beds.

However, minimum studies considered the more uniformity of particles in porous media by optimizing the structural parameters. Optimization design methods have used various metaheuristics such as nonlinear search optimization [12], the Taguchi method.

The Taguchi method has been proposed by Genichi Taguchi [13, 14] and widely used in many fields. Rout [15] applied the Taguchi method to find the optimal setting of parameters in a manipulator and increase the positional accuracy. T. Mothilal et al. [16] applied the Taguchi method to optimize the operational parameters including the solid particle diameter, inlet air velocity, and inlet air temperature in a cyclone separator.

In summary, the paper is organized as follows: Section 2 introduces the basic theory of CFD, Euler-Lagrange Model, and the porous medium model as well; then the result of numerical simulation is discussed in a three-dimensional model of separator such as the migration distribution diagram of particles over time and the velocity distribution in filter area. Section 3 evaluates the model by using the statistics method of Taguchi to determine the weight of different structure parameters and get an effective improved plan.

2. The Approach of Modeling

2.1. Computational Fluid Theory. Computational fluid dynamics method is used in this study. Its basic approach is dividing the continuous physics region into discrete. Based on the Navier-Stokes equations, the fluid domain is calculated to obtain the key physical parameters of heated air such as speed, temperature, pressure, and flow positions.

The flow condition can be judged from the Reynolds number. The turbulence model is selected which includes the conversation laws of mass, momentum, and energy. The turbulence equation should be considered. Thus k- ϵ model is taken as follows:

$$\frac{\partial(\rho k)}{\partial t} + \frac{\partial(\rho k u_i)}{\partial x_i} = \frac{\partial}{\partial x_j} \left[\left(\mu + \frac{\mu}{\sigma_k} \right) \frac{\partial k}{\partial x_j} \right] + G_k + G_b - \rho \epsilon - Y_M + S_k \quad (1)$$

$$\frac{\partial(\rho \epsilon)}{\partial t} + \frac{\partial(\rho \epsilon u_i)}{\partial x_i} = \frac{\partial}{\partial x_j} \left[\left(\mu + \frac{\mu}{\sigma_k} \right) \frac{\partial k}{\partial x_j} \right] + G_{1\epsilon} \frac{\epsilon}{k} \cdot (G_k + C_{3\epsilon} G_b) - G_{2\epsilon} \rho \frac{\epsilon^2}{k} + S_\epsilon \quad (2)$$

Here k is turbulent kinetic energy in (1) and (2). ϵ means the dissipation rating. And we can know that G_k and G_b are the turbulent kinetic energy generation introduced by mean velocity gradient and buoyancy. Y_M is the contribution in the turbulent pulsating pressure expansion. $C_{1\epsilon}$, $C_{2\epsilon}$, and $C_{3\epsilon}$ are

empirical constants. σ_k and σ_ϵ are Prandtl numbers to k and ϵ correspondingly. S_k and S_ϵ are user defined options.

2.2. The Porous Medium Model. The filter area in separator needs to be calculated with model of porous media which is defined as laminar. A flow resistance value is introduced. The porous medium model based on superficial velocity can simulate pressure loss. The flow resistance of porous material in the fluid domain is calculated by adding a feature in momentum equation. The feature is composed of two parts, Darcy viscous resistance terms and inertial loss terms, which is expressed as

$$S_j = - \left(\sum_{j=1}^3 D_{ij} \mu v_j + \sum_{j=1}^3 C_{ij} \frac{1}{2} \rho |v| v_j \right) \quad (3)$$

Here D_{ij} and C_{ij} is the viscous resistance and inertia loss coefficient matrix, respectively. This negative result leads to a pressure drop in the unit of porous medium. μ is the fluid viscosity coefficient. The viscous resistance and inertial resistance is calculated by the following formula (4) and (5):

$$\frac{1}{\alpha} = \frac{150 (1 - \epsilon)^2}{D_p^2 \epsilon^3} \quad (4)$$

$$C_2 = \frac{3.5 (1 - \epsilon)^2}{D_p \epsilon^3} \quad (5)$$

where D_p is the particle diameter, ϵ is the porosity, and α is the permeability.

2.3. The Coupling of Discrete Phase and Porous Medium. The particles trajectory is tracked using the DPM model. The particle motion formula is on a Lagrange coordinate system. The particles motion formula of discrete phase is shown in (6) and the inertia force is considered.

$$\frac{du_p}{dt} = F_D (u - u_p) + \frac{g_x (\rho_p - \rho)}{\rho_p} + F_x \quad (6)$$

Here up is the velocity of particle. ρ and ρ_p are the densities of the continuous and discrete phase, respectively. g_x is the acceleration of gravity in x direction; $g(\rho_p - \rho)/\rho_p$ represents the joint force of gravity and buoyancy when particle is moving; $F_D(u - u_p)$ is the air resistance acting on the particle in formula (6); and F_D represents the resistance impacting on particles in unit-mass:

$$F_D = \frac{18\mu}{\rho_p d_p^2} \frac{C_D \text{Re}}{24} \quad (7)$$

$$\text{Re} = \frac{\rho d_p |u_p - u|}{\mu} \quad (8)$$

$$C_D = a_1 + \frac{a_2}{\text{Re}} + \frac{a_3}{\text{Re}} \quad (9)$$

R_e is the relative Reynolds number and C_D is the product ratio of fluid dynamic pressure. F_D has impact

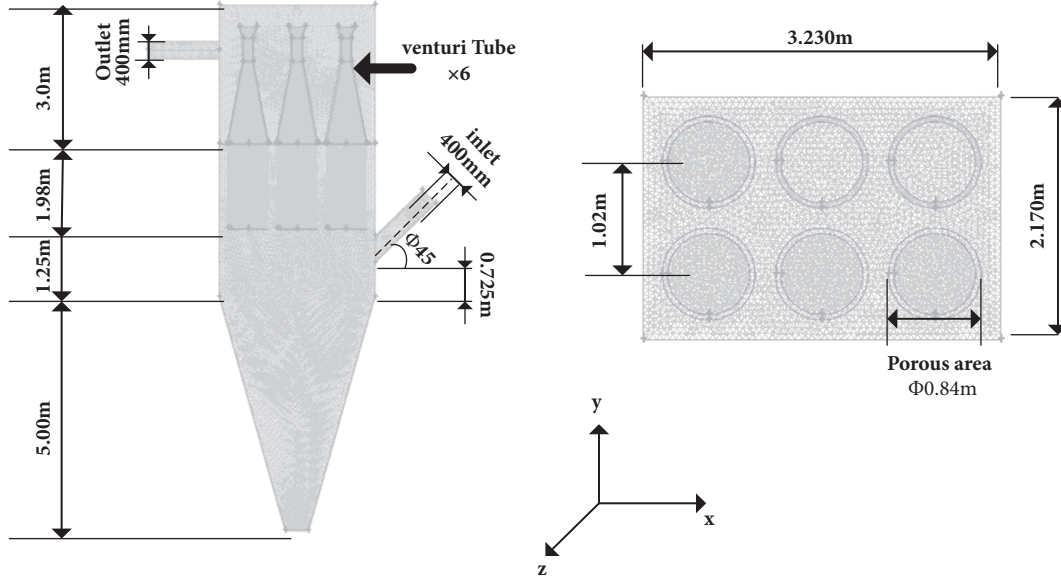


FIGURE 1: Calculation domain and grid arrangement.

on the projection which is the movement direction of the particles, namely, the drag force coefficient. d_p is the particle diameter here. The control equations of coupling model in the continuous phase, discrete phase, and porous media [17, 18] are as follows:

$$\begin{aligned} & \varepsilon (\rho C_p)_f \frac{\partial T_f}{\partial t} + (\rho C_p) \varepsilon v \nabla T_f \\ & = \varepsilon \nabla (k_f \nabla T_f) + (1 - \varepsilon) \frac{6h_f}{d} (T_s - T_f) \end{aligned} \quad (10)$$

$$\begin{aligned} & (\rho C_s) \frac{\partial T_s}{\partial t} \\ & = \nabla (k_s \nabla T_s) + \frac{6h_f}{d} (T_s - T_f) + \rho_s \sum_i \left(-\nabla H_i \frac{\partial q_i}{\partial t} \right) \end{aligned} \quad (11)$$

C_p and C_s are the specific heat at constant pressure of the continuous and discrete phase, respectively; h_f is the thermal coefficient of gas and solid phase; k_f is axial heat transfer coefficient for the gas phase; k_s is thermal conductivity coefficient for solid phase, unit for; T_f and T_s are the temperature of gas and solid phase, respectively. Here transfer rate of mass equation is used:

$$\frac{\partial q_i}{\partial t} = k_i (q_i^* - q_i) \quad (12)$$

Adsorption balance equations [19, 20] are as

$$\begin{aligned} q_i^* & = \frac{K p_i}{1 + \sum_{k=1}^N b_k P_k}, \\ K & = k_1 \exp \frac{k_2}{T_f}, k_3 \exp \frac{k_4}{T_f} \end{aligned} \quad (13)$$

k_i is the mass transfer coefficient of the component i ; q_i is the adsorption quantity for solid phase of component

i ; q^* is the maximum adsorption amount for solid phase components.

2.4. Principle and Simulation Conditions

2.4.1. Separator Principle. The computational domain and grid arrangements of the separator are shown in Figure 1. The simulation domain consists of inlet, outlet, six Venturi tubes, and inferior vena including six filter parts. The diameters of inlet and outside are both 400 mm. The angle between the centerlines of the inlet and the horizontal direction is 45° . There are six Venturi tubes in the separator. What is more, a back pulse made by vibration wave is used to reduce particles accumulated in filters elements. There are six filters in inferior vena which can be seen as porous mediums. Each filter has a diameter of 840 mm and a length of 1980 mm.

The semi-implicit method for pressure-link equation (SIMPLE) algorithm is used as the numerical method. In computational fluid dynamics, the SIMPLE algorithm is widely used to solve the Navier-Stokes equations, and it has been extensively used to solve fluid flow and heat transfer problems [21, 22]. A no-slip condition is set to the air phase on the walls. The simulation is started with the random generation of particles combined with gas phase in inlet. With the setting of gravitational force, lift force, and drag force settling, the particles enter into the inferior vena and pervade in the area of porous mediums. Finally, the part of the particles will sink into bottom; others will pass filter holes and reach the cavity Venturi tube and the export. In general we want to keep less particles away from passing through the porous area. Thus the filter will work for a longer time and not be broken easily. We hope more particles are blown down to the bottom of separator directly.

2.4.2. Simulation Conditions. Calculation domain is meshed by Gambit. The total number of meshes is 6,197,815; therefore,

TABLE 1: The parameter settings of calculation.

Gas phase	Density(kg/m ³)	1.225
	Viscosity(kg/m-s)	1.7894e-05
	Reference Temperature(k)	298.15
	Velocity Magnitude(m/s)	20
	Turbulent Intensity(%)	10
	Hydraulic Diameter(m)	0.4
Particles phase	Cp(Specific Heat)(j/kg-k)	1550
	Molecular Weight (kg/kg-mol)	17.237
	Standard State Enthalpy(j/kg-mol)	-5.601e+07
	Reference Temperature(k)	298.15
	Velocity (m/s)	20
	Turbulent Kinetic Energy	0.8
	Momentum	0.2
Porous area	Porosity	0.4
	face permeability(m ²)	1.19e-11
	Porous permeability	0.5
	Viscous Resistance	8.4e+10
	Inertial Resistance	5.1e+04

the time of calculation of the meshed model needs about 48 hours on a workstation (System is Windows 8. The processor is Xeon 1231v3. The memory is 16G). The calculation is done in Fluent 14.0 and the result is extracted by Tecplot 360 21013R1. The type of grid is chosen as tetrahedron structure. The grid density is increased appropriately in the six filter parts. The Jacobian value is positive.

In this study, we set medium volatile coal (Coal-Mv) as the particles of discrete phase in calculation. Compared with highly volatile coal (Coal-Hv) and low volatile coal (Coal-Lv), Coal-Mv is suitable for simulating most coal powders in working conditions [23]. The physical parameters are set according to the real property in Table 1.

The Rosin-Rammler model is used to describe the distribution of particle diameters in this work. The Rosin-Rammler model was first applied by Rosin-Rammler to describe a particle size distribution. The expression function of the Rosin-Rammler is described as

$$F(d) = 1 - \exp\left[-\left(\frac{d}{c}\right)^m\right] \quad (14)$$

where F is the distribution function of particles with a diameter of d. c is the characteristic diameter which is always the average diameter of particles. The exponent m is uniformity constant [24, 25].

Inlet and outlet of the mode are mentioned in Figure 1. The area of filters is defined as the laminar zone porous. Other parameters in Ansys are chosen in Table 1. In Table 1, air is simulated as gas phase while particles phase is simulated as discrete phase. Filters are represented as porous area in separator. The physical parameters are set according to the real property. As to the velocity, diameter, energy, and momentum, average values are chosen to initialize and calculate. Momentum is the subrelaxation factor in Ansys 14.0 to reduce appropriately between the calculation results of the previous layer and the later one, which could avoid the

nonlinear divergence induced by excessive difference during the iterative process.

In order to make result closer to reality, other options are set based on the real actual working conditions.

2.5. Simulation Result and Discussion. This section discusses the results of the simulation. The result positions of the three cross-sectional in porous region in Figure 2. Particle distribution in the three sections is shown in Table 2. We can find the following: (1) The particles enter into the inferior vena of separator, combined with continuous phase. Most particles cannot penetrate the porous media because there are viscous resistance and inertial resistance. (2) With the increase of time, particles slowly goes from import to inferior vena area. The number of particles gradually increases from bottom to top. Meanwhile, a large number of particles accumulated in the middle area. (3) Due to the fact that the particle phase is loaded continuously and the pressure is increased in the inferior vena, particles slowly enter into the filter which is close to inlet about the time of 23.4 s. (4) The color of the particles indicates that the particles sink slowly to bottom of separator under the effect of gravity with time increases.

Table 3 shows the velocity distribution images in three cross-sectional. These sections illustrate the flow field of continuous phase under the influence of solid phase, and solid phase affects velocity distribution of the continuous phase. Take 60 speed values in each face to calculate the mean square error for each surface and it is shown in Table 4. Y_i represents the mean square error of sample values in each cross section which is calculated as

$$Y_i = \sqrt{\frac{1}{N} \sum_{i=1}^N (x_i - \mu)^2} \quad (15)$$

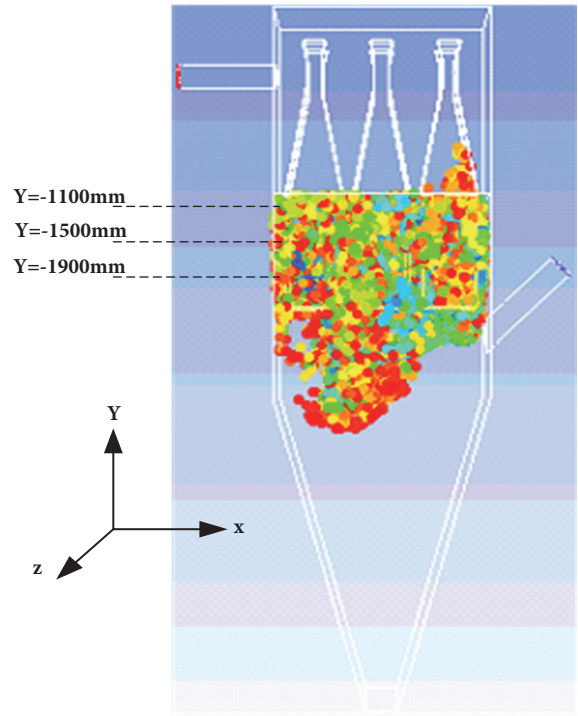


FIGURE 2: Three-dimensional particle distribution (t=286s).

TABLE 2: Particle distribution at different times.

position	Simulation result			
	T:126s	T:162s	T:198s	T:234s
Y=-1100mm				
Y=-1500mm				
Y=-1900mm				

N is the number of data point and x_i is the value of each point. μ is the average value of all data points. The mean square error of each section is relatively large.

In engineering, the replacement of filter has a high cost and complicated operation. Therefore, we hope that most particles will not penetrate filter. A large number of particles accumulated in the middle area will cause filter to

be partially stressed resulting in the aging rate of the filter, so particle should distribute uniformly in the filter to reduce the accumulation of particles partially in the filter. The particles are mainly affected by the continuous phase. Therefore, the goal of the separator structure optimization is to get a more homogeneous flow field in porous media zone. In our paper, the uniformity of flow field is evaluated by velocity and pressure.

TABLE 3: The image of velocity distribution.

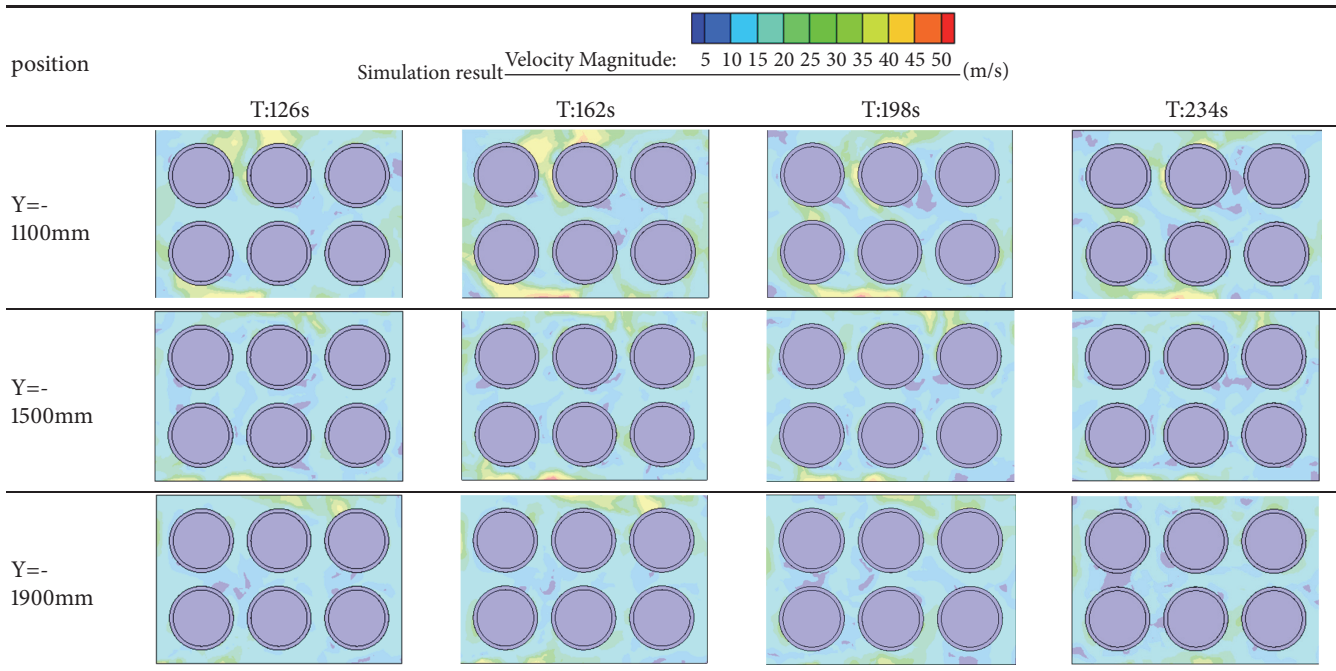


TABLE 4: The results of mean square error.

Position of section	126s	162s	198s	234s
-1100mm	10.877	9.957	9.073	8.838
-1500mm	7.886	7.852	8.083	5.441
-1900mm	6.777	6.777	5.685	6.230

3. The Optimizations of Structure for Separator

A separator model is given by an enterprise in China. Our purpose is to improve parameters about inlet and filters based on CFD. As to a separator, performance is always decided by the distribution of velocity and pressure. In ideal status, a uniform distribution of flow field means that the particle will contact the filters equivalently; therefore, all the filters play the same role. Otherwise, particles will focus on some parts of few filters which will be damaged easily. These filters may be blocked by too much concentrated particles, while an unfair distribution also means that some area of filters does not work at all. For these reasons, mean square errors of velocity and pressure are used to evaluate the result of optimization, and a smaller value means a better performance.

As to a given separator in specific working conditions, the mainframe cannot be changed, and the filter is already made according to standard; therefore, their sizes always cannot be changed. Inlet is a key part to decide the distribution of fluid field; thus both the position and inclination angle of inlet are chosen to optimize. In the inner of separator, the utilization rate of filters is decided by the installation site directly, since it is so, it cannot be neglected that the distance between two filters in the direction-Z in Figure 1. The distance-X is

neglected here to simplify the process since its result is similar to distance in direction-Z.

Based on the reasons above, three parameters are selected to optimize the model according to the mean square error from distribution of both velocity and pressure. Taguchi method is used to realize the target.

3.1. The Theory of Taguchi Method. The basic principle of the Taguchi method, avoiding the blindness of traverse type analysis, is the inspection of the effectiveness from the experimental variables which is the synthesis procedure conducted by orthogonal array with minimum number of experiments [15, 26]. This approach can obtain effectively the contribution rate and weight relations from various elements of target. The method can be used to realize the optimization and reduce test times compared to exhaustion method. The main steps of structure optimization for separator are as follows: (1) Determining the key elements of the research object, select all elements of the plan. (2) Design the orthogonal table for all combination schemes according to the relationship between elements. (3) Select the orthogonal schemes and calculate each of them. (4) According to the results, get the order of weight for all selected elements based on the contribution rate.

3.2. The Design of Orthogonal Table. In the study based on Taguchi method, to represent three parameters, we take the angle between the inlet axis and the horizontal direction as factor A, the distance between the inlet and bottom of filter as factor B, and the distance of two filters in direction-Z as factor C. Control factors and its levels are designed and shown in Table 5.

Factor A is often between 0° to 45° in actual equipment, thus 0°, 45°, and 22.5° are chosen. As to factor B and factor

TABLE 5: The statistics of element.

Factor	Level 1	Level 2	Level 3
A (degree)	45	22.5	0
B (m)	1.267	0.725	0.200
C (m)	1.220	1.020	0.820

TABLE 6: The proof of the orthogonal.

case	A	B	C	AB	BC	CA
1	+	+	+	+	+	+
2	+	-	-	-	+	-
3	+	0	0	0	0	0
4	-	+	-	-	-	+
5	-	-	0	+	0	0
6	-	0	+	0	0	-
7	0	+	0	0	0	0
8	0	-	+	0	-	0
9	0	0	-	0	0	0
Total	0	0	0	0	0	0

C, the extreme values and their medium value are taken into consideration, ranging from the highest and lowest position. Different values are noted as different levels in Taguchi method as shown in Table 5.

Table 6 is the orthogonal table for Taguchi analysis with factors A, B, and C. A correct orthogonal table needs to fulfill with following two conditions: (1) In a column, the numbers of different values should be the same. (2) The same levels have the same frequency in every two columns.

L_9 orthogonal array is used here; it contains nine tests, three levels, and three variables (L means Latin square and 9 means the number of cases). The orthogonal table is recorded in Table 7 and it can be used as experiment scheme.

3.3. *The Analysis of the SNR.* In Taguchi method, the ratio of signal to noise (SNR) is always used as the key value to evaluate the performance of each experiment in Taguchi analysis. In this study, the target is to find smaller mean square errors; thus SNR can be expressed as (16). A bigger value of SNR is needed since it is negatively correlated with Y [27].

$$\eta = -10 \lg \frac{1}{n} \left(\sum_{i=1}^n Y_i^2 \right) \quad (16)$$

η represents the SNR. n is the number of replications. Since it is expected to be smaller that both the mean square errors of velocity and pressure, a smaller value is what we needed. In Taguchi method, the ratio of signal to noise (SNR) is used instead of mean square errors as SNR can expand the range of smaller values. In (16), Y_i^2 is used to eliminate the negative values and an average is calculated. A logarithmic relation can amplify the average of Y_i^2 when it is under 1; this means the contrast ratio for smaller values is increased and it is benefit to our optimization based on mean square errors. Then the result is multiplied by 10 to observe easily. Finally, an opposite number is chosen and that means that a smaller mean square

TABLE 7: The orthogonal table of separator.

case	A	B	C
1	A1	B1	C1
2	A1	B2	C2
3	A1	B3	C3
4	A2	B1	C2
5	A2	B2	C3
6	A2	B3	C1
7	A3	B1	C3
8	A3	B2	C2
9	A3	B3	C1

For example, A1 stands for factor A with Level 1.

error has a bigger SNR as (16). We can find that SNR can expand the range of smaller values with logarithmic relation and describe the result more clearly. In another way, SNR is more sensitive to a small value and that is what we care; thus we take SNR instead of Y. From the explanation above, a better result has a bigger SNR as to (16).

The SNR, a function of noise, is a good performance measure for robustness, is a good performance measure for robustness. Thus, it is expected that the results of statistically significant should represent the optimal combination of kinematic parameters [28]. The η is used to evaluate the fluctuation of mean square error about combination parameters in the article.

Values of Y and η from 180 data points on three sections of each model are calculated. 9 cases in Table 7 are calculated and the results are recorded in Tables 8 and 9. Table 8 shows the result with velocity while Table 9 with pressure.

Then the contribution rate is expressed as (17). It reflects the importance of different factors to η . z is the z th control factors, namely, the factors in Table 4. $\eta_{\max z} - \eta_{\min z}$ is the range of different factors. m is the number of levels of a factor. Contribution rates are recorded in Tables 10 and 11.

$$CR_z = \frac{\eta_{\max z} - \eta_{\min z}}{\sum_{z=1}^m (\eta_{\max z} - \eta_{\min z})} \times 100\% \quad (17)$$

From Table 10, A and B play important roles in determine the uniform of velocity, because they both have a contribution over 39%. The influence of C is much smaller. From Table 11, it can be found that C, over 56%, is considered to be the most important factor to distribution of pressure and A is less important with 41%, while factor B has almost no impact on pressure with 2.184%. In the work, we must select the factors with contribution rate.

In order to obtain better parameters of the separator, both distributions are considered. The values of η according to factors are shown in Figures 3 and 4. Target values of η are bigger ones, with contribution rate; the best scheme is A2B2C2 according to Figure 3. As to the effective of pressure, A2B2C2 is still the best scheme. Although it comes from different physical quantities, the result is the same.

It can be seen that there is a positive correlation between the distribution of velocity and pressure. A better scheme

TABLE 8: The results about velocity.

case	A(degree)	B(m)	C(m)	Y	η
1	45	1.267	1.220	3.000	-9.542
2	45	0.725	1.020	1.052	-0.440
3	45	0.200	0.820	1.895	-5.552
4	22.5	1.267	1.020	1.338	-2.529
5	22.5	0.725	0.820	0.677	3.388
6	22.5	0.200	1.220	0.121	18.344
7	0	1.267	0.820	1.687	-4.542
8	0	0.725	1.020	0.181	14.846
9	0	0.200	1.220	0.790	2.047

TABLE 9: The results about pressure.

case	A(degree)	B(m)	C(m)	Y	η
1	45	1.267	1.220	38.132	-31.626
2	45	0.725	1.020	16.057	-24.113
3	45	0.200	0.820	43.186	-32.707
4	22.5	1.267	1.020	3.895	-11.810
5	22.5	0.725	0.820	40.566	-32.163
6	22.5	0.200	1.220	2.042	-6.201
7	0	1.267	0.820	55.801	-34.933
8	0	0.725	1.020	3.405	-10.642
9	0	0.200	1.220	31.813	-30.052

TABLE 10: The contribution of factors based on velocity.

		A	B	C
SNR	1	-5.178	-5.528	3.616
	2	6.401	5.931	3.959
	3	4.117	4.947	-2.235
Range		11.579	11.459	6.194
Contribution Rate		39.611%	39.200%	21.189%

TABLE 11: The contribution of factors based on pressure.

		A	B	C
SNR	1	-29.482	-26.123	-22.626
	2	-16.725	-22.306	-15.522
	3	-25.209	-22.987	-33.267
Range		-12.757	-0.681	-17.745
Contribution Rate		40.910%	2.184%	56.906%

can be obtained with Taguchi method to get a uniform distribution of fluid filed in inner part.

3.4. Result. From the result above, A2B2C2 is considered as the best scheme. The mean square errors of velocity and pressure are shown in Figures 5 and 6, respectively.

The mean square error of the 10th scheme is close to the optimal, as well as the case of 6th scheme and the case of 8th scheme. The most obvious characteristic of the three cases is the smaller angle between import and horizontal. Therefore, control factor A has great influence for the flow

field uniformity in the filter sections. We can draw the conclusion that the Taguchi method can also evaluate the importance of a single factor.

The Taguchi methods can not only evaluate the importance of elements and also evaluate the rate of contribution of the single factor. This method applied in structure design can be refined and extended in a follow-up study such as increasing the number of parameters and the degree of level factors. A better scheme can be got to reduce the cost of design and manufacture through the analysis and calculation.

4. Conclusion

In this paper, a separator is simulated with CFD, and key parameters of a separator are optimized with Taguchi method. The results in this paper are as follows:

(1) The process of movement and diffusion of particles is obtained. The accumulation areas of particle are found, and the causes of accumulation are analyzed through the distribution figures. An evaluation for the structure of the original separator is taken.

(2) Taguchi method is introduced to take orthogonal experiment. It can reduce 27 schemes to 9. Then the weights of key parameters are determined through the contribution rate and it can be known which parameter has a bigger influence on separator

(3) The optimal scheme, namely, A2B2C2, is determined according to the results of a bigger SNR value. It is verified by numerical simulation and found that mean square error of distributions from both velocity and pressure is close to the minimum. The optimization of the structure is realized.

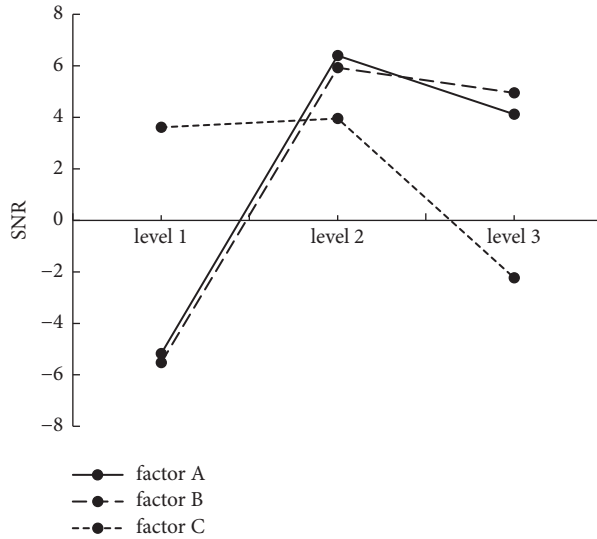


FIGURE 3: SNR according to velocity.

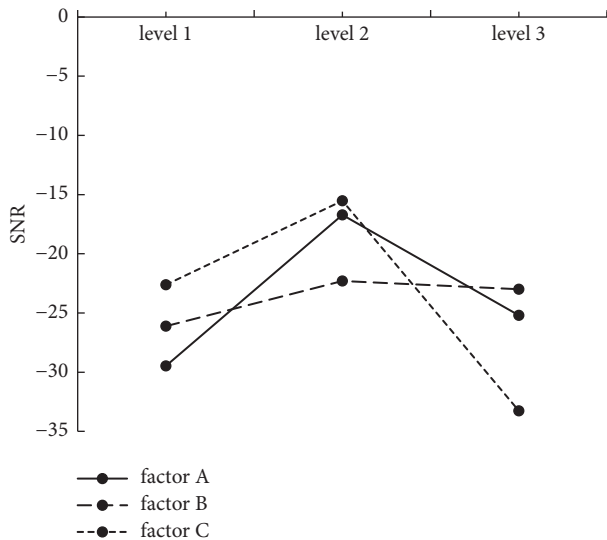


FIGURE 4: SNR according to pressure.

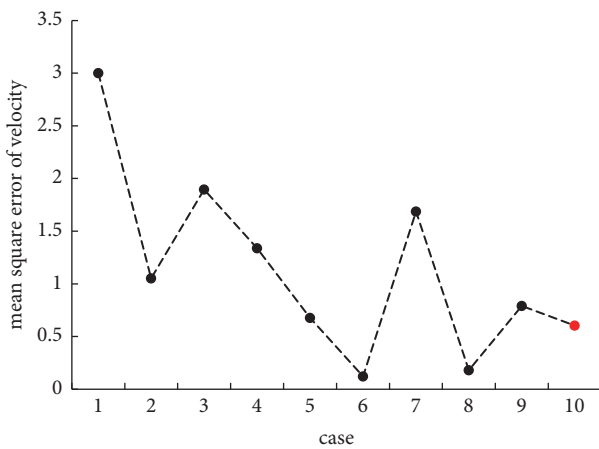


FIGURE 5: The mean square error of velocity in all cases.

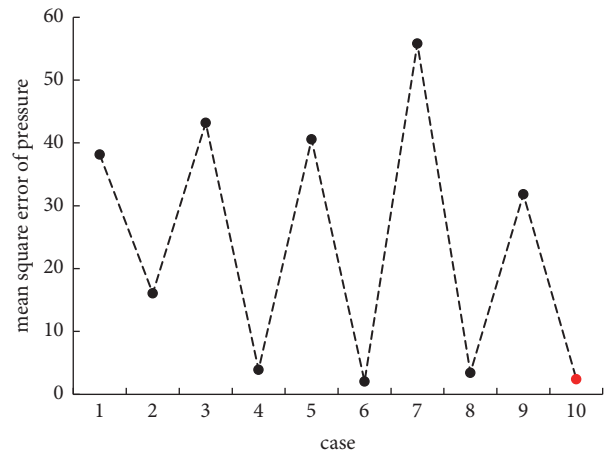


FIGURE 6: The mean square error of pressure in all cases.

In this paper a theoretical foundation and effective means has been provided and help in extending the knowledge on the research of optimization design in separator.

Data Availability

The data used to support the findings of this study are included in the supplementary material file.

Conflicts of Interest

The authors declare that they have no conflicts of interest.

Acknowledgments

This work was supported by the National Natural Science Foundation of China (Grant 51876175), the Innovative Talents

Promotion Project of Shaanxi, China (Grant 2018KJXX-067), and the Tianjin Municipal Science and Technology Foundation (no. 14JCYBJC43200).

Supplementary Materials

The data is extracted from the postprocessing software Tecplot. There are a total of 9 cases with 120 speed values for each case. The mean square error is obtained by the 120 data of each case. SNR is obtained from the formula in Table 5 of the article. The data processing in other forms have been clearly stated in paper. The file data are used to support the findings of this study. (*Supplementary Materials*)

References

- [1] Y. Xiong, "High moisture lignite coal burning power generation integrated drying technology," *Boiler Technology*, pp. 46–49, 2006.
- [2] J. A. M. Kuipers, K. J. Van Duin, F. P. H. Van Beckum, and W. P. M. Van Swaaij, "A numerical model of gas-fluidized beds," *Chemical Engineering Science*, vol. 47, no. 8, pp. 1913–1924, 1992.
- [3] H. T. Bi and J. Li, "Multiscale analysis and modeling of multiphase chemical reactors," *Advanced Powder Technology*, vol. 15, no. 6, pp. 607–627, 2004.
- [4] Y. Tsuji, T. Tanaka, and T. Ishida, "Lagrangian numerical simulation of plug flow of cohesionless particles in a horizontal pipe," *Powder Technology*, vol. 71, no. 3, pp. 239–250, 1992.
- [5] Y. X. Wu, X. Wang, and C. B. Ching, "Computational fluid dynamics simulation of the adsorption separation of three components in high performance liquid chromatography," *Chromatographia*, vol. 55, no. 7-8, pp. 439–445, 2002.
- [6] H. Boysen, G. Wozny, and T. Laiblin, "CFD simulation of preparative HPLC columns with consideration of nonlinear isotherms," *Chemical Engineering & Technology*, vol. 26, no. 6, pp. 651–655, 2003.
- [7] Y. Liming, X. Zhou, J. Yang et al., "Numerical Simulation of Water and Sediment Movement in Screen Filter Based on Coupled CFD-DEM," *Transactions of the Chinese Society for Agricultural Machinery*, vol. 3, pp. 303–308, 2018.
- [8] B. Wang, D. L. Xu, K. W. Chu, and A. B. Yu, "Numerical study of gas-solid flow in a cyclone separator," *Applied Mathematical Modelling*, vol. 30, no. 11, pp. 1326–1342, 2006.
- [9] T. Zhao, K. Liu, Y. Cui, and M. Takei, "Three-dimensional simulation of the particle distribution in a downer using CFD-DEM and comparison with the results of ECT experiments," *Advanced Powder Technology*, vol. 21, no. 6, pp. 630–640, 2010.
- [10] M. Haim, Y. Weiss, H. Kalman, and A. Ullmann, "The effect of the inlet conditions on the numerical solutions of particle-gas flows," *Advanced Powder Technology*, vol. 14, no. 1, pp. 87–110, 2003.
- [11] X. Gao, T. Li, A. Sarkar, L. Lu, and W. A. Rogers, "Development and validation of an enhanced filtered drag model for simulating gas-solid fluidization of Geldart A particles in all flow regimes," *Chemical Engineering Science*, vol. 184, pp. 33–51, 2018.
- [12] J. A. Pamanes, J. P. Montes, E. Cuan, and G. F. Rodriguez, "Optimal placement and synthesis of a 3R manipulator," in *Proceedings of the International Symposium on Robotics and Automation*, Monterrey, Mexico, 2000.
- [13] G. Taguchi, *Introduction to Quality Engineering Designing: Quality into Products and Processes*, Asian Productivity Organization, Tokyo, Japan, 1986.
- [14] G. Taguchi, *Studies on Mathematical Statistics for Quality Control [Doctoral thesis]*, Kushu University, Japan, 1962.
- [15] B. K. Rout and R. K. Mittal, "Tolerance design of robot parameters using Taguchi method," *Mechanical Systems and Signal Processing*, vol. 20, no. 8, pp. 1832–1852, 2006.
- [16] T. Mothilal, K. Pitchandi, V. Velukumar, and K. Parthiban, "CFD and statistical approach for optimization of operating parameters in a tangential cyclone heat exchanger," *Journal of Applied Fluid Mechanics*, vol. 11, no. 2, pp. 459–466, 2018.
- [17] A. Bejan and D. A. Nield, *Convection in Porous Media*, Springer, New York, NY, USA, 3rd edition, 2006.
- [18] T. L. Dantas, F. M. Luna, I. J. Silva et al., "Carbon dioxide-nitrogen separation through pressure swing adsorption," *Chemical Engineering Journal*, vol. 172, no. 2-3, pp. 698–704, 2011.
- [19] E. Glueckauf, "Theory of chromatography. Part 10. Formula for diffusion into spheres and their application to chromatography," *Transactions of the Faraday Society*, vol. 51, pp. 1540–1551, 1955.
- [20] S. U. Rege and R. T. Yang, "Limits for Air Separation by Adsorption with LiX Zeolite," *Industrial & Engineering Chemistry Research*, vol. 36, no. 12, pp. 5358–5365, 1997.
- [21] J. C. Tannehill, R. H. Pletcher, and D. A. Anderson, *Computational Fluid Mechanics Foundation and Its Applications*, Taylor & Francis Inc, UK, 2nd edition, 1997.
- [22] L. Mangani and C. Bianchini, "Heat transfer applications in turbomachinery," in *Proceedings of the Open FOAM International Conference*, Florence, Italy, 2007.
- [23] T. Wigmans, H. Haringa, and J. A. Moulijn, "Role of the influence of potassium during pyrolysis of medium volatile coal," *Fuel*, vol. 63, no. 6, pp. 870–872, 1984.
- [24] P. Rosin and E. Rammler, "The Laws Governing the Fineness of Powdered Coal," *Journal of the Institute of Fuel*, vol. 7, pp. 29–36, 1933.
- [25] N. C. Sagias and G. K. Karagiannidis, "Gaussian class multivariate Weibull distributions: theory and applications in fading channels," *Institute of Electrical and Electronics Engineers Transactions on Information Theory*, vol. 51, no. 10, pp. 3608–3619, 2005.
- [26] Q. Zou, Y. Xu, and C. Zheng, "Optimization of Structural Parameters of Drilling slotting Integration Nozzle Based on Taguchi Method," *Coal Mine Machinery*, vol. 33, no. 10, pp. 17–19, 2012.
- [27] Z.-B. Yang, M. Radzienski, P. Kudela, and W. Ostachowicz, "Two-dimensional Chebyshev pseudo spectral modal curvature and its application in damage detection for composite plates," *Composite Structures*, vol. 168, pp. 372–383, 2017.
- [28] L. Wang, C. Wang, W. Du et al., "Parameter optimization of a four-legged robot to improve motion trajectory accuracy using signal-to-noise ratio theory," *Robotics and Computer-Integrated Manufacturing*, vol. 51, pp. 85–96, 2018.

Research Article

Parameter Optimization and Prediction Model of Induction Heating for Large-Diameter Pipe

Xiurong Fang , Jia Lu, Junfeng Wang, and Jinhui Yang

School of Mechanical Engineering, Xi'an University of Science and Technology, Xi'an 710054, China

Correspondence should be addressed to Xiurong Fang; fangxr098@163.com

Received 26 July 2018; Revised 6 October 2018; Accepted 1 November 2018; Published 26 November 2018

Guest Editor: Arshad Afzal

Copyright © 2018 Xiurong Fang et al. This is an open access article distributed under the Creative Commons Attribution License, which permits unrestricted use, distribution, and reproduction in any medium, provided the original work is properly cited.

The parameters of induction heating of large-diameter pipes have a direct effect on the final processing quality of the elbow, and the complexity of multifield coupling of magnetothermal force in induction heating can make it impossible to quantitatively optimize the design parameters of the induction heating device. In this paper, X80 pipeline steel induction heating is taken as the research object, and a corresponding numerical model is established. The influence of induction heating process parameters on the heating temperature of pipeline steel under the skin effect is determined. First, the influence of process parameters on the heating effect of pipeline steel is quantified by orthogonal test. Then, taking the optimum temperature difference between the inner and outer wall of X80 pipeline steel during the induction heating process as a target, the optimal process parameter set of the pipe induction heating is determined by using neural network genetic algorithm. Finally, comparing the relevant test criteria of the regression equation, the optimum mathematical prediction model of the outer wall temperature of the pipe induction heating process is obtained, which provides a theoretical basis for optimization of the process parameters of the pipe-based induction heating device.

1. Introduction

The induction heating of pipe is one of the common techniques for production of elbows thanks to its rapid heating, easy cooling, small thinning rate of wall thickness, and easy adjustment of the bending radius of elbow. In the actual project of oil and gas transmission engineering, the bending of large-diameter pipes in oil and gas transportation pipe network is mostly processed by hydraulic push-type induction heating pipe bending machine. The system diagram is shown in Figure 1 [1], and the specific induction heating diagram is shown in Figure 2 [2]. It is required to realize continuous operation of propulsion→heating→bending→cooling→forming while the induction heating device fulfills the local heating of the pipe when the pipe bending machine is working [3]. At present, many researchers have conducted a lot of studies on the bending process of different materials, the mechanical properties, and the microstructure of the bent pipe [4–7]. However, the influence of various parameters on the heating effect of the induction heating

forming process for large-diameter pipe is not yet clear. The detailed theoretical guidance and basis for the selection and optimization of design parameters on the induction heating device are not yet available. Thus, it is impossible to ensure a reasonable matching between the heating time of the pipe and the pushing speed of the hydraulic cylinder, resulting in the fact that the reliability of the pipe quality cannot be guaranteed [8]. Therefore, the induction heating device of the pipe has become one of the important factors affecting the final processing quality of the elbow. In this paper, the optimization of the process parameters of pipe induction heating is investigated by means of numerical simulation and mathematical methods.

2. Analysis on Induction Heating Parameters of Pipes

The basic principle of induction heating is shown in Figure 3: the coil is connected to the heating power source, and an alternating magnetic field is generated in the pipe when the alternating current in the heating power source flows

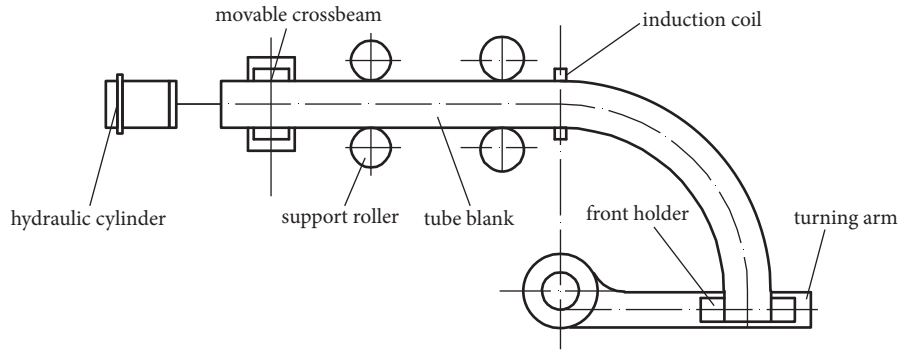


FIGURE 1: Structure of the bend of induction heating pipe bending machine.

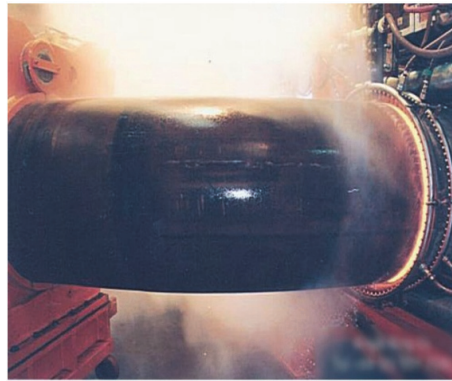


FIGURE 2: Specific induction heating.

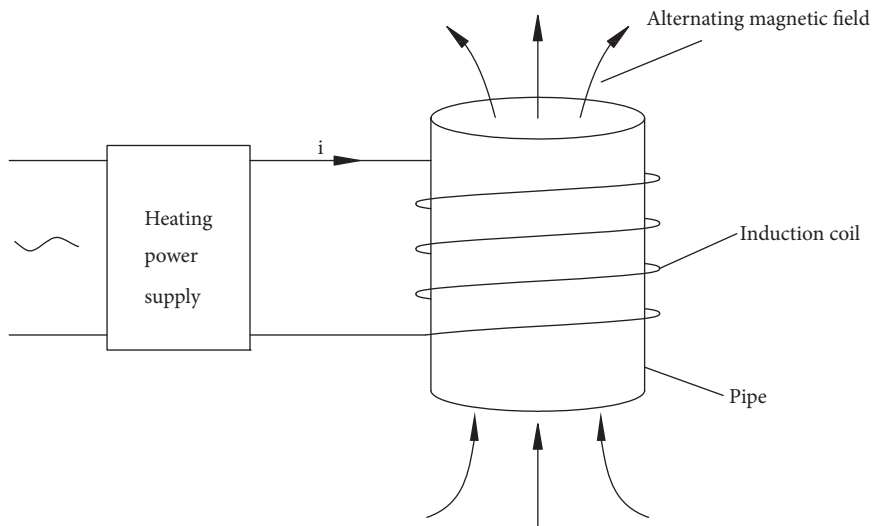


FIGURE 3: Schematic diagram of pipe induction heating.

through the coil. Under the action of the alternating magnetic field, vortex current is generated inside the pipe, and the vortex current and alternating current in the induction coil have opposite directions with the same frequency. When the vortex current passes through the pipe, the pipe generates a large amount of Joule heat under the action of the material

resistance, so that the pipe temperature rises rapidly to achieve the purpose of heating [9].

It can be seen that electromagnetic induction is used to generate vortex current heating in the conductor to realize the heating of the work piece. Therefore, by the electromagnetic induction law (1), the Joule-Electric law (2), and technical

requirements of the large-diameter pipe induction heating forming device, we can obtain the main influential factors on the heating effect of the pipe, such as the induction frequency, current density, and air gap [10].

$$e = -N \frac{d\Phi}{dt} \quad (1)$$

$$Q = 0.24i^2Rt \quad (2)$$

where N is the number of turns of the induction coil; Q is Joule heat (unit is J); i is the effective value of induction current (unit is A); R is conductor resistance (unit is Ω); and t is the time of the current flowing through the conductor (unit is s).

Taking the elbow forming of X80 pipeline steel [11] with diameter $\Phi 1219$ mm and wall thickness $\delta 27$ mm as an example, the numerical modeling of induction heating is carried out.

2.1. Mathematical Model of Induction Heating Electromagnetic Field. In the numerical calculation of finite element, the mathematical model of the induction heating vortex current field for the heated workpiece area can be obtained by the control equation (Maxwell equations) and the magnetic vector-scalar potential (\vec{A} - Φ) theory of the induction heating electromagnetic field [12–14]:

$$\nabla \times \frac{1}{\mu} \nabla \times \vec{A} - \nabla \frac{1}{\mu} (\nabla \cdot \vec{A}) + \sigma \frac{\partial \vec{A}}{\partial t} + \sigma \nabla \Phi = 0 \quad (3)$$

$$\nabla^2 \Phi + \frac{\partial}{\partial t} (\nabla \cdot \vec{A}) = 0 \quad (4)$$

$$\vec{J}_e = -\sigma \frac{\partial \vec{A}}{\partial t} - \sigma \nabla \Phi \quad (5)$$

where ∇ is Hamilton operator; μ is magnetic conductivity (H/m); σ is material conductivity (S/m); ϵ is capacitivity (F/m); \vec{A} is magnetic vector potential; Φ is scalar potential; and \vec{J}_e is induction vortex current density vector (A/m^2).

In order to ensure the continuity condition of the field quantity at the interface of different media, consider the boundary condition as a ferromagnetic boundary with surface current density \vec{J} . The expression is shown as

$$\vec{n} \times \left(\frac{1}{\mu} \nabla \times \vec{A} \right) = -\vec{J} \quad (6)$$

2.2. Mathematical Model of Induction Heating Temperature Field. It is assumed that the Joule heat generated by the vortex current in the alternating magnetic field is completely converted into its own heat; that is, the induced current Joule heat obtained by the electromagnetic field is used as an internal heat source to heat the workpiece, and the heating process is an unsteady heat conduction process [15, 16]. Based on Fourier's law and the first law of thermodynamics [17], the

differential form of the transient temperature field governing equation in induction heating can be derived:

$$\rho c \frac{\partial T}{\partial t} - \frac{\partial}{\partial x} \left(\lambda_x \frac{\partial T}{\partial x} \right) - \frac{\partial}{\partial y} \left(\lambda_y \frac{\partial T}{\partial y} \right) - \frac{\partial}{\partial z} \left(\lambda_z \frac{\partial T}{\partial z} \right) - q_v = 0 \quad (7)$$

where λ is thermal conductivity ($W/(m \cdot ^\circ C)$); T is temperature field distribution function; q_v is intensity of the heat source of induction vortex current in the pipeline (W/m^3); ρ is material density (Kg/m^3); c is the specific heat capacity of material ($J/(Kg \cdot K)$).

Use the Newton convection boundary as a temperature boundary condition:

$$-\lambda \frac{\partial T}{\partial n} = h(T - T_0) \quad (8)$$

where n refers to the normal direction on the boundary; λ is thermal conductivity ($W/m \cdot ^\circ C$); h is convective heat transfer coefficient ($W/m^2 \cdot K$); T is work surface temperature (K); and T_0 indicates ambient temperature (K).

2.3. Coupling of Induction Heating Electromagnetic Field-Temperature Field. The induction heating is involved in the interaction of two physical fields of electromagnetic field and temperature field. The complexity of solving the magneto-thermal coupling problem makes it difficult to obtain accurate solutions for many engineering issues [18]. Hopefully, the large-scale finite element numerical simulation software can be used for engineers to solve complex problems on the basis of theoretical analysis. This paper is aimed at the characteristics of induction heating magneto-thermal coupling of large-diameter pipes. We adopt ABAQUS software to solve the magneto-thermal coupling issue by sequential coupling [19]. First, the vortex current is obtained in the electromagnetic field; then the Joule heat of the workpiece under the action of vortex current field is got. Eventually, the Joule heat is used as the temperature field input condition to obtain the temperature distribution on the workpiece. The analysis process of magneto-thermal coupling during the induction heating is shown in Figure 4.

2.4. Building of Numerical Model. The geometric model of pipe induction heating consists of three parts: X80 pipe, induction coil, and air. Since the pipe is only involved in the solution of temperature field, it is assumed that, in the solution of the electromagnetic field, the physical properties of the material corresponding to the induction coil and air are not affected by the temperature change. Since the X80 pipe, induction coil and air together constitute the electromagnetic path in the induction heating process, the thermal property parameters of the relative magnetoconductivity, resistivity, specific heat capacity, thermal conductivity, density, etc. corresponding to the three parts should be considered in solving the electromagnetic field (as shown in Table 1). The material of induction coil is T3 copper, its resistivity is $1.75 \times 10^{-8} \Omega \cdot m$, and the relative magneto-conductivity is 1. As air is

TABLE I: The thermal properties of X80.

Temperature (°C)	Relative Permeability μ	Resistivity ρ ($10^{-6}\Omega\cdot\text{m}$)	Specific Heat C_p (J/Kg $\cdot^\circ\text{C}$)	Thermal Conductivity K (W/m $\cdot^\circ\text{C}$)	Density ρ (Kg/m 3)	Emissivity C_s (J/m $^2\text{sK}^4$)
0	200	0.195	450	47.4	7896	1
25	198	0.202	450	46.2	7896	0.998
100	194	0.251	479	43.7	7870	0.996
200	186	0.336	520	40.3	7849	0.992
300	179	0.434	564	38	7824	0.987
400	167	0.539	612	35.9	7796	0.983
500	156	0.659	668	33.8	7769	0.978
600	139	0.792	785	31.7	7744	0.978
700	93	0.947	936	28.4	7716	0.879
800	1	1.073	848	25.9	7691	0/648
900	1	1.164	655	23.5	7665	0.594
1000	1	1.199	620	23.9	7639	0.535

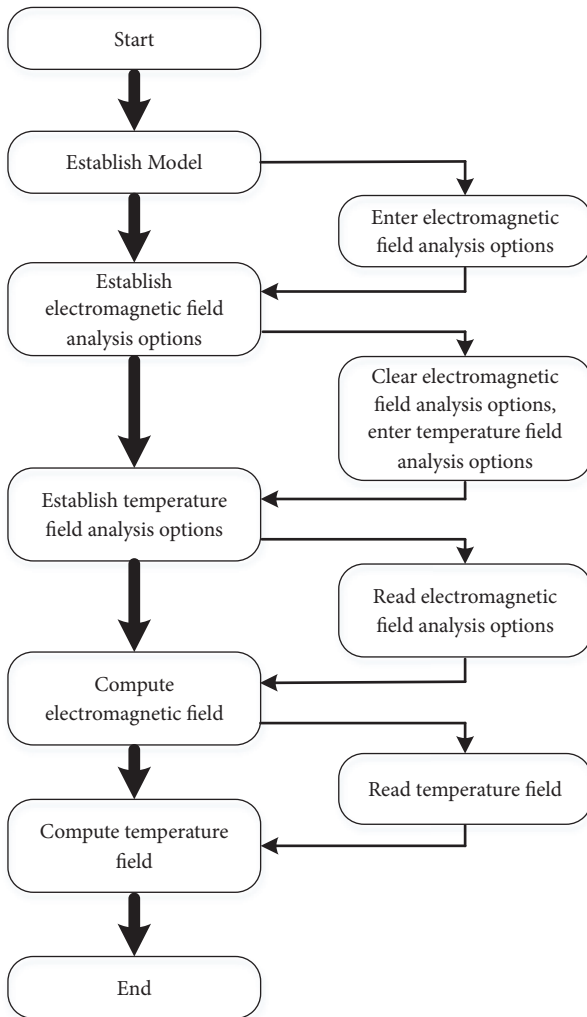


FIGURE 4: Analysis process of magnetothermal coupling during the induction heating.

not affected by the current, the relative magnetoconductivity should be set as 1 when performing numerical simulation.

It is one of the important influential factors on the quality of the pipe to reasonably match the heating time of the pipe and the pushing speed of the hydraulic cylinder during the bending process of the large-diameter pipe (see Figure 1). Thus, in order to further study the problem of matching the induction heating time with the pushing speed, the finite element model is built in Cartesian coordinate system. At the same time, considering that the large-diameter pipe and its applied load are axisymmetric, 1/4 of the pipe is used to build a finite element model. The working loads are applied to the model according to the characteristics of each physical field; the corresponding analysis steps, solution variables, and boundary conditions are setup; different grid types are selected to mesh the model (the unit type of EMC3D8 is selected in the electromagnetic field and the unit type of DC3D8 is selected in the temperature field). In order to ensure the accuracy and convergence of the calculation, the pipe mesh is refined, as shown in Figure 5.

3. Results Analysis

3.1. Analysis of Numerical Simulation Results. In order to visually display the dynamic changes of the electromagnetic field and temperature field inside the pipe during the heating process, the main parameters such as current frequency ($f=1000\text{Hz}$), current density ($J=6 \times 10^7 \text{A/m}^2$), and air gap ($d=30\text{mm}$) are determined according to the engineering practice, and the distribution clouds of the Joule heat and temperature of the pipe under induction heating are obtained through simulation (see Figures 6 and 7), and the curves of temperature for the inner and outer wall of the pipe with the times are shown in Figure 8. It can be seen that the distribution of Joule heat and temperature on the pipe is that the outer wall's is much greater than that of the inner wall due

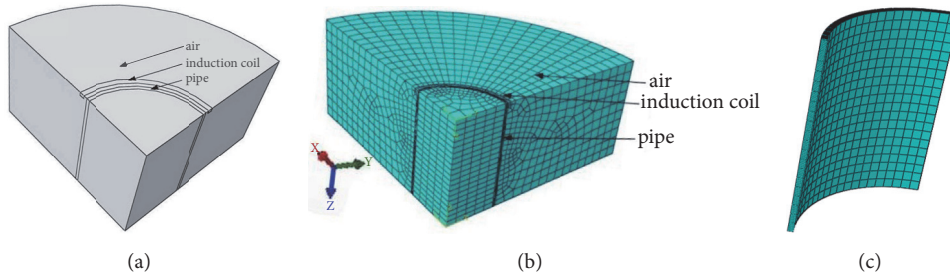


FIGURE 5: Numerical model of induction heating for thin-walled pipe. (a) Geometric model. (b) Finite element model. (c) Finite element model of the pipe.

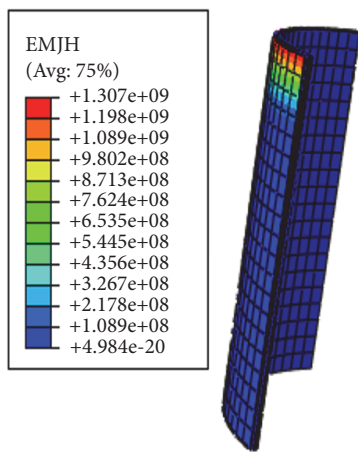


FIGURE 6: Distribution cloud of Joule heat in pipe (Unit: J).

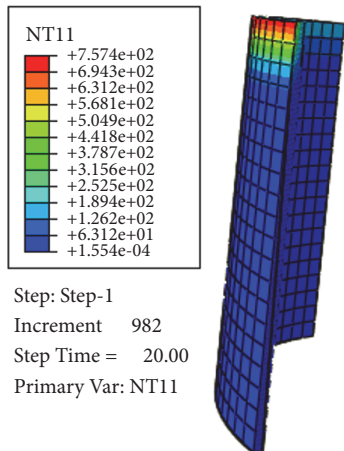


FIGURE 7: Distribution cloud of temperature in pipe (Unit: °C).

to the effects of skin effect, proximity effect, and ring effect in the induction heating process [20], which ultimately leads to the greater temperatures difference of the inner and outer walls of the pipe, causing a great inconvenience to the pushing speed of the elbow, which in turn affects the quality of the pipe bending.

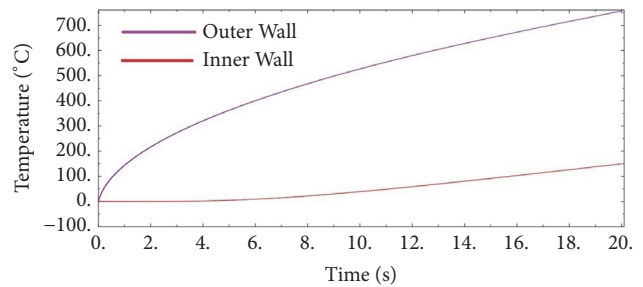


FIGURE 8: Temperature curves of the inner and outer wall of pipe with the times.

It can be seen from Figure 8 that although there is unevenness in the temperature rise of the inner and outer walls in the pipe, the difference in temperatures between the inner and outer walls tends to be stable as the increase of heating time. Therefore, by parameter optimization, the difference in temperature gradient between the inner and outer walls of the pipe is reduced as much as possible.

In order to further explore the relationship between the current frequency, current density, air gap, and pipe heating effect, the control variable method is used to change the three process parameters for simulation calculation. The results are shown in Figure 9.

Figure 9 shows the effect of the current frequency, current density, and the air gap between coil and pipe on the temperature rise of the inner and outer wall of the pipe, respectively. It can be seen from the figure although that relationship between the variation of parameters and the temperature of the inner and outer wall of the pipe is basically linear; the influence of three parameters on the heating effect of pipe cannot be quantified. Moreover, the temperature difference between the inner and outer wall of the pipe is the key quantity; thus it is necessary to analyze the variation rule of the temperature difference between the inner and outer wall of the pipe to find the optimal parameter group.

3.2. Parameter Optimization Based on Orthogonal Test Design

3.2.1. Orthogonal Test Design for Induction Heating of Pipe.

The three process parameters of the current frequency,

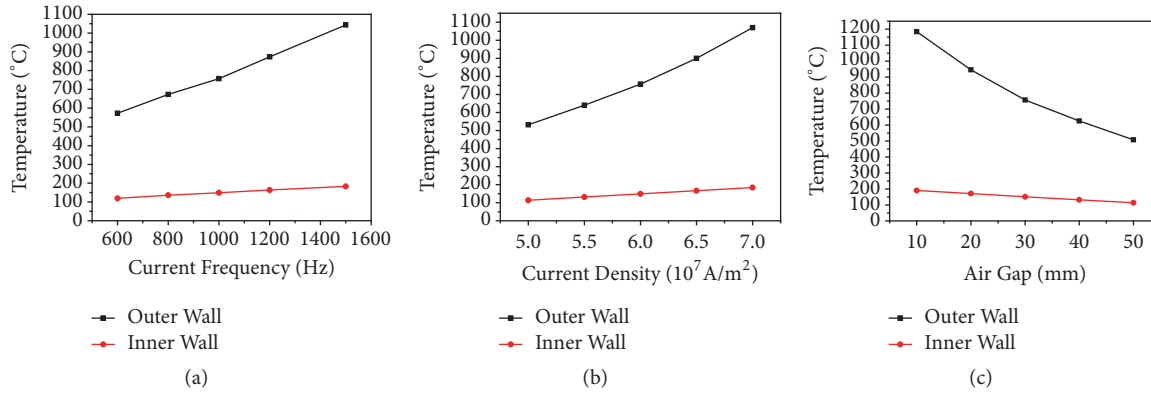


FIGURE 9: Relationship between three parameters and the inner and outer wall temperature of pipe. (a) Current frequency. (b) Current density. (c) Air gap between pipe and induction coil.

TABLE 2: Test parameters and levels.

Level	Factor		
	Current Frequency f (Hz)	Current Density J (A/m ²)	Air Gap d (mm)
1	600	5×10^7	10
2	800	5.5×10^7	20
3	1000	6×10^7	30
4	1200	6.5×10^7	40
5	1500	7×10^7	50

current density, and air gap are the factors of the orthogonal test [21], and each factor is set at 5 levels, as shown in Table 2.

It can be seen from Table 2 that there is a total of 125 experimental parameter combinations, and the orthogonal test is mainly used to analyze the primary and secondary relationship of the influence of various process parameters on the heating effect. Therefore, according to the orthogonality and the engineering practice, some parameter groups with the characteristics of “uniform dispersion, neatness, and comparability” are selected as the representative ones for the experiment.

In the orthogonal experimental analysis, the Taguchi design method is used to neglect the interaction between different process parameters, the L25 (5^6) orthogonal table is selected, and the empty column is adopted as the error column. According to the 25 sets of parameters selected in Table 3, the numerical simulation analysis of the induction heating of X80 pipe ($\Phi 1219$ mm, wall thickness 27 mm) is carried out to obtain the temperatures of the inner and outer walls of the pipe. The orthogonal experimental scheme is designed with the temperatures of the inner and outer walls of the pipe as the test indexes (see Table 3).

3.2.2. Analysis of the Orthogonal Test Results of Induction Heating of Pipe. The variance method is used to determine the significant degree and contribution rate of the influence of various process parameters on the heating effect of medium-frequency induction heating of large-diameter pipes, and

the primary and secondary relationship of the influence of various process parameters on the heating effect is obtained. Then we use the range analysis to verify the primary and secondary relationships again to provide a guidance for engineering process design.

(1) *Variance Analysis.* The analysis results of the influence of each parameter on temperatures of the inner and outer walls of the pipe are shown in Tables 4 and 5.

(2) *Range Analysis.* First, the comprehensive mean and range of each factor are obtained, and then the primary and secondary relationships of the influence of the process parameters on the heating effect are got by comparing the extremes [22]. The range analysis of the inner and outer wall temperatures of the pipe under different levels in the orthogonal test is shown in Table 6:

According to the analysis results of Tables 4 and 5, when the temperature of the inner and outer walls of the pipe is taken as an index, the influence of the current frequency and current density on the index is significant, and the influence of the air gap on the index is extremely significant. And in the medium-frequency induction heating of the pipe, the influential degree of each process parameter on the heating effect of the pipe is air gap > current density > current frequency. From the range R corresponding to each process parameter in Table 6, it can be concluded that the influential degree of the process parameters on the heating effect of the pipe is consistent with the variance analysis result, which further verifies the accuracy of the obtained results. Compared with the range analysis, the contribution rate of each process parameter to the survey indicators is defined more clearly by the variance analysis.

It can be known from the engineering that when the induction heating temperatures of the outer wall of the pipe are 900~1000°C [23] and the difference between the inner and outer wall temperature is small, the final processing quality of the elbow is better. Combined with the above analysis, a better process parameter group can be initially determined as current frequency 1500 Hz, current density 5.5×10^7 A/m², and air gap 10 mm.

TABLE 3: Orthogonal test design scheme and numerical calculation results.

Test No.	Factor			Test Index	
	Current Frequency (Hz)	Current Density (A/m ²)	Interval (mm)	Outer Wall Temperature (°C)	Inner Wall Temperature (°C)
1	1(600)	1(5×10 ⁷)	1(10)	649	127
2	1(600)	2(5.5×10 ⁷)	2(20)	618	125
3	1(600)	3(6×10 ⁷)	3(30)	574	119
4	1(600)	4(6.5×10 ⁷)	4(40)	528	114
5	1(600)	5(7×10 ⁷)	5(50)	474	105
6	2(800)	1(5×10 ⁷)	2(20)	587	121
7	2(800)	2(5.5×10 ⁷)	3(30)	569	120
8	2(800)	3(6×10 ⁷)	4(40)	546	117
9	2(800)	4(6.5×10 ⁷)	5(50)	508	113
10	2(800)	5(7×10 ⁷)	1(10)	1526	215
11	3(1000)	1(5×10 ⁷)	3(30)	532	114
12	3(1000)	2(5.5×10 ⁷)	4(40)	528	115
13	3(1000)	3(6×10 ⁷)	5(50)	508	113
14	3(1000)	4(6.5×10 ⁷)	1(10)	1420	208
15	3(1000)	5(7×10 ⁷)	2(20)	1349	205
16	4(1200)	1(5×10 ⁷)	4(40)	509	112
17	4(1200)	2(5.5×10 ⁷)	5(50)	508	114
18	4(1200)	3(6×10 ⁷)	1(10)	1319	201
19	4(1200)	4(6.5×10 ⁷)	2(20)	1297	202
20	4(1200)	5(7×10 ⁷)	3(30)	1248	200
21	5(1500)	1(5×10 ⁷)	5(50)	510	115
22	5(1500)	2(5.5×10 ⁷)	1(10)	989	173
23	5(1500)	3(6×10 ⁷)	2(20)	1255	200
24	5(1500)	4(6.5×10 ⁷)	3(30)	1253	202
25	5(1500)	5(7×10 ⁷)	4(40)	1239	204

TABLE 4: Variance analysis results of the orthogonal test of temperatures for pipe's outer wall.

Sources of Variance	Degree of Freedom	Sum of Squares	Mean Square	F	Contribution Rate (%)	Significance
Current Frequency	4	0.996	0.25	31.63	21.28	*
Current Density	4	1.49	0.372	47.32	31.84	*
Air Gap	4	2.1	0.525	66.68	44.86	**
Error	12	0.095	0.008	–	2.02	
Total	24	4.671	1.155	–	100	

Note: * indicates that the difference is significant; ** indicates that the difference is extremely significant.

3.3. Process Parameter Optimization Based on Neural Network and Genetic Algorithm. The orthogonal experiment can determine the influence degree of the process parameters on the temperature of the inner and outer walls of the pipe and judge the better parameter group from the existing process parameter group. However, it is difficult to obtain the global optimal process parameters for the multiparameter group problems which affect the actual engineering. We use BP

neural network method to establish the mapping relationship between the induction heating process parameters and the temperatures of the inner and outer walls of the pipe [24, 25]. The data is trained to predict the heating effect of all combinations of process parameters within the variation range, and the process parameters are optimized by genetic algorithm [26, 27]. Thus, the global optimal process parameter group is obtained.

TABLE 5: Variance analysis results of orthogonal test of temperatures for pipe's inner wall.

Sources of Variance	Degree of Freedom	Sum of Squares	Mean Square	F	Contribution Rate (%)	Significance
Current Frequency	4	0.478	0.12	37.77	25.78	*
Current Density	4	0.589	0.147	46.47	31.72	*
Air Gap	4	0.751	0.188	59.26	40.45	**
Error	12	0.038	0.003	-	2.05	
Total	24	1.856	0.458	-	100	

Note: * indicates that the difference is significant; ** indicates that the difference is extremely significant.

TABLE 6: Range analysis results of orthogonal test for pipe's outer wall temperature.

	Outer Wall Temperature (°C)			Inner Wall Temperature (°C)		
	Current Frequency	Current Density	Air Gap	Current Frequency	Current Density	Air Gap
K_1	568.6	557.4	1180.6	118	117.6	184.8
K_2	747.2	642.4	1021.2	137.2	129.4	170.6
K_3	867.4	840.4	835.2	151	150	151
K_4	976.2	1001.2	670	165.8	167.8	132.4
K_5	1049.2	1167.2	501.6	178.8	185.8	112
R	480.6	609.8	679	60.8	68	72.8

Note: $K_1 \sim K_5$ represent the average temperature of each factor at each level, and R is range.

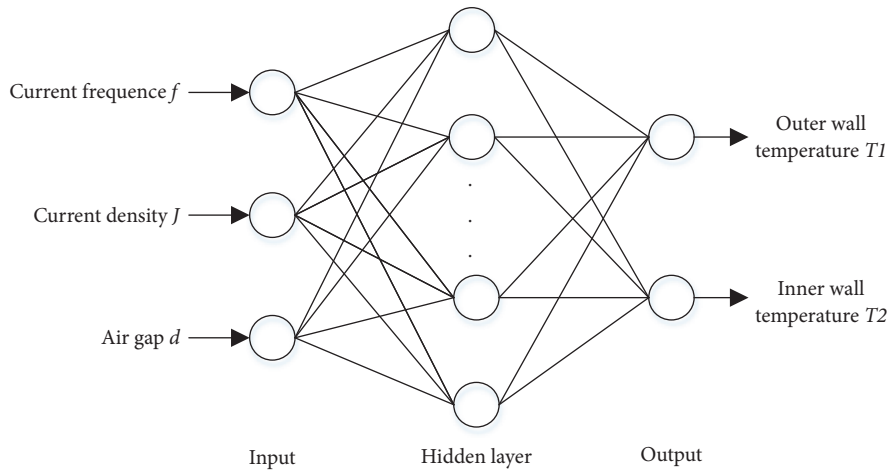


FIGURE 10: Structure of pipe induction heating BP neural network.

3.3.1. Prediction Model Based on BP Neural Network. The current frequency, current density, and air gap are selected as the network model input, and the outer and inner wall temperatures T_1 and T_2 of the pipe are taken as output to build a three-layer BP neural network model. The network structure is shown in Figure 10.

The data (see Table 3) obtained by numerical simulation is used as a training sample, and the sample is trained by running a BP neural network program. The training target is selected as 0.000001 and the learning rate is 0.1. The training of the network model is shown in Figure 11. When the

iteration is 274 times, the training is finished with the system error of 9.75×10^{-7} ; thus its error is within the expected range, and the network output is more accurate.

In order to verify the accuracy of the training prediction results, the five new sets of process parameters are reselected as test samples for training prediction and numerical simulation. The training prediction results and numerical simulation results are shown in Table 7.

According to the above results in Table 7, the error between the prediction data and the simulation data is within 3%, which indicates that the prediction accuracy of the BP

TABLE 7: Error between numerical simulation and BP neural network training.

Current Frequency f (Hz)	Current Density J (A/m ²)	Air Gap d (mm)	Outer Wall Temperature T_1 (°C)			Inner Wall Temperature T_2 (°C)		
			Simulation	Prediction	Error	Simulation	Prediction	Error
1200	6×10^7	30	883	862.5	2.3%	164	163.29	0.43%
1500	6×10^7	30	1043	1036.5	0.62%	183	185.35	1.3%
1000	5.5×10^7	30	640	638.2	0.28%	132	130.67	1%
1000	6.5×10^7	30	900	894.5	0.61%	167	163.40	2.1%
1000	7×10^7	30	1070	1079.3	0.87%	184	180.71	1.8%

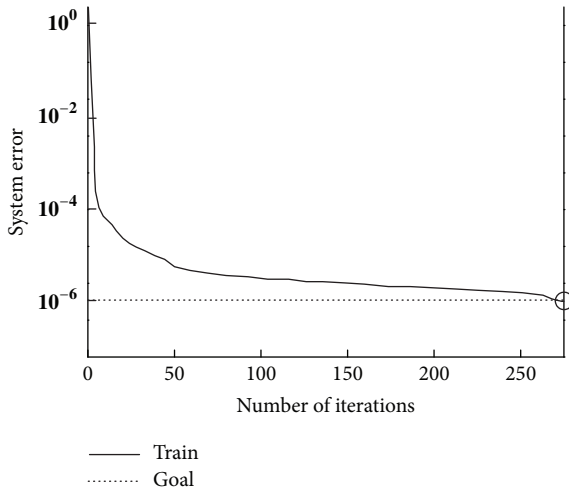


FIGURE 11: BP neural network training error curve.

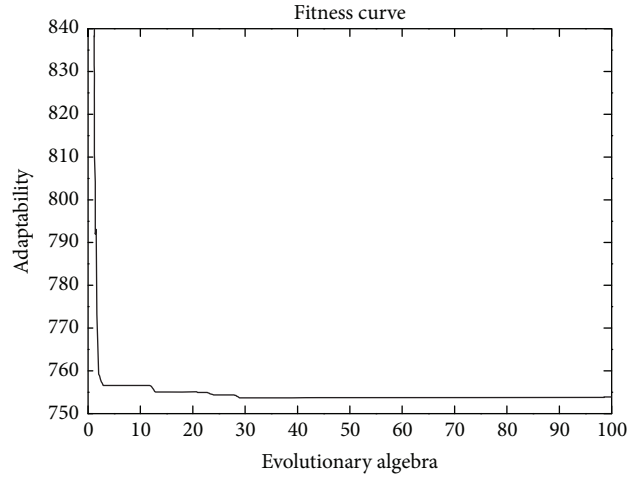


FIGURE 12: Genetic algorithm optimization process.

neural network for the heating effect is higher, and the prediction result is close to the actual situation.

3.3.2. *Optimization of Induction Heating Parameters Based on Genetic Algorithm.* The population with a size of 50 is selected and the binary code is adopted. The crossover probability and mutation probability are 0.75 and 0.01, respectively. The BP neural network prediction result is used as the fitness function to control the temperature of the inner and outer walls of the pipe [28, 29]. The genetic algorithm with 100 times of iteration is designed to optimize the process parameters of pipe induction heating. The software is used to iteratively calculate the BP neural network and genetic algorithm joint optimization program. After 100 iterations, the target fitness is shown in Figure 12.

It can be seen from the Figure 12 that, after 30 iterations, the fitness value of the temperature difference between the inner and outer wall under the processable condition is maintained at 751; meanwhile the temperature T_1 of the outer wall and the temperature T_2 of the inner wall is 923°C and 172°C, respectively. The process parameter group that is superior to the orthogonal test in the induction heating process of the pipe is obtained with the current frequency, current density, and air gap which are 1460 Hz, 5.65×10^7 A/m², and 15 mm, respectively.

3.4. *Pipeline Induction Heating Prediction Model Based on Regression Analysis.* Through the aforementioned analysis and calculation, the selection of optimal parameter group for the induction heating parameter design can be realized, but In order to further guide the engineering practice, a prediction model of pipe induction heating is necessary. In this paper, the regression analysis of the data obtained from numerical simulation is carried out to determine a reasonable mathematical model for the prediction of the outer wall temperature, which provides a certain theoretical guidance for the actual processing. The data obtained from the numerical simulation of medium-frequency induction heating of large-diameter pipe are taken as samples, and the process parameters that influence the induction heating effect of pipe materials, such as current frequency f (Hz), current density J (A/m²), and air gap d (mm), are seen as independent variables, while the outer wall temperature of the pipe is seen as the dependent variable. Subsequently, two regression models are established for prediction of the pipe outer wall temperature T on the basis of combining the feature of sample data. It can be seen from Figure 9 that the process parameters and the temperature of the inner and outer walls show a linear change law; thereby a regression Model I is established. However, considering the magnitude difference of the selected values of each parameter,

TABLE 8: Results of regression analysis.

	Model I: $T = b_0f + b_1J + b_2d + C$	Model II: $T = Cf^{b_0}J^{b_1}d^{b_2}$
Regression Coefficients	(0.525, 3.092×10^{-5} , -17.184, -1049.604)	(-33.103, 0.642, 2.061, -0.481)
Sum of Residuals	181575.2825	0.295
Return Square Sum	3712511.687	4.915
Correlation Coefficient r^2	0.953	0.943
F-test Value	129.515	120.585
P	1.029×10^{-20}	2.23×10^{-19}

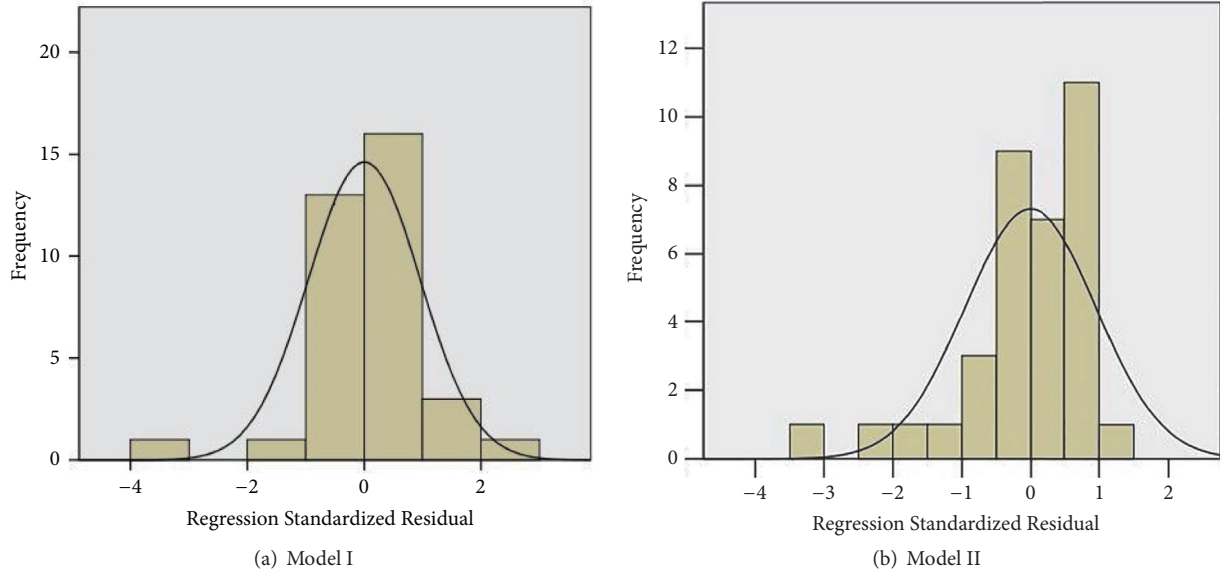


FIGURE 13: Regression standardized residual histogram.

the logarithmic conversion of the sample data is performed to build a regression Model II [30].

$$\text{Regression Model I: } T = b_0f + b_1J + b_2d + C$$

$$\text{Regression Model II: } T = Cf^{b_0}J^{b_1}d^{b_2}$$

Assume that the above two regression models meet the following conditions:

- (1) $\varepsilon_i \sim N(0, \sigma_2)$, $Cov(\varepsilon_i, \varepsilon_j) = 0$, $i \neq j$
- (2) The selected variables are not random and have no multiple linear relationship with each other
- (3) There is a linear relationship between the dependent variable T and the transformed independent variable in the regression model II

The two regression models are analyzed and solved by a multiple regression calculation program, and the results are shown in Table 8.

The regression equations obtained by stepwise regression calculation are as follows:

$$\text{Equation of Model I: } T = 0.525f + 3.092 \times 10^{-5}J - 17.184d - 1049.604$$

$$\text{Equation of Model II: } T = e^{-33.103} f^{0.642} J^{2.061} d^{-0.481}$$

It can be seen from Figure 13 that although the normalized residuals of Model I and Model II are basically normal distribution, comprehensive analysis of the calculation results of Table 8, including the correlation coefficient, sum of squared residuals, and F-test value. It can be seen that Model I has an optimal fitting degree; thus the regression equation (1) is chosen as the mathematical model for predicting the outer wall temperature of large-diameter pipe during the medium-frequency induction heating. In order to verify the accuracy of the regression models, five sets of process parameters are taken as test samples for the numerical simulation and regression model prediction. The results are shown in Table 9.

It can be seen from Table 9 that errors between the simulated data and predicted data are within 5%. The error value needs to be determined according to industry standards. However, it is worth noting that the mathematical model of the outer wall temperature prediction can accurately reflect the mapping relationship between the process parameters of the induction heating and the outer wall temperatures of the pipe. The mathematical model of the outer wall temperature prediction for large-diameter pipe in the induction heating process has certain significance for guiding engineering practice.

TABLE 9: Errors between the numerical simulation and regression model prediction.

Current Frequency f (Hz)	Current Density J (A/m ²)	Air Gap d (mm)	Outer Wall Temperature T (°C)		
			Simulation	Return	Error
1200	6×10^7	30	883	920.1	4.2%
1500	6×10^7	30	1043	1077.6	3.2%
1000	5.5×10^7	30	640	660.5	3.1%
800	6×10^7	30	683	710.1	4.0%
1000	6×10^7	40	626	643.2	2.7%

4. Conclusions

(1) Based on the basic theory of induction heating and analysis of induction heating forming process for large-diameter X80 pipe, the magnetic-thermal coupling issue in the heating process is simulated by sequential coupling method. The influential law of each group's induction heating process parameters (current frequency, current density, and air gap) on the temperature of the inner and outer walls of the pipe has been obtained.

(2) Taking the induction heating process parameters as the test factors, we carry out the orthogonal test design of the process parameters with the difference of the inner and outer wall temperature of the pipe as the evaluation index, the influential degree of each process parameter on the heating effect is determined as air gap > current density > current frequency, and the optimized process parameter sets for the heating bending of the pipe have been obtained using the neural network genetic algorithm, with the current frequency, current density, and air gap which are 1460 Hz, 5.65×10^7 A/m², and 15 mm, respectively.

(3) The linear regression models of two types of pipe temperature have been built based on the simulation results of different heating parameters. By comparing and analyzing the relevant test standards of each regression equation, we have obtained the mathematical model of the outer wall temperature prediction during the induction heating process of the pipe.

(4) From the bend forming practice of X80 pipe, the numerical simulation process parameters sets are somewhat limited. Hopefully, our mathematical analysis method is of a referential significance for practical engineering.

Data Availability

The data used to support the findings of this study are available from the corresponding author upon request.

Conflicts of Interest

The authors declare that they have no conflicts of interest.

Acknowledgments

This work was supported by National Natural Science Foundation of China (NSFC) (no. 51775427)

References

- [1] R. X. Fang and W. S. Cao, "The research of hydraulic technology for large caliber medium frequency heating pipe hydraulic bending machine," *Chinese Hydraulics & Pneumatics*, 2010.
- [2] X. Fang, J. Wang, and W. Cao, "Induction heating of large-diameter thin-walled elbow based on skin effect," *Oil & Gas Storage and Transportation*, vol. 36, no. 8, pp. 958–963, 2017.
- [3] X. Fang, X. Meng, and H. Fan, "Research on Ultra-low and Constant Speed Hydraulic Control System of Large Push-bending Style Pipe Bender," *Machine Tool & Hydraulics*, vol. 19, pp. 61–64, 2017.
- [4] C. Pandey, M. M. Mahapatra, P. Kumar, N. Saini, and J. G. Thakre, "Nano-size Particle Evolution During Heat Treatment of P91 Steel and Their Effect on Micro Hardness," *Transactions of the Indian Institute of Metals*, pp. 1–8, 2017.
- [5] C. Pandey and M. M. Mahapatra, "Effect of Heat Treatment on Microstructure and Hot Impact Toughness of Various Zones of P91 Welded Pipes," *Journal of Materials Engineering and Performance*, vol. 25, no. 6, pp. 2195–2210, 2016.
- [6] C. Zheng, H. Liu, X. Ding, and Q. Fu, "Horizontal Vibration of a Large-Diameter Pipe Pile in Viscoelastic Soil," *Mathematical Problems in Engineering*, vol. 2013, Article ID 269493, 13 pages, 2013.
- [7] C. Pandey, M. Mahapatra, P. Kumar et al., "Some studies on P91 steel and their weldments," *Journal of Alloys & Compounds*, vol. 743, pp. 332–364, 2018.
- [8] S. Q. Pan, X. U. Zhe, and H. E. Bi-Shi, "A Study on Temperature Control for the Billet Electromagnetic Induction Heating Based on Simulation," *Industrial Heating*, vol. 41, no. 6, pp. 25–28, 2012.
- [9] H. Du, J. Li, and Y. Qu, "Mathematical Modeling of Eddy-Current Loss for a New Induction Heating Device," *Mathematical Problems in Engineering*, vol. 2014, Article ID 923745, 7 pages, 2014.
- [10] Y. Wang, C. Liu, and X. Wang, "Influence of induction coil parameter on temperature field of steel plate and choosing of coil size," *Jinshu Rechuli/Heat Treatment of Metals*, vol. 41, no. 4, pp. 178–182, 2016.
- [11] T. D. S. Antonino, P. B. Guimarães, R. D. A. Alcício et al., "Measurements of the Thermophysical Properties of the API 5L X80," *Materials Sciences & Applications*, vol. 5, no. 8, pp. 617–627, 2014.
- [12] Y. H. Zhang, *Numerical Simulation of Induction Heating Temperature Field*, Jiangnan University, 2008.
- [13] Z. QianZhe, *Numerical Simulation and Experimental Study on Induction Heating Process of Steel Bar Production Line*, North China Electric Power University, 2013.

- [14] Z. Tianxu, *Numerical analysis and experimental study on dynamic medium frequency induction heating process of high frequency straight seam welded pipe*, Yanshan University, 2016.
- [15] Y. Chenguang, *Numerical Simulation of Variable Power Induction Heating of 42CrMo Steel Shaft Parts*, Yanshan University, 2010.
- [16] S. Wenjie, *Numerical simulation and experimental study on electromagnetic field and temperature field of large-diameter molten silicon single crystal growth equipment*, Zhejiang University, 2013.
- [17] J. L. Fleming and J. Moser, "A Fourier Approach to Model Electromagnetic Fields Scattered by a Buried Rectangular Cavity," *Mathematical Problems in Engineering*, vol. 2009, Article ID 937327, 22 pages, 2009.
- [18] X. Yi, L. Li, J. Yue et al., "Simulation of coupling of electromagnetic and thermal of intermediate frequency induction heating of pipeline," *Heat Treatment of Metals*, vol. 41, no. 7, pp. 154–158, 2016.
- [19] H. U. Jun, J. Chen, and L. I. Ming, "Research on Drawing Technology of High-strength Steel Rectangular Box Based on ABAQUS," *Hot Working Technology*, 2014.
- [20] S. Liu, H. Shi, and L. Feng, "Transformer harmonic loss model considering skin effect and proximity effect," *Dianli Zidonghua Shebei/Electric Power Automation Equipment*, vol. 35, no. 3, pp. 133–139, 2015.
- [21] Z. Zhao and S.-Y. Zhang, "Self-adaptive step sequential-interaction method and its application in transient-fields coupling problems," *Jisuanji Jicheng Zhizao Xitong/Computer Integrated Manufacturing Systems, CIMS*, vol. 17, no. 7, pp. 1404–1414, 2011.
- [22] Z. Wang, W. Yang, and Y. Song, "The R/S analysis and application in the oil-gas gathering and transportation process," *Petroleum Exploration & Development*, vol. 37, no. 5, pp. 618–622, 2010.
- [23] C. Pandey, A. Giri, and M. M. Mahapatra, "Evolution of phases in P91 steel in various heat treatment conditions and their effect on microstructure stability and mechanical properties," *Materials Science & Engineering A*, vol. 664, pp. 58–74, 2016.
- [24] S. Wang, N. Zhang, L. Wu, and Y. Wang, "Wind speed forecasting based on the hybrid ensemble empirical mode decomposition and GA-BP neural network method," *Journal of Renewable Energy*, vol. 94, pp. 629–636, 2016.
- [25] Z. Sun, H. Yang, and Z. Tang, "Microstructural evolution model of TA15 titanium alloy based on BP neural network method and application in isothermal deformation," *Computational Materials Science*, vol. 50, no. 2, pp. 308–318, 2010.
- [26] C. Bharathi, D. Rekha, and V. Vijayakumar, "Genetic Algorithm Based Demand Side Management for Smart Grid," *Wireless Personal Communications*, vol. 93, no. 2, pp. 481–502, 2017.
- [27] H. S. Madraswala and A. S. Deshpande, "Genetic algorithm solution to unit commitment problem," in *Proceedings of the 2017 International Conference on Nascent Technologies in Engineering, ICNTE 2017*, India, January 2017.
- [28] S. Pal, S. K. Pal, and A. K. Samantaray, "Artificial neural network modeling of weld joint strength prediction of a pulsed metal inert gas welding process using arc signals," *Journal of Materials Processing Technology*, vol. 202, no. 1-3, pp. 464–474, 2008.
- [29] J. Tang, "Study on temperature control effect with pipe-cooling of thick inverted T-shaped concrete pier-wall during construction," *Water Resources & Hydropower Engineering*, 2017.
- [30] C. Pandey, A. Giri, and M. M. Mahapatra, "On the prediction of effect of direction of welding on bead geometry and residual deformation of double-sided fillet welds," *International Journal of Steel Structures*, vol. 16, no. 2, pp. 333–345, 2016.

Research Article

A Parametric Study and Optimization of an Air Conditioning System for a Heat-Loaded Room

Qinghe Yao ¹, Hang Bai,¹ Trevor Hocksun Kwan,¹ and Kiwamu Kase²

¹School of Engineering, Sun Yat-Sen University, 510275, Guangzhou, China

²Advanced Photonics Technology Development Group, RIKEN, 2-1 Hirosawa, Wako, Saitama 351-0198, Japan

Correspondence should be addressed to Qinghe Yao; yaoqhe@mail.sysu.edu.cn

Received 15 June 2018; Revised 24 August 2018; Accepted 4 September 2018; Published 30 September 2018

Academic Editor: Kwang-Yong Kim

Copyright © 2018 Qinghe Yao et al. This is an open access article distributed under the Creative Commons Attribution License, which permits unrestricted use, distribution, and reproduction in any medium, provided the original work is properly cited.

Optimization of an air conditioning system is critical in terms of the transient and steady state behavior of the air distribution along the room and the temperature of the equipment themselves. In this paper, three computational techniques, namely, the standard $k - \epsilon$, RNG $k - \epsilon$, and the $k - \omega$ model, are used to numerically simulate and determine the air distribution in an air-conditioned room. The simulation results for all three methods are verified via a comparison with an experiment involving a room that contains a computer server which generates up to 6 kW of heat. In doing so and by additionally performing an error analysis, it is determined that the $k - \omega$ model produces the most accurate results. The results also indicated that the direction of air supply from the air conditioners has a strong impact on the velocity field and temperature distribution along the room and on the computer server. Hence, many candidate directions of air supply options were selected for study and by conducting a performance evaluation in terms of air temperature around the server, the optimal solution was obtained.

1. Introduction

The design of air-conditioning (AC) system is strongly dependent on the dynamics of the air flow in a room. Traditional measurement methods such as trial and error experiments is often time-consuming and expensive [1]. This is because modifying an existing AC system is generally a difficult and labor-intensive task and it is generally preferred that the optimal design be initially obtained in simulation. Therefore, computational fluid dynamics (CFD) are frequently adopted to design AC systems where the key benefits include reduced time and cost while retaining accurate and valuable results [2, 3]. Moreover, CFD methods also have the advantages of enabling interactive visualization and repeatability [4]. Hence, CFD techniques are currently widely used in air distribution research and subsequently the design of AC systems [5–7].

With reference to other cases, literature studies show that the CFD simulations could be conveniently applied to analyze and predict the indoor air distribution [4, 8, 9], to optimize the heating and cooling performances of the AC system [10, 11], to evaluate the indoor thermal comfort

[12] or to take into account ammonia concentration for livestock [13]. In [14], air conditioning in a museum was studied with a coupled numerical approach of energy and fluid-dynamic analysis. Fariborz H and Chérif MA [15] comprehensively analyzed the validation of two models: COMIS and CONTAM. Furthermore, Li Y and Nielsen PV [16] discussed the major challenges of CFD and finally suggested that CFD technology has not become a replacement for experiment and theoretical analysis in ventilation research and rather it has become an increasingly important partner.

Indeed, because indoor airflow typically involves turbulent dynamics, a turbulence model will be required in the associated CFD simulation. A comparison of various types of $k - \epsilon$ models including standard, renormalization group (RNG), low Reynolds number, and other types was conducted in [17] for analyzing natural and forced convection of indoor air flows. It was concluded that none of the models could accurately simulate anisotropic turbulence or secondary recirculation air dynamics. Alternatively, [18, 19] performed a literature survey on various existing turbulence models (including the various $k - \epsilon$ models

aforementioned) and concluded that there is no model that is universally optimal for any scenario and that the appropriate model is often application specific. More recently, [20] conducted another research on comparing 11 different turbulence models including Reynolds averaged numerical simulation (RANS) models for the wind tunnel application with comparisons to experimental results. They showed that the S-A model and the RNG $k - \varepsilon$ were the most suitable candidates for predicting surface pressure distributions but emphasized that they were unable to evaluate the most appropriate model for predicting turbulence length scales.

Indeed, CFD techniques and turbulence model are well established for simulation air flow distributions in various applications. However, although a comparison of adopting different turbulence models for analyzing natural and forced convective air flow or flow through test samples in wind tunnels currently exists in literature, this is not the case for an air-conditioned room that has a large heat source, a scenario that is commonly encountered in a computer server room. Therefore, this paper analyzes the air distribution of an air-conditioned room that specifically contains an operating computer server that generates up to 6kW of heat. The temperature of air leaving the air conditioner is set to a reference value and the resulting air temperature and pressure dynamics are calculated via the CFD simulation. Three different turbulence models, the standard $k - \varepsilon$, RNG $k - \varepsilon$, and the $k - \omega$ model, are used to analyze the scenario and their accuracy is determined by an experiment involving a real computer server room with temperature measurements. Moreover, the effects of the different air supply directions on air distribution were analyzed in this work and the optimal configuration was determined based on evaluating the AC system's cooling rate and energy efficiency.

2. Method and Governing Equations

Several methods are available for studying the indoor air distribution, such as the traditional measurement and the method of numerical simulation based on the computational dynamics fluid (CFD). In this paper, we adopted the Fluent as the research tool and chose UDF to impose the boundary conditions. The standard wall function was adopted in this work to simulate the flow in the near-wall region, and the SIMPLE algorithm is used to couple the pressure and velocity. To simplify the problem, assumptions are made as follows [4, 21]:

- (i) The air is steady turbulent flow;
- (ii) Indoor air is incompressible and conforms to Boussinesq hypotheses; namely, changes of fluid density have an influence on buoyancy lift only;
- (iii) Considering the room simulated is with good air tightness, so air leakage effect is out of consideration;
- (iv) Indoor air is the Newton fluid, and its viscosity is isotropic;
- (v) Ignore the energy dissipation caused by the viscous effect in the energy equation;

- (vi) Due to the adjacent houses, all equipped with air conditioning, interior wall and floor can be regarded as adiabatic boundary condition without temperature difference.

Reynolds time-averaged control equations with Boussinesq approximation are adopted in this work. By the assumptions above, the governing equations are as follows:

$$\begin{aligned} \frac{\partial \bar{u}_i}{\partial x_i} &= 0 \\ \rho \frac{\partial \bar{u}_i}{\partial t} + \rho \bar{u}_j \frac{\partial \bar{u}_i}{\partial x_j} &= -\frac{\partial \bar{p}}{\partial x_i} + \mu \frac{\partial^2 \bar{u}_i}{\partial x_j \partial x_j} - \rho \frac{\partial \overline{u'_i u'_j}}{\partial x_j} + \rho \bar{f}_i, \end{aligned} \quad (1)$$

where \bar{u}_i is Reynolds mean velocity in i direction; u' is fluctuation velocity; $-\rho \overline{u'_i u'_j}$ is Reynolds stress; ρ is fluid density; μ is kinematic viscosity; p is pressure; and f_i is unit mass force.

To compare and find a suitable simulation to this model, the numerical results of standard $\kappa - \varepsilon$, RNG $\kappa - \varepsilon$ and $\kappa - \omega$ turbulence models are compared in this work, where for standard $\kappa - \varepsilon$, the κ equation, and ε equation are

$$\begin{aligned} \frac{\partial (\rho \kappa)}{\partial t} + \frac{\partial (\rho \kappa u_i)}{\partial x_i} &= \frac{\partial}{\partial x_j} \left[\left(\mu + \frac{\mu_t}{\sigma_\kappa} \right) \frac{\partial \kappa}{\partial x_j} \right] + G_\kappa + G_b \\ &\quad - \rho \varepsilon - Y_M + S_\kappa \\ \frac{\partial (\rho \varepsilon)}{\partial t} + \frac{\partial (\rho \varepsilon u_i)}{\partial x_i} &= \frac{\partial}{\partial x_j} \left[\left(\mu + \frac{\mu_t}{\sigma_\varepsilon} \right) \frac{\partial \varepsilon}{\partial x_j} \right] \\ &\quad + C_1 \frac{\varepsilon}{k} (G_\kappa + C_3 G_b) - C_2 \rho \frac{\varepsilon^2}{k} \\ &\quad + S_\varepsilon, \end{aligned} \quad (2)$$

where ε is defined as

$$\varepsilon = \frac{\mu}{\rho} \overline{\left(\frac{\partial u'_i}{\partial x_k} \right) \left(\frac{\partial u'_i}{\partial x_k} \right)} \quad (3)$$

and the turbulent viscosity is expressed as

$$\mu_t = \rho C_\mu \frac{k^2}{\varepsilon}, \quad (4)$$

where G_κ is turbulent kinetic energy product; G_b is turbulent kinetic energy caused by buoyancy; Y_M is influence of fluctuating expansion of compressible turbulence on total dissipation rate; S_κ and S_ε are source terms depending on the conditions; C_i ($i = 1, 2, 3$) is an empirical constant.

For the RNG $\kappa - \varepsilon$, the κ equation and ε equation are

$$\begin{aligned} \frac{\partial(\rho k)}{\partial t} + \frac{\partial(\rho k u_i)}{\partial x_i} &= \frac{\partial}{\partial x_j} \left[(\alpha_k \mu_{eff}) \frac{\partial k}{\partial x_j} \right] + G_k + G_b \\ &\quad - \rho \varepsilon - Y_M + S_k \\ \frac{\partial(\rho \varepsilon)}{\partial t} + \frac{\partial(\rho \varepsilon u_i)}{\partial x_i} &= \frac{\partial}{\partial x_j} \left[(\alpha_\varepsilon \mu_{eff}) \frac{\partial \varepsilon}{\partial x_j} \right] \\ &\quad + C_1 \frac{\varepsilon}{k} (G_k + C_3 G_b) - C_2 \rho \frac{\varepsilon^2}{k} \\ &\quad - R + S_\varepsilon, \end{aligned} \quad (5)$$

where

$$\mu_{eff} = \mu + \mu_t \quad (6)$$

and μ_t is the same as in (4). $1/\alpha_k$ is effective Prandtl number of turbulent kinetic energy; C_μ is effective Prandtl number of dissipation rate; for the high Reynolds number problem $C_\mu = 0.00845$.

For the $\kappa - \omega$ turbulence model, the κ equation and ω equation are

$$\begin{aligned} \frac{\partial}{\partial t}(\rho k) + \frac{\partial}{\partial x_i}(\rho k u_i) &= \frac{\partial}{\partial x_i} \left(\Gamma_k \frac{\partial k}{\partial x_j} \right) + G_k - Y_k + S_k \\ \frac{\partial}{\partial t}(\rho \omega) + \frac{\partial}{\partial x_i}(\rho \omega u_i) &= \frac{\partial}{\partial x_j} \left(\Gamma_\omega \frac{\partial \omega}{\partial x_j} \right) + G_\omega - Y_\omega + S_\omega, \end{aligned} \quad (7)$$

where G_ω is the kinetic energy produced by ω equation; Γ_k and Γ_ω are the diffusion rates of k and ω , respectively; Y_k and Y_ω are the effect of turbulence caused by diffusion; S_k and S_ω are the source terms depending on the conditions and select the $\kappa - \omega$ model when setting up the boundary conditions.

3. Modeling and Experimental Setup

An air-conditioned room involving a small computer center in the Sun Yat-sen University is selected as the research subject for this paper. The airflow parameter distributions throughout this room will be analyzed. The computer room consists of three tables, a locker, a computer server, and its uninterruptable power supply (UPS). In this room, the air conditioning system consists of two separate air conditioners with 30° placed at the back of the room, as shown in Figure 1. The dimension of the model are as follows:

- (i) Door dimensions: 2.1 m \times 0.9 m;
- (ii) Locker dimensions: 1.8 m \times 0.45 m \times 1.8 m;
- (iii) Table dimensions: 3 \times 1.5 m \times 0.75 m \times 0.85 m;
- (iv) The computer server and its two associated equipment: 0.6 m \times 0.96 m \times 1.98 m; 0.94 m \times 0.78 m \times 1.2 m; 0.25 m \times 0.51 m \times 0.57 m;
- (v) Room dimensions: 7.20 m \times 6.70 m \times 2.75 m;
- (vi) Air conditioner: 0.60 m \times 0.35 m \times 1.86 m;

3.1. The Model and Mesh Generation. The software of ANSYS ICEM CFD is adopted in this study to generate the model and its grid. In order to improve grid quality, local mesh refinement for special boundaries and smoothing are performed. Different mesh sizes have been used to check the grid in dependency. And after considering both accuracy and economics, the computational domain was meshed into around 9,090,502 cells as illustrated in Figure 2.

And in this paper, the treatment of the near wall boundary is to make $y^+ \sim 1$, where y^+ is the dimensionless distance to the wall. For the turbulent flow in the fully developed area of the solid wall, it can be divided into the near wall area and the turbulent core area. In this research we pay more attention to the flow in the near wall area. And the near wall area can be further divided into an adhesive bottom layer, a transition layer, and a logarithmic layer, and these layers are the relationship between the dimensionless velocity u^+ and y^+ . Generally, y^+ of the viscous underlayer should approach 1.

3.2. Boundary Condition Settings. Before the numerical calculation, we classified the boundaries and measured the necessary parameters as follows:

(a) *Inlet Air Temperature.* To get the temperature variation curve, nine temperature sensors are uniformly distributed in the air inlet of air conditioner (see Figure 3). The functions of the average temperature curves are as follows:

Right Air-Conditioning

$$f_1(t) = A_0 + \sum_{i=1}^5 A_i \cos(i\omega t) + \sum_{i=1}^5 B_i \sin(i\omega t), \quad (8)$$

where $f_1(t)$ is air temperature supplied from right air conditioner; t is time; ω is angular frequency, $A_0=296.4$, $A_1=1.101$, $A_2=-1.019$, $A_3=0.9897$, $A_4=0.3855$, $A_5=0.1527$, $B_1=0.5416$, $B_2=-0.6437$, $B_3=-0.741$, $B_4=-0.3257$, $B_5=-0.1593$, and $\omega=0.07797$.

Left Air-Conditioning

$$f_2(t) = A_0 + \sum_{i=1}^6 A_i \cos(i\omega t) + \sum_{i=1}^6 B_i \sin(i\omega t), \quad (9)$$

where $f_2(t)$ is air temperature supplied from left air conditioner; t is time; ω is angular frequency, $A_0=300.1$, $A_1=6.145$, $A_2=-1.242$, $A_3=-3.669$, $A_4=-1.542$, $A_5=0.3772$, $A_6=0.3574$, $B_1=-5.895$, $B_2=-6.146$, $B_3=-1.3$, $B_4=2.122$, $B_5=1.671$, $B_6=0.3795$, and $\omega=0.06637$.

(b) *Inlet Air Velocity.* The average air velocity of right air conditioner is 3.37 m/s and that of left air conditioner is 3.88 m/s.

(c) *Inlet Air Temperature of Server.* The exhaust air temperature from server varies over time, but it fluctuates little. Therefore, we take an average temperature of 303.85 K.

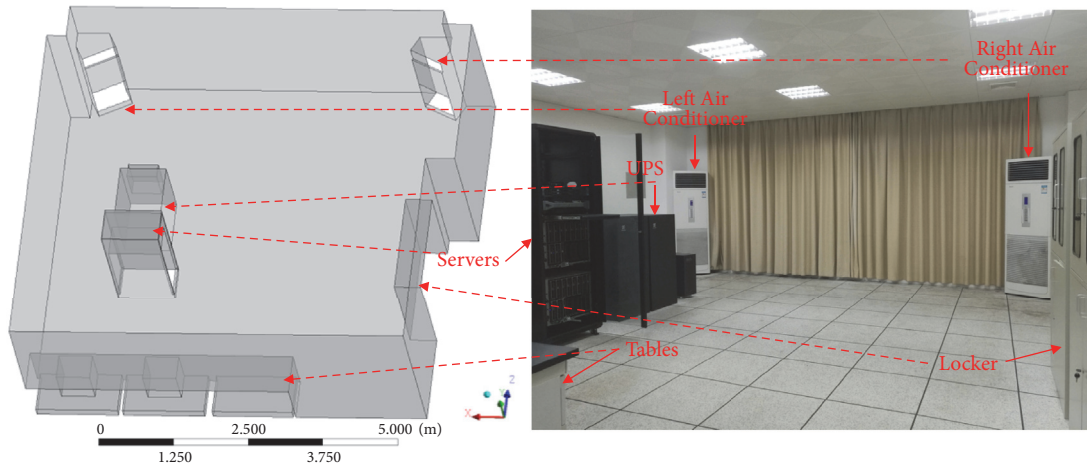


FIGURE 1: Schematic of the server room to be air conditioned.

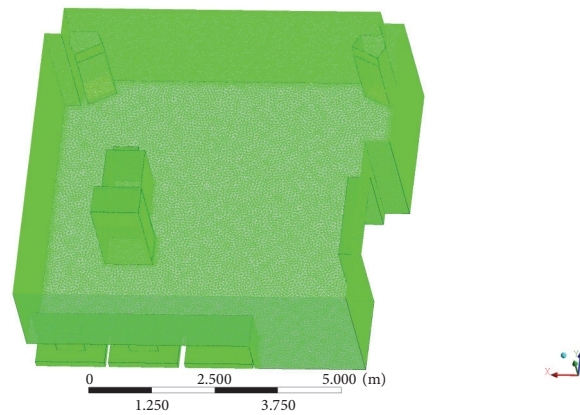


FIGURE 2: Surface mesh generation.

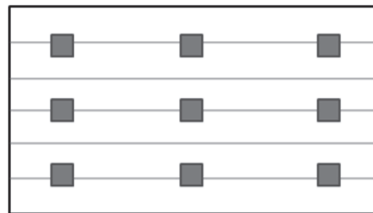


FIGURE 3: The distribution of sensors in the inlet.

(d) *Inlet/Outlet Air Speed of Server.* It is assumed that the speed of the cooling air entering the server equals the average velocity of air supplied from the server, which is 1.31 m/s.

(e) *Initial Indoor Air Temperature: 303.65 K.* The simulation is based on the preset operation conditions. And these conditions are set according to the measurement data. As is shown in Figure 1, the air supply outlets of air conditioners and server are set as the speed inlets. The return air inlets are set as the opening-outlet boundaries with the temperature of 298 K. And the front plane of the server is set as the speed outlet. The other boundaries are set to nonslip wall,

wall insulation. Table 1 shows detail values of boundary conditions.

In order to study the influence of different air supply direction on indoor airflow, we consider nine different combinations of air flow supply directions from the two separated air conditioners and, for the sake of brevity, these shall be called air supply combinations. The configuration of each combination is shown in Table 2. In this table, 0 degree means parallel with respect to the ground. Also, positive values are facing upwards towards the ceiling and negative values are facing downwards towards the ground. The other parameters such as the supply air wind velocity are unchanged.

TABLE 1: The preset operation conditions for simulation.

Parameters	Value	Unit
Inlet air velocity of right AC	3.37	m/s
Inlet air velocity of left AC	3.88	m/s
Inlet air velocity of Server	1.31	m/s
Inlet air temperature of right AC	f_1	K
Inlet air temperature of left AC	f_2	K
Outlet air temperature of right AC	298	K
Outlet air temperature of left AC	298	K
Air temperature of server outlet	303.85	K
Air temperature of server outlet	1.31	m/s

TABLE 2: Combinations of air supply direction.

Operating conditions	Right air conditioning	Left air conditioning
1	+35°	+35°
2	+35°	0
3	+35°	-35°
4	0	+35°
5	0	0
6	0	-35°
7	-35°	+35°
8	-35°	0
9	-35°	-35°

TABLE 3: Error analysis of the three turbulence models.

Turbulence model	\bar{E}	U
$k - \varepsilon$	0.887	0.736
RNG $k - \varepsilon$	0.890	0.864
$k - \omega$	0.680	0.681

4. Result and Discussion

4.1. Indoor Air Temperature Measurement. In order to analyze the accuracy of the results calculated by three turbulence models, we measured the temperature in the room. In this case study, the main way of the server cooling is that controlling the air temperature of the environment around the server. Therefore, after fully considering the influence of the air conditioning and the location of the main working zone (the server area), two rows of measuring sensors were set up at different height (172 cm and 70 cm) between the air conditioning and the server in the back of the room as shown in Figure 4(a). The area, in which the measuring sensors are located, is part of the working zone and close to the air conditioning with complicated airflow, and it has a certain representativeness. Figure 4(b) shows the detail distribution of the measuring points: the upper (172 cm) and lower (70 cm) rows each contains five sensors.

4.2. Validation and Error Analysis. In this part, we presented the simulation results calculated by different turbulence models and discussed their accuracy by comparing the measurement data. This investigation used absolute calculation

error and uniformity of errors to evaluate the accuracy with different turbulence models [1, 14].

The absolute calculation error is the difference between the simulation values with the turbulence models and the actual values, i.e.,

$$E_{Ti} = |v_{ni} - v_{mi}|, \quad i = 1, \dots, 10, \quad (10)$$

where E_{Ti} represents the absolute error between the simulation temperature value and the actual value at sensor i ; v_{ni} is the numerical simulation temperature value; v_{mi} is the actual value.

The uniformity of errors evaluates whether or not different turbulence models would lead to an uneven simulation error distribution

$$U = \sqrt{\frac{1}{N-1} \sum_{i=1}^N (E_{ni} - \bar{E})^2}, \quad (11)$$

where U is the uniformity of errors for air temperature; N is the number of sensors, E_{ni} indicates the simulation error of the air temperature at point i ; and \bar{E} is the averaged simulation error of the air temperature.

Table 3 lists the average simulation errors and the uniformity of errors for the flow domain, the working zone, calculated by (10) and (11), respectively. For the three turbulence models, with the same computational conditions, the $K - \omega$ model yielded a smaller average calculated error and higher uniformity than the others [1, 14]. For the $k - \varepsilon$, RNG $k - \varepsilon$, and $K - \omega$ models the maximum relative calculated errors of the air temperature were 0.98%, 1.39%, and 0.96%, respectively.

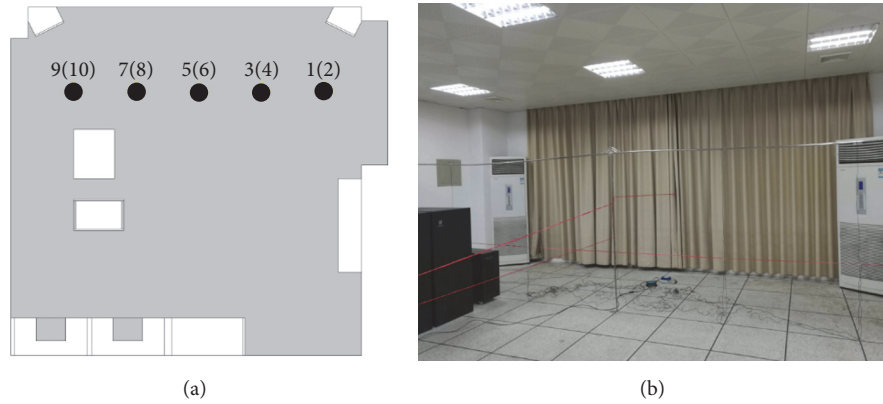


FIGURE 4: Measuring sensors distribution (a) and test scenario (b).

The errors of the three models are all in reasonable limits and the $K - \omega$ model performed best.

As shown in Figure 5, the errors between simulated values and measured values are different at different points. At the points 1, 2, 4, 5, 6, 8, and 10, the simulated values of all the three turbulence models are well in agreement with the measured ones, whereas at the points 3, 4, and 9, the errors are bigger. It might result from the certain error between simulation results by the turbulence models and the real physical air distributions or the experimental instrument is not that precise. Generally, the simulation result of the $K - \omega$ model shows good agreement with the experimental findings with the error range from 0.006K to 0.910K. And the RNG $k - \epsilon$ and standard $k - \epsilon$ models have similar performance. It should be noted that the biggest error appears at the point 3 and the calculation errors of the lower row measurement points (70cm) were smaller. This difference arose because the airflow in the upper area (172cm) is more complex and chaotic, so that it is more difficult to numerically calculate this area accurately.

In summary, it can be concluded that the $k - \omega$ turbulence model has the better reliability than that of the others in this study, and the simulation result can predict the real physic process. It must be pointed out that because of the grid generation, simplification of the physical model, computational method, and other factors, the deviation between the simulated values and the measurement data is large (> 1.0 K) at some measuring points. But on the whole, the numerically calculated results are reasonable and reliable.

4.3. Analysis of the Air Supply Direction. Based on the conclusion of last section, the $k - \omega$ model was used to simulate the air distribution for analyzing the influence of air supply direction. In this case study, the server heat dissipation is controlled by ambient temperature; that is, the environmental temperature affects the server cooling directly. Therefore, the streamline pictures and temperature field cloud pictures of typical cross section near the cooling windward side of server (at $X=3.6$) were analyzed.

The parallel air supply direction of both air conditioners (condition 5 in Table 2) is applying now in this air-conditioned room. Therefore, in the following discussion

we chose it as a reference. Figures 6 and 7 show the pictures of streamlines and temperature fields cloud from condition 1 to condition 9, respectively. It could be observed that, different combinations of different air supply directions of two air conditioners have a significant influence on the fluid field and temperature distribution.

Due to the existence of a single the heat source (server) the original symmetrical the AC system is no longer symmetrical in the aspect of layout. That is why the obvious difference arose between the conditions, for instance, condition2 and condition 4. As is shown in Figure 7, there are different situations of local higher temperature areas distribution and temperature stratification in the corner regions (mainly upper left) under all combination conditions. The main reason of this phenomenon is that, the high temperature air supplied from the server lifting and accumulating at the ceiling, and the exhausted air cannot be discharged in time. These partial hot spots could induce indoor heat island effect, which have adverse effects on indoor air organization and cooling efficiency [22, 23]. In Figures 7(f) and 7(h), the local high temperature areas under condition 6 and 8 are evidently larger than that under other conditions, and these areas even extend directly to the main working zone where the server located, namely, the area we concerned in this study (red circle in the figure). Meanwhile the phenomena of temperature stratification are more obvious under these conditions. Comparatively speaking, the temperature distribution of the main working zone is more uniform and there are fewer partial hot spots under the conditions 1, 4, and 7 [24, 25].

In order to optimize the air supply direction, we further analyzed the streamlines of conditions 1, 4, and 7. As represented in Figure 6(a), there was no wide range recirculation and the air velocity distribution is also relatively uniform in the main working zone under the condition 1. But there were two small vortices near the server, which would increase the velocity gradient between the upper and lower regions. In Figure 6(d), it was found that the whole area is divided into different parts by the vortices, the streamlines were very messy, and there was a recirculation containing two vortices controlled the air organization near the server. And

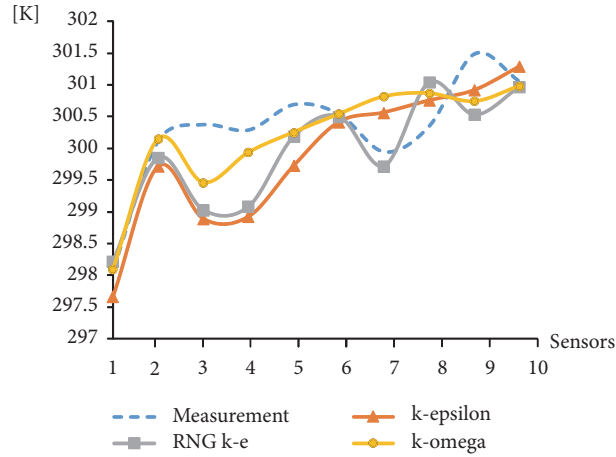


FIGURE 5: The comparison of simulation results and measurement.

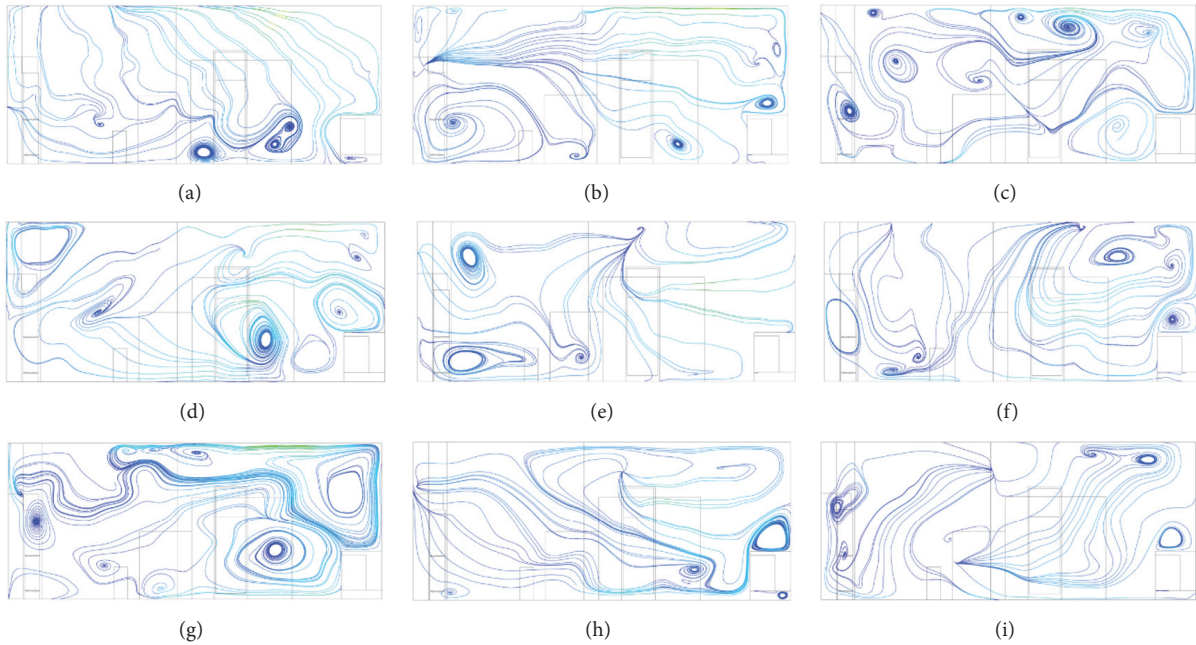


FIGURE 6: Streamlines, (a)-(i) corresponding the condition 1 to condition 9.

in Figure 6(g), air motion of the whole area was controlled by two large recirculation (upper and lower) containing two and four vortices, respectively. The recirculation moves along the surface of the enclosure structure and almost the entire working area is controlled by the bottom swing vortex. The velocity distribution, gradient, and the streamlines of the condition 7 perform better than that of the others.

Table 4 illustrates the different average cooling rates of the all conditions. The difference between all cooling rates is very small. We found that the maximum appearing in condition 4 is 0.032 K/s, the minimum is 0.022 K/s for the condition 9, and the cooling rate of condition 5 is 0.030 K/s.

In order to analyze the energy efficiency in the main working zone under different conditions, the energy

utilization coefficient (EUC) that was adopted in [26, 27] is adopted here and is presented in

$$\eta = \frac{T_p - T_o}{\bar{T} - T_o} \tag{12}$$

where η is the energy utilization coefficient, T_o is the temperature of air supplied from the air conditioning, T_p represents the temperature of the air returns to the air conditioners, and \bar{T} is the average temperature of the air in working zone.

As regards this analysis, all the supply combinations have good performance on the energy utilization coefficient (>1) [21, 26, 27] except for the condition 9 (see Table 5). The best performance rose in the case of combination 2 (1.243) and the coefficient of condition 5 is 1.231. Furthermore, the difference

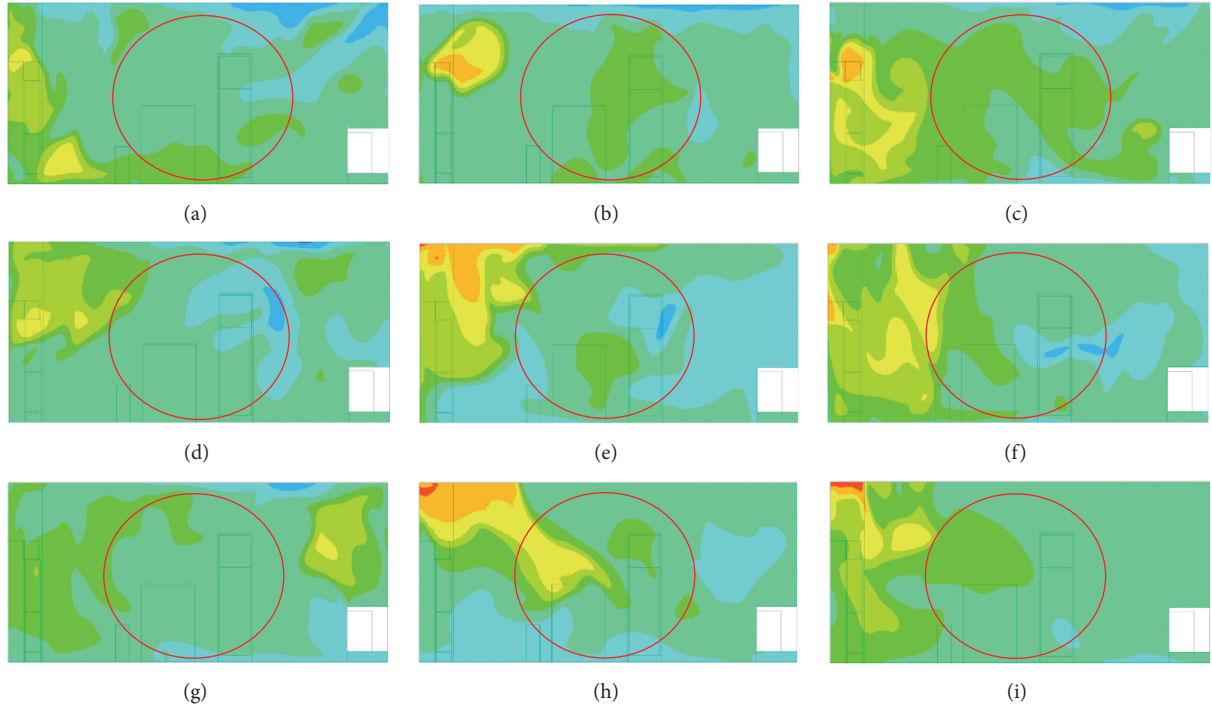


FIGURE 7: Temperature contour, (a)-(b) corresponding condition 1 to condition 9.

TABLE 4: Cooling rates of nine conditions.

	1	2	3	4	5	6	7	8	9
Cooling rate (K/s)	0.031	0.028	0.025	0.032	0.030	0.029	0.029	0.028	0.022

TABLE 5: Energy utilization coefficient of different conditions.

	1	2	3	4	5	6	7	8	9
η	1.165	1.243	1.042	1.222	1.231	1.0629	1.152	1.178	0.998

among all conditions is quite small; namely, the air supply directions have a little influence on the energy utilization.

To sum up, in terms of the cooling rate, energy utilization coefficient, and the distributions of velocity and temperature, we discussed the influence of different combinations of air supply direction. The result shows that the AC system has defects. After a comprehensive analysis, we found that combination 7 has the best performance, so it is recommended that the air supply direction should be adjusted to the combination 7 (-35° and $+35^\circ$) without changing the other settings.

5. Conclusion

In this paper, three turbulence models, namely, the standard $k-\varepsilon$, RNG $k-\varepsilon$, and the $k-\omega$ model, were used to simulate air distributions for a conditioning room containing a high-powered computer server in CFD simulations. Several configurations of the air supply directions were studied and the results were all compared with that of a real experiment.

After performing a detailed evaluation of the obtained results, the following conclusions are obtained:

(1) By comparing the three studied turbulence models with that of the experimental results, it is found that the $k-\omega$ method produced the most accurate results. While the results of the standard $k-\varepsilon$ and RNG $k-\varepsilon$ were found to be similar, they were also found to have a larger relative error with respect to the experiment than that of the $k-\omega$ method where the relative errors are calculated to, be respectively, 0.983%, 1.393%, and 0.96%.

(2) By studying different air supply directions configurations, it is found that there is indeed a unique air supply directions combination that would provide the most stable velocity field and temperature distribution. In the scenario of this paper, it is found that combinations 7 and 8 (of Table 2) involved less vortices and turbulent flows, while in combinations 3 and 4 there are more chaotic and complex airflows. With regards to temperature distribution, combinations 4 and 7 were found to have much smoother temperature gradients than that of conditions 8 and 9. Overall, it can be

concluded that there is certainly a unique combination of the air supply directions that provides the optimal velocity and temperature field distributions and this is found to be condition 7 (Table 2) for the scenario studied in this paper.

(3) In addition, the analysis in this paper also indicated that the air supply directions have little influence on the cooling rate and energy utilization coefficient. The maximum cooling rate is found to be 0.032 K/s for combination 4 and the minimum one is 0.022 K/s for the combination 9. In the meantime, the energy utilization coefficients ranged from 0.998 (for combination 9) to 1.243 (for combination 2).

Data Availability

The data used to support the findings of this study are available from the corresponding author upon request.

Conflicts of Interest

The authors declare that they have no conflicts of interest.

Acknowledgments

This work was partly supported by Key project of national key R&D program for HPC under Grant no. 2016YFB0200603 and Special Program for Applied Research on Super Computation of the NSFC-Guangdong Joint Fund (the third phase) under Grant no. U1501501. The project of Guangzhou Science and Technology Program (Grant 655 no. 201704030089) also supports this research.

References

- [1] Y. Huang, X. Shen, J. Li et al., "A method to optimize sampling locations for measuring indoor air distributions," *Atmospheric Environment*, vol. 102, pp. 355–365, 2015.
- [2] J. F. Karlsson and B. Moshfegh, "Investigation of indoor climate and power usage in a data center," *Energy and Buildings*, vol. 37, no. 10, pp. 1075–1083, 2005.
- [3] J. Cho, T. Lim, and B. S. Kim, "Measurements and predictions of the air distribution systems in high compute density (Internet) data centers," *Energy and Buildings*, vol. 41, no. 10, pp. 1107–1115, 2009.
- [4] L. Yang, M. Ye, and B.-J. he, "CFD simulation research on residential indoor air quality," *Science of the Total Environment*, vol. 472, pp. 1137–1144, 2014.
- [5] Z. Ma and S. Wang, "Building energy research in Hong Kong: A review," *Renewable & Sustainable Energy Reviews*, vol. 13, no. 8, pp. 1870–1883, 2009.
- [6] A. Fouquier, S. Robert, F. Suard, L. Stéphan, and A. Jay, "State of the art in building modelling and energy performances prediction: A review," *Renewable & Sustainable Energy Reviews*, vol. 23, pp. 272–288, 2013.
- [7] R. J. Dear, T. Akimoto, E. A. Arens et al., "Progress in thermal comfort research over the last twenty years," *Indoor Air*, vol. 23, no. 6, pp. 442–461, 2013.
- [8] M. Cehlin, T. Karimipanh, and U. Larsson, "Unsteady CFD simulations for prediction of airflow close to a supply device for displacement ventilation," in *Proceedings of the 13th International Conference on Indoor Air Quality and Climate, Indoor Air 2014*, pp. 47–54, Hong Kong, July 2014.
- [9] C. Huang, J. Lee, W. Yu, and W. Yu, "Study of the temperature flow field change by air-conditioning system in a indoor circular stadium," in *Proceedings of the 2011 International Conference on Consumer Electronics, Communications and Networks (CEC-Net)*, pp. 3568–3571, Xianning, China, April 2011.
- [10] X. Cui, K. J. Chua, and W. M. Yang, "Numerical simulation of a novel energy-efficient dew-point evaporative air cooler," *Applied Energy*, vol. 136, pp. 979–988, 2014.
- [11] R. Qi and L. Lu, "Energy consumption and optimization of internally cooled/heated liquid desiccant air-conditioning system: A case study in Hong Kong," *Energy*, vol. 73, pp. 801–808, 2014.
- [12] D. Wang, Z. Zhang, L. Han, and L. Li, "Numerical simulation on air conditioning system and flow field of passenger compartment of type-A subway," *Pain*, vol. 152, no. 6, pp. 1317–1326, 2011.
- [13] T. Norton, J. Grant, R. Fallon, and D.-W. Sun, "Assessing the ventilation effectiveness of naturally ventilated livestock buildings under wind dominated conditions using computational fluid dynamics," *Biosystems Engineering*, vol. 103, no. 1, pp. 78–99, 2009.
- [14] F. Ascione, L. Bellia, and A. Capozzoli, "A coupled numerical approach on museum air conditioning: Energy and fluid-dynamic analysis," *Applied Energy*, vol. 103, pp. 416–427, 2013.
- [15] H. Fariborz and M. A. Chérif, "A comprehensive validation of two airflow models - COMIS and CONTAM," *Indoor Air*, vol. 6, no. 4, pp. 278–288, 1996.
- [16] Y. Li and P. V. Nielsen, "Commemorating 20 years of Indoor Air: CFD and ventilation research," *Indoor Air*, vol. 21, no. 6, pp. 442–453, 2011.
- [17] Q. Chen, "Comparison of different k- ϵ models for indoor air flow computations," *Numerical Heat Transfer, Part B: Fundamentals*, vol. 28, no. 3, pp. 353–369, 1995.
- [18] Z. J. Zhai, Z. Zhang, W. Zhang, and Q. Y. Chen, "Evaluation of various turbulence models in predicting airflow and turbulence in enclosed environments by cfd: Part 1—summary of prevalent turbulence models," *HVAC&R Research*, vol. 13, no. 6, pp. 853–870, 2007.
- [19] Z. Zhang, W. Zhang, Z. J. Zhai, and Q. Y. Chen, "Evaluation of various turbulence models in predicting airflow and turbulence in enclosed environments by CFD: Part 2—comparison with experimental data from literature," *HVAC&R Research*, vol. 13, no. 6, pp. 871–886, 2007.
- [20] B. Li, J. Liu, F. Luo, and X. Man, "Evaluation of CFD Simulation Using Various Turbulence Models for Wind Pressure on Buildings Based on Wind Tunnel Experiments," in *Proceedings of the 9th International Symposium on Heating, Ventilation and Air Conditioning, ISHVAC 2015 Joint with the 3rd International Conference on Building Energy and Environment, COBEE 2015*, pp. 2209–2216, China, July 2015.
- [21] J. Q. Yang and M. J. Li, "Numerical simulation of energy saving at different air supply angles in air-conditioned room," *Applied Mechanics and Materials*, vol. 385–386, pp. 263–267, 2013.
- [22] A. Vukovic, "Data centers: Network power density challenges," *ASHRAE Journal*, vol. 47, no. 4, pp. 55–59, 2005.
- [23] J. Rambo and Y. Joshi, "Modeling of data center airflow and heat transfer: State of the art and future trends," *Distributed and Parallel Databases*, vol. 21, no. 2-3, pp. 193–225, 2007.

- [24] Y. Maeda, Y. Seshimo, and T. Okazaki, "Study of a cooling system for the telecommunication base site," in *Proceedings of the American Society of Heating, Refrigerating and Air-Conditioning Engineers, ASHRAE 2005 Annual Meeting*, pp. 746–755, USA, June 2005.
- [25] J. Choi, J. Jeon, and Y. Kim, "Cooling performance of a hybrid refrigeration system designed for telecommunication equipment rooms," *Applied Thermal Engineering*, vol. 27, no. 11–12, pp. 2026–2032, 2007.
- [26] N. Mao, M. Song, and S. Deng, "Application of TOPSIS method in evaluating the effects of supply vane angle of a task/ambient air conditioning system on energy utilization and thermal comfort," *Applied Energy*, vol. 180, pp. 536–545, 2016.
- [27] D. Qi, L. Wang, and R. Zmeureanu, *Large Eddy Simulation of Thermal Comfort and Energy Utilization Indices for Indoor Airflows*, Ashrae Transactions, 2013.

Review Article

Design Optimization of the Centrifugal Pumps via Low Fidelity Models

M. Hamid Siddique,¹ Arshad Afzal ,² and Abdus Samad ¹

¹Department of Ocean Engineering, Indian Institute of Technology Madras, Chennai 600036, India

²Department of Mechanical Engineering, Indian Institute of Technology Kanpur, Kanpur 208016, India

Correspondence should be addressed to Arshad Afzal; aafzal@iitk.ac.in

Received 14 March 2018; Revised 7 May 2018; Accepted 20 May 2018; Published 21 June 2018

Academic Editor: Petr Krysl

Copyright © 2018 M. Hamid Siddique et al. This is an open access article distributed under the Creative Commons Attribution License, which permits unrestricted use, distribution, and reproduction in any medium, provided the original work is properly cited.

Low fidelity model assisted design optimization of turbomachines has reduced the total computational and experimental costs. These models are called surrogate models which mimic the actual experiments or simulations. The surrogate models can generate thousands of approximate results from a few samples, making it easy to locate the optimal solution. Ample articles reported surrogate assisted design optimization of centrifugal pumps. In this article, the authors try to give a brief overview of the surrogate based optimization technique along with its historical applications and trend of the recent use. The various key design parameters which affect the performance of the centrifugal pump have also been discussed. The effectiveness of the surrogate based optimization technique and corresponding performance metrics have been discussed.

1. Introduction

A centrifugal pump is a type of rotodynamic pump, which has two basic components, i.e., impeller, a rotary part, and a volute casing, which is a stationary part (Figure 1). The impeller adds kinetic energy to pumping fluid and the volute casing converts kinetic energy into pressure energy. The complexity of the internal flow in the pump is due to the sudden entrainment of fluid at the eye of the impeller, flow separation, reverse flow, and cavitation formation. Sometimes, strong swirl and adverse pressure gradient at the suction and pressure side of the impeller blade causes inlet recirculation and flow separation in the flow passage. This phenomenon is severe at off-design working condition of a centrifugal pump [1–7]. The flow physics inside the blade passage can be analyzed by simulating the complex pump domain either experimentally or computationally which help to understand the performance of the impeller at both design and off-design conditions [8–16].

The optimization of the centrifugal pump has been carried out since 1940s with the help of experimental techniques [17, 18]. Advancement in computational facilities has

further improved the optimization techniques. Now, in recent decade, the use of surrogate base optimization techniques has emerged as a new technique with has capability of handling large design parameters for the optimization (Table 1). The centrifugal pump design optimization with objectives to improve head and efficiency is influenced by several design parameters such as the number of the blades, inlet and exit blade angles, wrap angles, blade profile curves, which has been discussed later in this paper. So, a proper understanding of design parameter and handling a larger number of design parameters can give better optimized designs.

In this paper, a review is made to understand surrogate assisted optimization techniques for centrifugal pump. The robustness and ease of using surrogate models with computational simulations are discussed along with the major design parameters which affect the pump performance.

2. A Brief of Surrogate Models

The surrogate models such as response surface approximation (RSA), radial basis neural network (RBNN), kriging (KRG), and support vector machine (SVM) are low fidelity

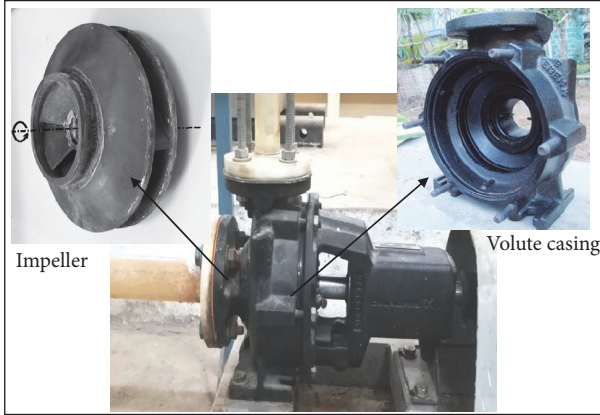


FIGURE 1: Basic components of centrifugal pump.

regression models constructed using data drawn from high-fidelity models. It provides fast approximations of objectives and constraints at new design points making the optimization studies easy and feasible. This technique has already been used in the area of aerospace systems, medical science, business management, and transportations but using it in the area of engineering design has recently been adopted [19–27]. The various types of surrogate models are described below.

2.1. Response Surface Using RSA Model. The response surface approximation method (RSA) is a statistical method to explore the relationship between variables and objectives. This method was invented by Box and Wilson [28], later a procedure for tracing polynomial function for discrete responses given by Myers and Montgomery [29]. This polynomial function represents the relationship of the objective function with the design variables. Suppose an objective function (y) which can be expressed as

$$y = F(x_1, x_2) + e \quad (1)$$

If we need to express the response surface in terms of linear equation using statistical method i.e., first-order model, then (1) can be written as

$$y = a_0 + a_1x_1 + a_2x_2 + e \quad (2)$$

And if there is a curvature in the response surface, then the second-order model of higher order polynomial can be used such as

$$y = a_0 + a_1x_1 + a_2x_2 + a_{11}x_{11}^2 + a_{22}x_{22}^2 + a_{12}x_1x_2 + e \quad (3)$$

This can also be represented as second-order polynomial, i.e., as the response function,

$$y = a_0 + \sum_{j=1}^n a_j x_j + \sum_{j=1}^n a_{jj} x_j^2 + \sum_{i \neq j}^n a_{ij} x_i x_j + e \quad (4)$$

where n is the number of design variables and x and a are the regression coefficients which can be calculated as $(n+1) \times (n+2)/2$.

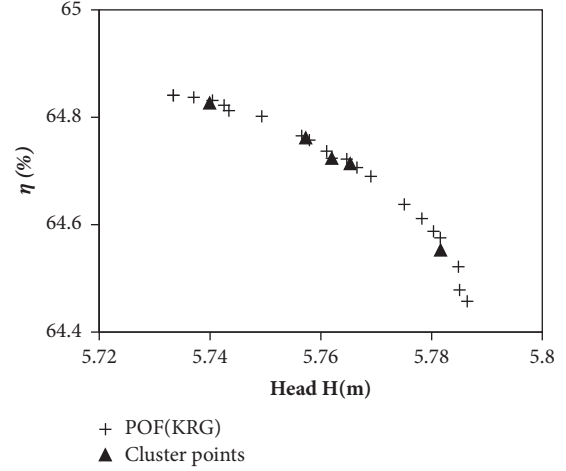


FIGURE 2: Pareto optimal front (Siddique et al. 2017).

The RSA was used by Wahba and Tournlidakis [30] to design the design of blade profiles for centrifugal pump. Kim et al. [31] optimized the centrifugal pump impeller by generating response surface using design of experiment (DOE), i.e., to improve the total efficiency at design flowrate by changing incidence angle and exit blade angles. Table 2 shows their results i.e., comparison of optimized design with the base design.

2.2. Kriging Model (KRG). The KRG model [32] is one of the surrogate models which are being frequently used to apply in optimization problems either for single or multiobjective optimizations. The kriging (KRG) model in a geostatistics based approximation function which works on the weighted superposition of basic functions (Gaussian function). The KRG can be expressed as an unknown function $F(x)$ given by

$$F(x) = y(x) + m(x) \quad (5)$$

where $F(x)$ is an unknown to be estimated and $y(x)$ is known a global function usually a polynomial representing the trend over the design space and $m(x)$ represents a local deviation from the global model. The details can be found in Martin and Simpson [32].

The kriging model base optimization performed by Siddique et al. [33] shows improvement in total head rise by varying inlet blade angles, exit blade angles, and controlling the shape of a centrifugal pump impeller. Figure 2 is showing the Pareto optimal front obtained from KRG surrogate model with cluster points, and Table 3 shows CFD validation of those cluster points.

2.3. Radial Basis Neural Network (RBNN). The RBNN is a two-layered network (Chen et al. 1991) consisting of a hidden layer of radial basis neurons and an output layer of linear neurons. Such a network is characterized by a set of inputs and a set of outputs. The radial basis functions act as processing units between the input and output. The hidden layer performs a nonlinear transformation of the

TABLE 1: The optimization techniques and design parameters for centrifugal pump optimization presented by previous researchers.

Paper	Year	Optimization technique	Design parameters
Fischer K	1946	Experimental	Exit blade angles
Acosta and Bowerman	1956	Experimental	Exit and inlet blade angles
Varley F.A	1961	Experimental	Number of blades, exit blade and inlet blade angles of the impeller
Khlopenkov	1982	Experimental	Splitter blades, outlet blade angles of the impeller
Wahba and Tourlidakis	2001	Genetic algorithm assisted CFD	Bezier curves used to control impeller blade flow passage
Goto et al.	2002	Numerical and experimental	meridional shape of the impeller
Golcu et al.	2006	Experimental	Splitter length, number of blade
Luo et al.	2008	Numerical computation	Inlet blade angles
Ardizzon and Pavesi	2005	Numerical computation	Inlet blade angles, number of blades of the impeller
Kim et al.	2009	Surrogate assisted CFD	Sweep angle of hub, sweep angle of shroud, inlet and exit blade angles.
Savar et al.	2009	Experimental	Impeller trimming
Bonaiuti and Zangeneh	2009	Surrogate assisted CFD	Sweep angle, blade profile shape and axial length of the impeller
Liu et al.	2010	Numerical and experimental	Number of blades of the impeller
Westra et al.	2010	Experimental and CFD	Shape of inlet blade profile
Safikhani et al.	2011	Surrogate assisted CFD	Leading edge angle, trailing edge angle and stagger angle of the impeller
Li, W.G	2011	Numerical computation	Exit blade angle of the impeller
Kim and Kim	2012	Surrogate assisted CFD	vane length ratio, diffusion area ratio, angle at the diffuser van tip, and distance ratio between the impeller blade trailing edge and the diffuser vane leading edge
Shojaeefard et al.	2012	Numerical computation	Exit blade angle and width of the impeller
Zhou et al.	2012	Experimental and CFD	Different shapes of the diffuser
Sanda and Daniela	2012	Numerical computation	Number of blades, inlet and outlet blade angles of the impeller
Derakhshan et al.	2013	Surrogate and artificial bee colony algorithm assisted CFD	Hub diameter, suction diameter, impeller diameter, impeller width, inlet and outlet blade angles
Tan et al.	2014	Numerical computation	Wrap angle of the impeller
Zhang et al.	2014	Surrogate assisted CFD and experimental	Blade profile shape of the impeller
Yang et al.	2014	Numerical computation	Gap between impeller tip and volute tongue
Cavazzini et al.	2014	Numerical and experimental	splitter blade length
Zhang et al.	2015	Surrogate assisted CFD	Blade profile shape of the impeller
Pei et al.	2016	Surrogate assisted CFD	Shroud arc radius, hub arc radius, shroud angle and hub angles of the impeller
Wang et al.	2016	Surrogate assisted CFD	Inlet, wrap and exit blade angles of the impeller
Siddique et al.	2016	Surrogate assisted CFD	Inlet blade angles and blade passage profile
Xu et al.	2016	Surrogate assisted CFD	Blade wrap angle, blade angles at impeller inlet and outlet, blade leading edge position, and blade trailing edge lean
Bellary and Samad	2017	Surrogate assisted CFD	Inlet and exit blade angles of the impeller
Wang et al.	2015	Surrogate assisted CFD	Diffuser inlet diameter, inlet blade width, diffuser inlet angle and wrap angle
Guleren	2018	Genetic algorithm assisted CFD	Relative diffuser vane angle, number of diffuser vanes, number of impeller blades, and the impeller wrap angle

TABLE 2: Comparison of optimized design results with base design [31].

	β_{1h}	β_{1s}	β_2	Efficiency
Optimization model(CFD)	11	4.5	29	97.98
RSA estimated value	11	4.5	29	98.07
Base design model (CFD)	3	3	22	97.72

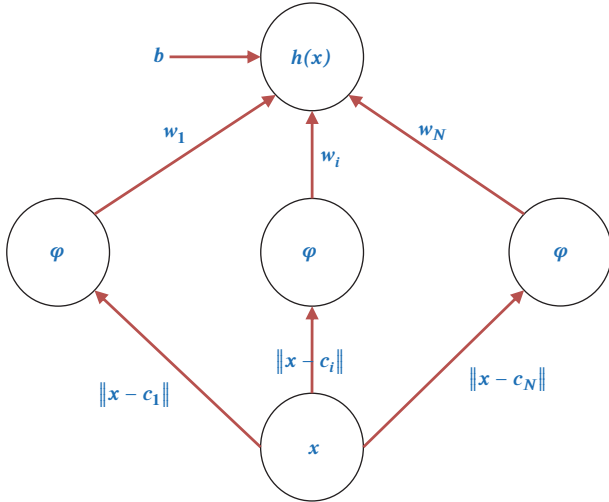


FIGURE 3: A radial basis neural network.

input space to an intermediate space using a set of radial basis units, the output layer, and then implements a linear combiner to produce the desired targets. Figure 3 shows a radial basis neural network design. Mathematically, the function approximation using radial basis neurons can be expressed as

$$h(\mathbf{x}) = \sum_{j=1}^N w_j \varphi_j \quad (6)$$

where $h(\mathbf{x})$ is the target function, φ is basis function, and N is the number of radial basis neurons. Generally, a bias term “ b ” is added to the weights in the linear layer. The basis function φ can be expressed as

$$\varphi = \exp\left(-\frac{(\mathbf{x} - c)^2}{r^2}\right) \quad (7)$$

where c is the center of the radial basis neuron and r is some parameter of the Gaussian function. The value predicted in the network is stored in the weights, obtained through training patterns. The network training is performed by using some suitable error estimation procedure. For example, the MATLAB function *newrb* depends on two parameters to design a RBNN network, the spread constant (Sc), and error goal (EG). The network training is performed by adjusting the cross-validation error by changing the spread constant (Sc). Usually, the error goal (EG) is set to default value (equal to 0). The main advantage of using the radial basis approach is the ability to reduce the computational cost owing to the linear nature of radial basis functions.

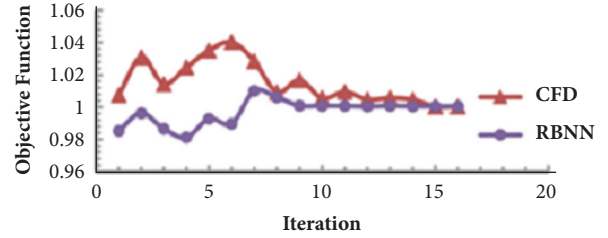


FIGURE 4: Convergence of surrogate model (RBNN) compared with CFD (Derakhshan et al. 2015).

The fast converging of surrogate based approximation depends on evenly distributed samples in the entire design space. Figure 4 shows the convergence of an approximate design solution predicted by surrogate model RBNN with the CFD results.

2.4. *Support Vector Machine (SVM)*. The SVM surrogate model is a supervised machine learning algorithm used for both classification as well regression. It was first introduced by Vapnik [38] and further extended by several researchers [39–42]. The SVM is primarily an informal method that performs classification tasks by constructing hyperplanes in a multidimensional space separated by different classes. This makes the SVM robust while handling sparse and noisy data.

2.5. *Weighted-Average Surrogate (WAS)*. A large number of design variables need a large number of sample designs, which increases the total optimization time. So, a surrogate base technique has been adopted by several researchers to mimic the high-fidelity model and give a reliable approximate optimum solution in a short period time [44–46]. Further, the reliability and robustness can be improved by using multiple surrogates as surrogates are problems dependent. Goel et al. [46] introduced a multiple surrogate techniques for handling problem from a different discipline which has improved the robustness and reliability of the surrogate approximation. Averaging the surrogate models can generate a new type of approximation model called weighted-average surrogate (WAS) model, which can reduce the effect caused due to bad surrogate predictions. There are different methods to find weights (w) for a surrogate [46]. One of the commonly used weights method is based on global data selection by considering the magnitude of the errors. This weighting scheme can be expressed as

$$w_i = \frac{\sum_{j=1, j \neq i}^m e_j}{(N-1) \sum_{j=1}^m e_j} \quad (8)$$

where e_j is the global database error measured at the j^{th} surrogate model. The best fitted surrogate models among the m^{th} models will give least error, i.e., e close to zero give weight to that surrogate close to 1.

3. Optimization Procedure

Design optimization is a method to solve design problems to obtain a superior design. The decision making for an

TABLE 3: Validation of surrogate predicted points (Siddique et al. 2017).

<i>Model</i>	<i>C.P</i>	η_{surr}	H_{surr}	η_{CFD}	H_{CFD}	$\eta_{CFD}-\eta_{POD}$	$H_{CFD}-H_{POD}$	RMSE
KRG	A	64.83	5.74	64.81	5.75	-0.02	0.01	0.01
	B	64.76	5.76	64.84	5.74	0.08	-0.02	0.06
	C	64.72	5.76	64.93	5.74	0.21	-0.02	0.15
	D	64.71	5.77	64.40	5.64	-0.31	-0.13	0.24
	E	64.55	5.78	64.43	5.64	-0.12	-0.15	0.13

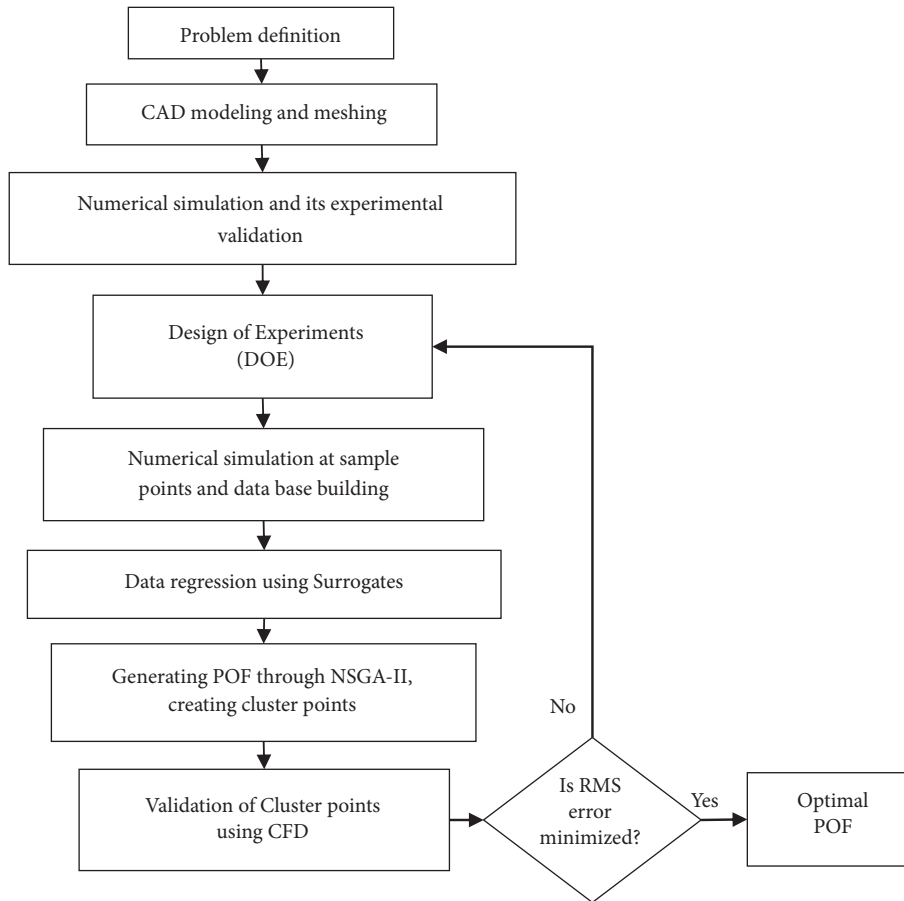


FIGURE 5: Flowchart of multiobjective optimization.

alternative design is based on engineering and economic feasibility. The procedure followed during surrogate based design optimization is shown through a flowchart in Figure 5. The first step is to define the problem statement which includes formulations of the problem, deciding the number of design variables, objective functions, and constraints if any. The design variables and their design space are created in design of experiment (DOE) step through literature survey and performing simulation at extreme design points. Later, sampling of designs and simulations to build data base are followed by CAD modeling, meshing, and numerical simulation validation. The database built from the responses of the sample design is used to train surrogates and a region of feasible solutions is obtained. These feasible solutions form a Pareto optimal front (POF), again validated at clustered

points. If the approximate POF points converge with the CFD results, then we get the final optimal POF or else, DOE step is repeated.

3.1. *Design of Experiment (DOE)*. The design of experiments (DOE) is the most important step in a surrogate based optimization method. The DOE helps to create a systematic method of determining the relationship between the objectives and variables. Sample designs are created within a design space to find responses of design variable to build response surface. Further, the response surface plots are used to obtain the optimum design point. There are different sampling techniques available in DOE such as random sampling, full factorial sampling, Latin hypercube sampling, and orthogonal sampling. Table 4 is showing design space and

TABLE 4: Design space and range selection for design variables [43].

Design variable	From(°)	To(°)	Selected values for modeling
γ	110	190	110, 130, 150, 170, 190
β_{lh}	60	89	60, 74.5, 89
β_{ls}	46	75	46, 60.5, 75
β_2	59	72	59, 65.5, 72

TABLE 5: Samples created using LHS [44].

S.No	β_2^o	$\Delta\beta^o$	γ^o
1	20.0	9.0	146
2	20.2	5.8	126
3	20.5	7.9	150
4	20.8	6.3	128
5	21.1	5.5	120
6	21.3	6.6	132
7	21.6	5.2	134
8	21.8	5.0	144
9	22.1	6.8	136
10	22.4	7.1	142
11	22.6	8.7	124
12	22.9	8.4	130
13	23.2	7.6	138
14	23.4	7.4	140
15	23.7	6.1	148

design levels for four different variables such as the wrap angle (γ), Inlet blade angle at hub (β_{lh}) at shroud (β_{ls}) and at exit (β_2). Further improvement in DOE is creating sample designs using Latin hypercube sampling method (LHS) which is a statistical method for generating random sample design from multidimensional distribution. The initial sampling size affects the distribution on surrogate construction using LHS sampling method [47, 48]. Table 5 shows random distributed sample designs for three variables such as exit blade angle (β_2), average inlet blade angle ($\Delta\beta$), and wrap angle (γ).

3.2. Multiobjective Optimization. The multiobjective optimization (MOO) problems deal with more than one objective function of which all may be simultaneously either minimized or maximized or one minimized and the other maximized. These types of problems often conflict with each other because improving one can degrade another. Therefore, for this type of problem, no single optimal solution can be the best for other objectives [30, 43]. For solving these types of problems where many solutions exist within the design space, a set of nondominated solutions known as Pareto optimal solutions is generated and the curve joining these solutions is known as Pareto optimal front (POF) [49].

The nondominated genetic algorithm (NSGA) was first used by Srinivas and Deb [50] for an MOO to search the feasible solution. The NSGA is an evolutionary search algorithm inspired by the biological evolution such as inheritance, mutation, selection, and crossover. The NSGA differs from

simple GA by the ways of selection operator works; the other operators such as crossover and mutation remain same. The limitations of using NSGA were its high computational complexity of nondominated sorting, lack of elitism, and the need for specifying the sharing parameter which increases further complexity. Later, the upgraded version NSGA-II is proposed by Deb et al. [51] which improves in finding the diverse set of solutions and converges quickly. NSGA-II replaces sharing function approach with a crowded comparison approach that eliminates the limitations of NSGA. The crowded comparison operator is defined after defining the density-estimation metric which is calculated by an average distance of two points on either side of the objective functions. The crowded comparison operator assists the selection process in every stage of the algorithm toward a uniformly spread out POF. NAGA-II also works better for the constrained based multiobjective optimization in view of solving practical problems.

4. Application of Surrogate in Centrifugal Pump Optimization

A set of papers contributed to design optimization of centrifugal pump to enhance their performances via surrogate models. Centrifugal pump impeller shape optimization by modifying inlet blade, exit blade, and wrap angles has shown improvement in the performance of pump. The performance improvement can be observed by both extending the blade leading edge and applying much larger blades angle. The larger inlet blade angle also improves the cavitation performance of the pump as shown in Figure 6 [34]. An investigation done by Bellary and Samad [52] shows that exit blade angle together with surface roughness influences the head, shaft power, and efficiency of the impeller while pumping different liquids. The wrap angle is also a sensitive parameter toward an objective function to maximize head when splitter blade is introduced in the flow passage [53]. By manipulating blade camber line using cubic Bezier curve changes blade loading coefficient and a smooth camber line guarantees improvement in the hydraulic performance of pump as shown in Figure 7 [35]. An investigation by Zhou et al. [54] shows the effects of different splitter blades on velocity distributions and pressure distributions along the flow channels and hydraulic performance of centrifugal pumps. Their result shows that a properly placed splitter blades by choosing suitable design factors can improve the flow in the pump and enhance its hydraulic performance.

Surrogate models used to optimize the shape of diffuser of a centrifugal pump were presented by [55–57]. Kim et al.

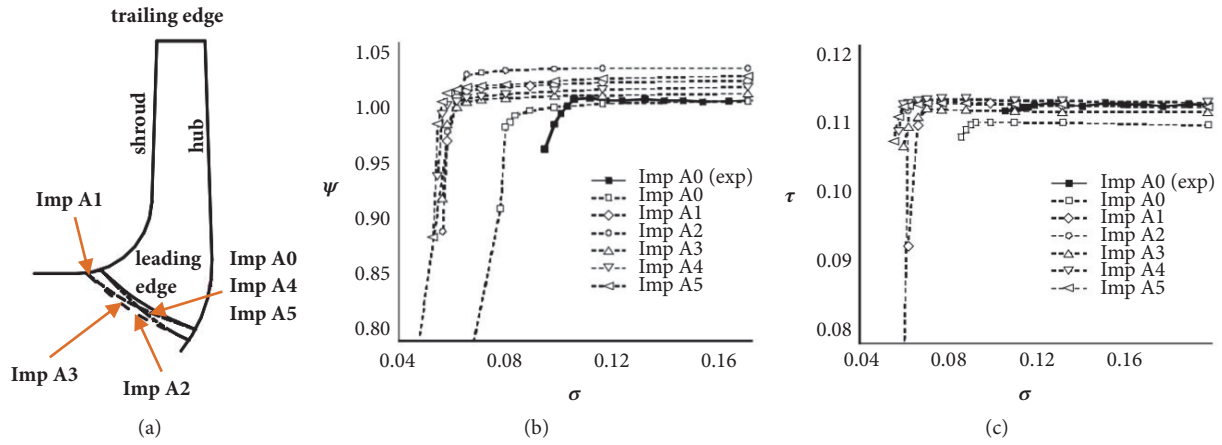


FIGURE 6: (a) Meridional configuration of test impellers; (b) and (c) cavitation performance for the test pump [34].

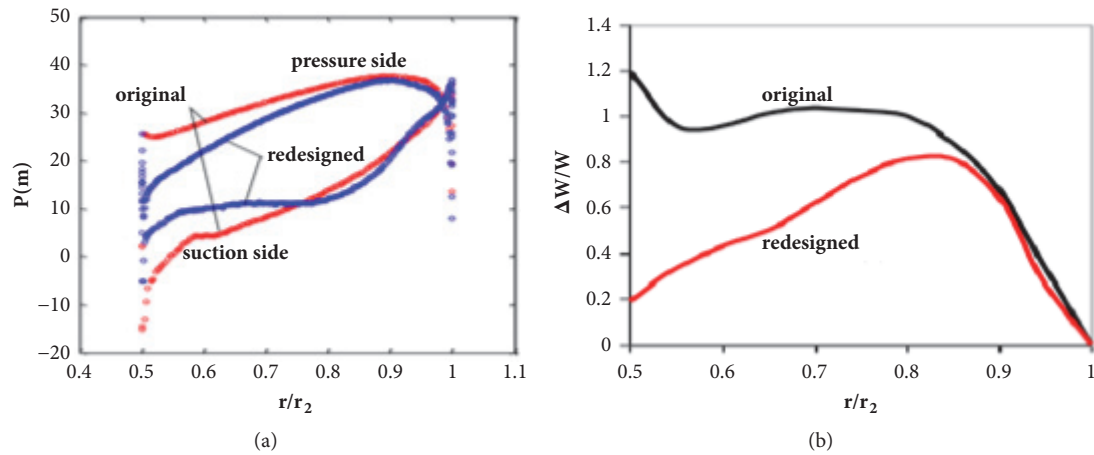


FIGURE 7: (a) Pressure (b) loading coefficient on blade surface of the original and redesigned impellers in mid-span [35].

[55] selected vane plane development as design parameters to improve the performance of pump using CFD and response surface methods. Kim and Kim [58] analyzed and optimized vaned diffuser in a mixed flow pump. The optimization process was based on radial basis neural network to enhance the performance of pump at high flow regions. The radial diffusers can improve the flow uniformity in pumps and affect the performance of centrifugal pump directly [57].

The pump performance is greatly affected by viscosity of the fluid pumped. In recent decades, the effect of surface roughness on the performance of centrifugal pump has been studied experimentally as well as numerically by several authors [5, 59–62]. Bellary and Samad [61] study on pumping crude oil using centrifugal pump shows that combined effect of an increase in exit blade angles and surface roughness can increase head with negligible increase in efficiency. The correlations developed using a polynomial regression (PR) model by Mrinal et al. [63] helped to predict the head and efficiency of centrifugal pump while pumping non-Newtonian slurries.

The surrogate based optimization has greatly improved the performance of low specific speed pumps such as axial,

centrifugal pumps for pumping blood [64–67]. A CFD and surrogate models based blood damage models for shear induced hemolysis were generated describing thrombosis potential and also helped design improvement [64]. Frazier et al. [66] study shows that the optimization using response surface has changed the pressure gradient at pump flowrates and improves normal flow imbalances between the pulmonary and systemic circulations. There is a great potential to improve the pump design used in cardiovascular systems using flow simulations assisted with surrogate models.

The several types of surrogate models used by previous authors have been summarized in Table 6. A series of researches was carried out using single and multiple surrogate models to improve the performance of the centrifugal pump.

5. Key Design Parameters

Previous researches show that there are several design parameters which can be used to optimize the performance of the centrifugal pump (Table 1). These parameters are either dependent or independent of each other and affect the pump performance. Also, there are few parameters which are

TABLE 6: Previous papers on application of surrogate for optimization of centrifugal pump.

Paper	Year	Contributions
Kim et al.	2009	Optimization of centrifugal pump impeller using response surface method and improved pump performance.
Safikhani et al.	2011	Optimized centrifugal pump using polynomial neural networks, multi-objective genetic algorithms.
Kim and Kim	2012	Optimized vaned diffuser design of a pump using radial basis neural network model.
Derakhshan et al.	2013	Optimized design of a centrifugal pump using artificial neural network and artificial bee colony algorithm.
Zhang et al.	2014	Optimization of a centrifugal pump vibration by integrating Kriging surrogate model, FSI simulation and experimental tests.
Pei et al.	2016	Optimized at three different flowrates using response surface function to improve performance of a centrifugal pump impeller.
Siddique et al.	2016	Optimized centrifugal pump using Kriging assisted computer based optimization to improve head and efficiency of a centrifugal pump.
Wang et al.	2016	Compared different surrogate models to optimize the centrifugal pump.
Bellary et al.	2016	Optimized two centrifugal pumps with different specifications with the help of multiple surrogate models.
Zhang et al.	2017	Optimization design of multiphase pump impeller based on combined genetic algorithm and boundary vortex flux diagnosis.
Wang et al.	2017	Optimization of the diffuser in a centrifugal pump by combining response surface method with multi-island genetic algorithm.
Shim et al.	2018	Kriging based approximation for optimizing three objective function to improve the performance of a centrifugal pump.
Mrinal et al.	2018	Polynomial regression model developed to predict head and efficiency of a centrifugal pump while pumping slurry.

highly sensitive to the objective function, while some are less sensitive. Shape optimization of impeller results in optimized shape with the highest efficiency without compromising the head or total pressure rise [68–71]. The various shape optimization parameters along with the objective functions are shown in Figure 8.

The inlet blade angles are one of the sensitive parameters which influence the performance of a pump Beveridge and Morelli [72]. The experimental investigation of the centrifugal pump using hydrodynamic and photographic technique was conducted by them to show the effect of inlet blade angles on the performance of the pump. The performance drop due to recirculation and shock losses at the eye of the impeller was studied by Acosta (1952). Later optimization by fixing exit blade angles and varying inlet blade angles was carried by Acosta and Bowerman [18] through experiments. They also presented performance drop due to the sudden entrance of fluid which causes recirculation. Ardizzon and Pavesi [73] presented an optimum incidence angle in centrifugal pumps using the theoretical method. The action of the counter-rotating vortex and of the blade camber was analyzed using an algorithm to evaluate an optimum incidence angle. The influence of Reynolds number is mild on the velocity profile due to inlet blade shape [33, 74].

The exit blade angle is an important design parameter which increases the peripheral velocity [17]. The work presented by ShojaeeFard and Boyaghchi [36] on the influence of outlet blade angle handling viscous fluids shows that the increase in exit blade angle improves performance centrifugal

pump handling viscous fluids (Figure 9). The impeller flow passage with large exit blade angle shows low separation near the blade which improves the performance of pumping viscous fluids [5, 36, 75].

The wrap angle affects the performance of pump in a similar way as the exit blade angle does. Modifying the shape of impellers by varying the wrap angle shows improvement of head and efficiency at higher wrap angles [15, 76].

The flow streamlines become uniform when a number of blades increase [77]. An increase in a number of the blades has both positive and negative effect [78, 79]. As the number of the blades increases, solidity increases, reducing efficiency due to the skin friction losses [80]. It also increases clogging at the inlet of the pump causing head and efficiency reduction [81]. Liu [79] study shows that, with the increase of blade number, the head of the model pumps increases. The cavitation characteristics are complicated and an optimum value of blade was shown for different cases. Jafarzadeh et al. [82] research shows that large number of blades improves the total head of the pump.

The impeller blade shape optimization using Bezier curve control point is a recently developed technique [83–89]. Bezier curve is parametric curve used to model smooth curves by controlling point between the start and the end of the curve. The angle of blade profile can be varied in any random way but for smooth variation, Bezier curve technique has been used which improved the performance of centrifugal pump [85].

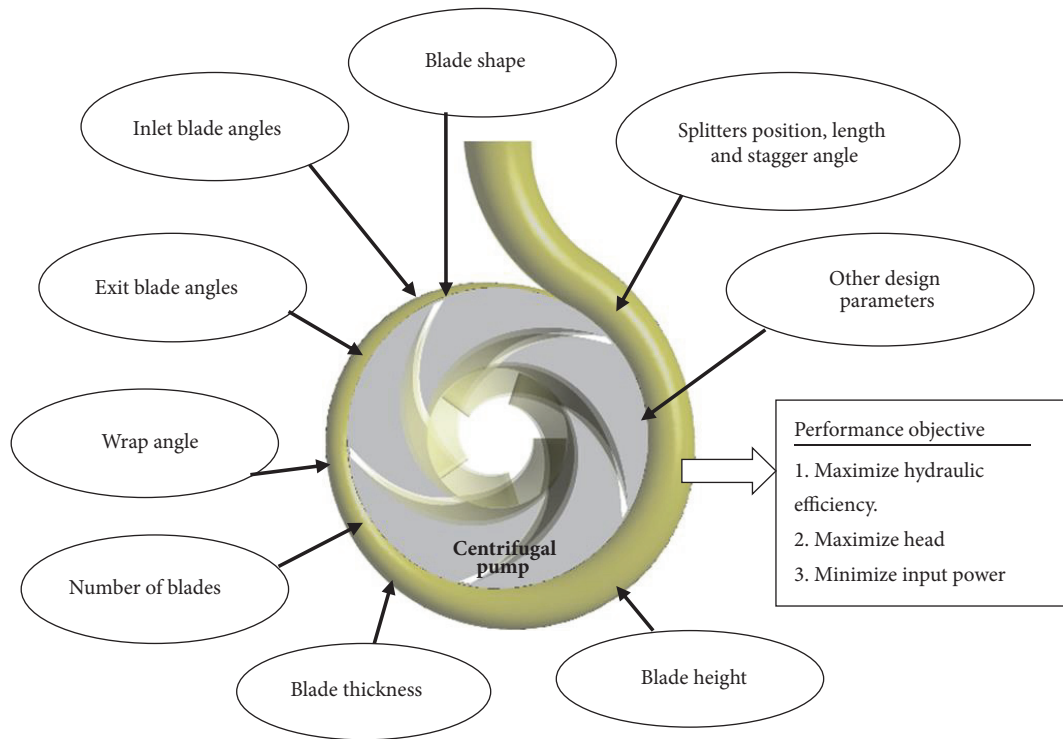


FIGURE 8: Centrifugal pump impeller design parameters and the objective functions.

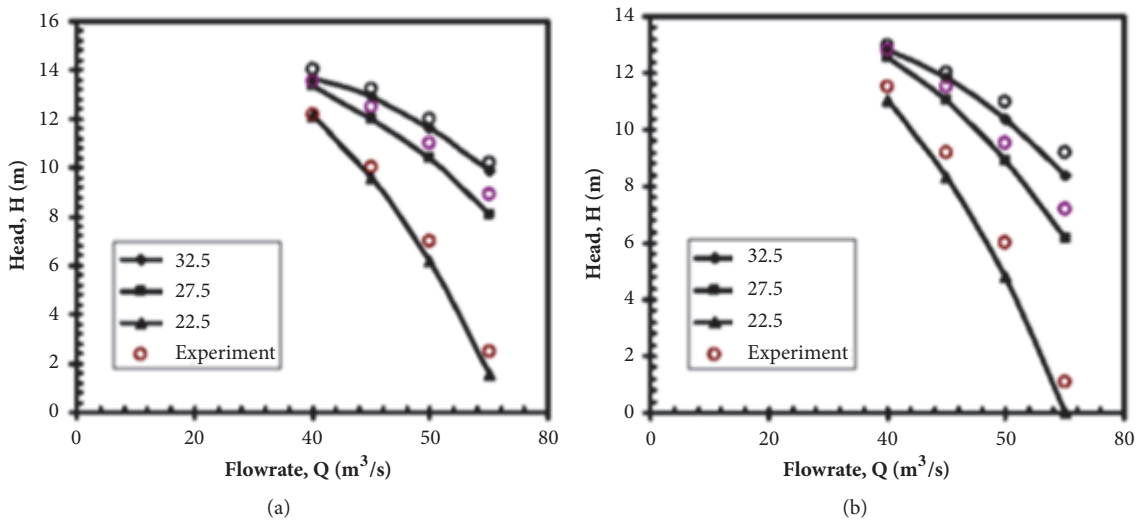


FIGURE 9: Influence of exit blade angles on performance of centrifugal pump handling (a) oil ($\nu = 43 \times 10^{-6} \text{ m}^2/\text{s}$) and (b) oil ($\nu = 62 \times 10^{-6} \text{ m}^2/\text{s}$) [36].

Miyamoto et al. [90] studied the effect of splitter blade on the flow and characteristics in the centrifugal impeller. In their study, both shrouded and unshrouded impeller was used to measure the flow properties using pressure probes. They observed that impeller with splitter blades has smaller blade loading and the absolute circumferential velocities and total pressures increased. Zangeneh et al. [91] presented a method for 3D inverse design of compressor impeller with splitters blades similar to the main blade at the mid-pitch

location. They observed that by controlling the circulation distribution on the splitter blades as well as the full blades allows a designer to optimize the geometry easily. Gölcü et al. [37] studied pump characteristics experimentally using a different number of blades with and without splitters on a deep well centrifugal pump. Their results show that the splitter blades cause negative effects on pump performance in impellers with 6 and 7 number of main blades whereas in the impeller having 5 main blades, the efficiency increases

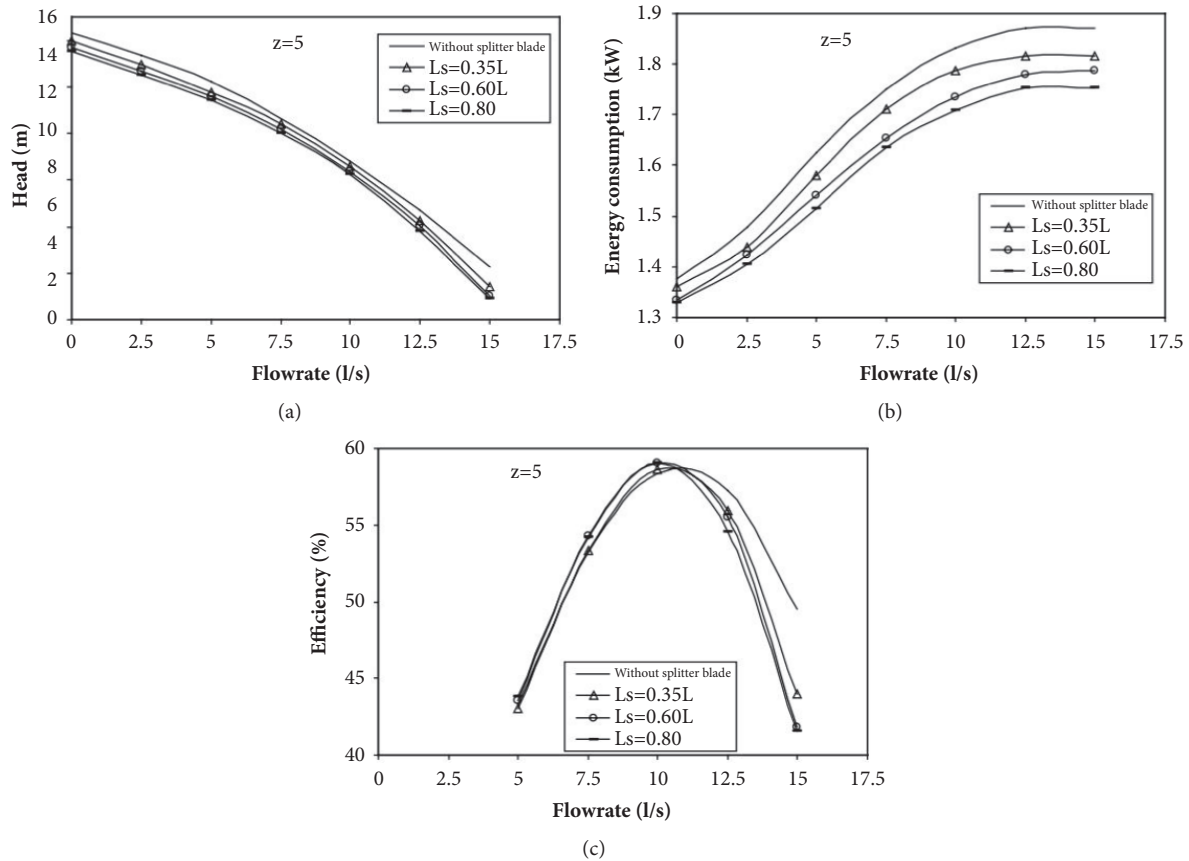


FIGURE 10: (a) Head versus flowrate, (b) energy consumption versus flowrate, and (c) efficiency versus flowrate of ($z=5$) [37].

with the increase of the splitter blade length to 50% of the main blade length (Figure 10). A similar study was done by Kergourlay et al. [92] to analyze the unsteady effect on the flow when adding splitter blades to the impeller. They observed that the impeller periphery velocities and pressures become more homogeneous. Adding splitters has a positive effect on the pressure fluctuations which decrease at the canal duct [93].

The other design parameters like radial gap between the impeller and the volute casing, diffuser inlet, and wrap angle have huge influences on the performance of the pump which has been investigated by several authors [89, 94–98]. Increasing the number of the diffuser vanes can significantly decrease the impeller blade pressure fluctuations [94].

6. Conclusions and Future Challenges

In this paper, design optimization of a centrifugal pump via surrogate models has been discussed. The surrogate assisted design optimization technique has reduced the total optimization time and cost which is evident from the research work by previous authors. The validation of low fidelity models through experiments and numerical simulations has increased surrogate prediction accuracy and robustness.

The turbomachines geometries like a centrifugal pump is a complex fluid domain where some design parameters are

sensitive, whereas others are insensitive toward a particular objective function. The extensive study on various design parameters which influences the performance of centrifugal pump has also been discussed. The blade profile shape of impeller, interaction of impeller, and casing geometry and the profile of vanned diffuser have a huge effect on the performance of pump. The combined effect of the above design parameters has not been studied yet. The use of splitter blades in the centrifugal pump for pumping viscous fluid has been rarely studied.

There are still challenges to improve the surrogate assisted design optimization technique and huge efforts are required. Individual surrogate models can be made effective with appropriate selection of design variable and design space. Handling large design parameters are still under research; the weighted-average surrogate use can improve the capability of this technique. Further improvement in CFD as well as in the surrogate models can improve the accuracy of searching the optimum design.

Nomenclature

Notations

- a: Linear constant
- e: Error

n: Number of design variables
 p: Pressure
 r: Radial distance
 w: Width
 x: Design variable
 y: Objective function.

Greek Symbols

α : Regression coefficient
 β : Blade angles
 γ : Wrap angle
 ψ : Head coefficient
 σ : Thoma's cavitation number
 τ : Power coefficient.

Subscripts

i, j : 1, 2, ...
 s: Shroud of impeller
 h: Hub of impeller.

Conflicts of Interest

The authors declare that there are no conflicts of interest regarding the publication of this paper.

References

- [1] D. Eckardt, "Detailed flow investigations within a high-speed centrifugal compressor impeller," *Journal of Turbomachinery*, vol. 98, no. 3, pp. 390–399, 1976.
- [2] M. Zangeneh, A. Goto, and H. Harada, "On the role of three-dimensional inverse design methods in turbomachinery shape optimization," *Proceedings of the Institution of Mechanical Engineers, Part C: Journal of Mechanical Engineering Science*, vol. 213, no. 1, pp. 27–42, 1999.
- [3] J. D. H. Kelder, R. J. H. Dijkers, B. P. M. Van Esch, and N. P. Kruyt, "Experimental and theoretical study of the flow in the volute of a low specific-speed pump," *Fluid Dynamics Research*, vol. 28, no. 4, pp. 267–280, 2001.
- [4] A. Goto, M. Nohmi, T. Sakurai, and Y. Sogawa, "Hydrodynamic design system for pumps based on 3-D CAD, CFD, and inverse design method," *Journal of Fluids Engineering*, vol. 124, no. 2, pp. 329–335, 2002.
- [5] W. Li, "Effects of blade exit angle and liquid viscosity on unsteady flow in centrifugal pumps," *Proceedings of the Institution of Mechanical Engineers, Part A: Journal of Power and Energy*, vol. 226, no. 4, pp. 580–599, 2011.
- [6] C. H. Liu, C. Vafidis, and J. H. Whitelaw, "Flow characteristics of a centrifugal pump," *Journal of Fluids Engineering*, vol. 116, no. 2, pp. 303–309, 2014.
- [7] J. Lu, S. Yuan, Y. Luo, J. Yuan, B. Zhou, and H. Sun, "Numerical and experimental investigation on the development of cavitation in a centrifugal pump," *Proceedings of the Institution of Mechanical Engineers, Part E: Journal of Process Mechanical Engineering*, vol. 230, no. 3, pp. 171–182, 2016.
- [8] W. Li, "Flow of viscous oil in the volute of a centrifugal pump," *Journal of Thermal Science*, vol. 11, no. 1, pp. 10–15, 2002.
- [9] W.-G. Li, "Effects of flow rate and viscosity on slip factor of centrifugal pump handling viscous oils," *International Journal of Rotating Machinery*, vol. 2013, Article ID 317473, 12 pages, 2013.
- [10] M. Šavar, H. Kozmar, and I. Sutlović, "Improving centrifugal pump efficiency by impeller trimming," *Desalination*, vol. 249, no. 2, pp. 654–659, 2009.
- [11] R. Spence and J. Amaral-Teixeira, "A CFD parametric study of geometrical variations on the pressure pulsations and performance characteristics of a centrifugal pump," *Computers & Fluids*, vol. 38, no. 6, pp. 1243–1257, 2009.
- [12] J. F. Gülich, *Centrifugal Pumps*, Springer Publications, Berlin, Germany, 2nd edition, 2010.
- [13] M. H. Shojaeefard, M. Tahani, M. B. Ehghaghi, H. Fallah Ardeshir, and M. Beglari, "Numerical study of the effects of some geometric characteristics of a centrifugal pump impeller that pumps a viscous fluid," *Computers & Fluids*, vol. 60, pp. 61–70, 2012.
- [14] R. Dong and J. Katz, "Relationship between unsteady flow, pressure fluctuations, and noise in a centrifugal pump—part B: effects of blade-tongue interactions," *Journal of Fluids Engineering*, vol. 117, no. 1, pp. 30–35, 1995.
- [15] L. Tan, B. Zhu, S. Cao, H. Bing, and Y. Wang, "Influence of blade wrap angle on centrifugal pump performance by numerical and experimental study," *Chinese Journal of Mechanical Engineering*, vol. 27, no. 1, pp. 171–177, 2014.
- [16] A. D. Scillitoe, P. G. Tucker, and P. Adami, "Numerical investigation of three-dimensional separation in an axial flow compressor: the influence of free-stream turbulence intensity and endwall boundary layer state," in *Proceedings of the ASME Turbo Expo 2016: Turbomachinery Technical Conference and Exposition*, p. V02DT44A025, Seoul, South Korea, 2016.
- [17] K. Fischer, *Investigation of Flow in a Centrifugal Pump*, 1946.
- [18] A. Acosta and R. Bowerman, "An experimental study of centrifugal pump impellers," *Transactions of the ASME*, vol. 79, no. 4, pp. 1821–1839, 1956.
- [19] L. Lebensztajn, C. A. R. Marretto, M. C. Costa, and J.-L. Coulomb, "Kriging: A useful tool for electromagnetic device optimization," *IEEE Transactions on Magnetics*, vol. 40, no. 2, pp. 1196–1199, 2004.
- [20] A. I. J. Forrester, A. Sobester, and A. J. Keane, *Engineering Design via Surrogate Modeling*, John Wiley & Sons, Ltd., UK, 1st edition, 2008.
- [21] A. Samad, K.-Y. Kim, T. Goel, R. T. Haftka, and W. Shyy, "Multiple surrogate modeling for axial compressor blade shape optimization," *Journal of Propulsion and Power*, vol. 24, no. 2, pp. 302–310, 2008.
- [22] R. Banos, C. Gil, J. Reça, and J. Martinez, "Implementation of scatter search for multi-objective optimization: a comparative study," *Computational Optimization and Applications*, vol. 42, no. 3, pp. 421–441, 2009.
- [23] J. Kim, J. Choi, and K. Kim, "Surrogate Modeling for Optimization of a Centrifugal Compressor Impeller," *The International Journal of Fluid Machinery and Systems*, vol. 3, no. 1, pp. 29–38, 2010.
- [24] D. Lim, Y. Jin, Y.-S. Ong, and B. Sendhoff, "Generalizing surrogate-assisted evolutionary computation," *IEEE Transactions on Evolutionary Computation*, vol. 14, no. 3, pp. 329–355, 2010.
- [25] J. Janusevskis and R. Le Riche, "Simultaneous kriging-based estimation and optimization of mean response," *Journal of Global Optimization*, vol. 55, no. 2, pp. 313–336, 2013.

- [26] K. Ezhilsabareesh, S. H. Rhee, and A. Samad, "Shape optimization of a bidirectional impulse turbine via surrogate models," *Engineering Applications of Computational Fluid Mechanics*, vol. 12, no. 1, pp. 1–12, 2018.
- [27] P. Halder, A. Samad, and D. Thévenin, "Improved design of a Wells turbine for higher operating range," *Journal of Renewable Energy*, vol. 106, pp. 122–134, 2017.
- [28] G. E. P. Box and K. B. Wilson, "On the experimental attainment of optimum conditions," *Journal of the Royal Statistical Society: Series B (Statistical Methodology)*, vol. 13, no. 1, pp. 1–45, 1951.
- [29] R. H. Myers and D. C. Montgomery, *Response Surface Methodology: Process and Product Optimization Using Designed Experiments*, John Wiley & Sons Ltd., Hoboken, NJ, USA, 1st edition, 1995.
- [30] W. A. Wahba and A. Tourlidakis, "A genetic algorithm applied to the design of blade profiles for centrifugal pump impellers," in *Proceedings of the 15th AIAA Computational Fluid Dynamics Conference 2001*, pp. 1–10, Anaheim, Calif, USA, June 2001.
- [31] S. Kim, Y. Choi, K. Lee, and J. Yoon, "Design Optimization of Centrifugal Pump Impellers in a Fixed Meridional Geometry using DOE," *The International Journal of Fluid Machinery and Systems*, vol. 2, no. 2, pp. 172–178, 2009.
- [32] J. D. Martin and T. W. Simpson, "Use of kriging models to approximate deterministic computer models," *AIAA Journal*, vol. 43, no. 4, pp. 853–863, 2005.
- [33] M. H. Siddique, K. R. Mrinal, and A. Samad, "Optimization of a centrifugal pump impeller by controlling blade profile parameters," in *Proceedings of the ASME Turbo Expo 2016: Turbomachinery Technical Conference and Exposition*, vol. 2C, pp. 1–8, Seoul, South Korea, 2016.
- [34] X. W. Luo, Y. Zhang, J. Peng, H. Xu, and W. Yu, "Impeller inlet geometry effect on performance improvement for centrifugal pumps," *Journal of Mechanical Science and Technology*, vol. 22, no. 10, pp. 1971–1976, 2008.
- [35] W. Li, "Inverse design of impeller blade of centrifugal pump with a singularity method," *Jordan Journal of Mechanical and Industrial Engineering*, vol. 5, pp. 119–128, 2011.
- [36] M. H. Shojaeefard and F. A. Boyaghchi, "Studies on the influence of various blade outlet angles in a centrifugal pump when handling viscous fluids," *American Journal of Applied Sciences*, vol. 4, no. 9, pp. 718–724, 2007.
- [37] M. Gölcü, Y. Pancar, and Y. Sekmen, "Energy saving in a deep well pump with splitter blade," *Energy Conversion and Management*, vol. 47, no. 5, pp. 638–651, 2006.
- [38] V. N. Vapnik, "An overview of statistical learning theory," *IEEE Transactions on Neural Networks and Learning Systems*, vol. 10, no. 5, pp. 988–999, 1999.
- [39] S. Tong and D. Koller, "Support vector machine active learning with applications to text classification," *The Journal of Machine Learning Research*, pp. 4–66, 2001.
- [40] I. Tsochantaridis, T. Hofmann, T. Joachims, and Y. Altun, "Support Vector Machine Learning for Interdependent and Structured Output Spaces," in *Proceedings of the Twenty-First International Conference*, p. 104, Banff, Alberta, Canada, July 2004.
- [41] L. Olatomiwa, S. Mekhilef, S. Shamshirband, K. Mohammadi, D. Petković, and C. Sudheer, "A support vector machine-firefly algorithm-based model for global solar radiation prediction," *Solar Energy*, vol. 115, pp. 632–644, 2015.
- [42] A. K. Shiba, T. Kaburagi, and Y. Kurihara, *Classification of State Transition by Using a Microwave Doppler Sensor for Wandering Detection*, vol. 11, 2017.
- [43] H. Safikhani, A. Khalkhali, and M. Farajpoor, "Pareto based multi-objective optimization of centrifugal pumps using CFD, neural networks and genetic algorithms," *Engineering Applications of Computational Fluid Mechanics*, vol. 5, no. 1, pp. 37–48, 2011.
- [44] W. Wang, J. Pei, S. Yuan, J. Zhang, J. Yuan, and C. Xu, "Application of different surrogate models on the optimization of centrifugal pump," *Journal of Mechanical Science and Technology*, vol. 30, no. 2, pp. 567–574, 2016.
- [45] N. V. Queipo, R. T. Haftka, W. Shyy, T. Goel, R. Vaidyanathan, and P. Kevin Tucker, "Surrogate-based analysis and optimization," *Progress in Aerospace Sciences*, vol. 41, no. 1, pp. 1–28, 2005.
- [46] T. Goel, R. T. Haftka, W. Shyy, and N. V. Queipo, "Ensemble of surrogates," *Structural and Multidisciplinary Optimization*, vol. 33, no. 3, pp. 199–216, 2007.
- [47] A. Afzal, K.-Y. Kim, and J.-W. Seo, "Effects of latin hypercube sampling on surrogate modeling and optimization," *The International Journal of Fluid Machinery and Systems*, vol. 10, no. 3, pp. 240–253, 2017.
- [48] H.-S. Shim, K.-Y. Kim, and Y.-S. Choi, "Three-objective optimization of a centrifugal pump to reduce flow recirculation and cavitation," *Journal of Fluids Engineering*, vol. 140, no. 9, p. 14, 2018.
- [49] D. Kalyanmoy, *Multi-objective Optimization Using Evolutionary Algorithms*, John Wiley & Sons Ltd., Chichester, England, 2nd edition, 2001.
- [50] N. Srinivas and K. Deb, "Multiobjective function optimization using nondominated sorting genetic algorithms," *Evolutionary Computation*, vol. 2, pp. 221–248, 1994.
- [51] K. Deb, A. Pratap, S. Agarwal, and T. Meyarivan, "A fast and elitist multiobjective genetic algorithm: NSGA-II," *IEEE Transactions on Evolutionary Computation*, vol. 6, no. 2, pp. 182–197, 2002.
- [52] S. A. Bellary and A. Samad, "Exit blade angle and roughness effect on centrifugal pump performance," in *Proceedings of the ASME 2013 Gas Turbine India Conference, GTINDIA '13*, pp. 1–10, Bangalore, India, December 2013.
- [53] L. Zhou, W. Shi, W. Lu, B. Hu, and S. Wu, "Numerical Investigations and Performance Experiments of a Deep-Well Centrifugal Pump With Different Diffusers," *Journal of Fluids Engineering*, vol. 134, no. 7, p. 071102, 2012.
- [54] X. Zhou, Y. X. Zhang, Z. L. Ji, and L. Chen, "Hydraulic design and performance analysis of low specific speed centrifugal pump," *IOP Conference Series: Earth and Environmental Science*, vol. 15, no. 3, p. 032023, 2012.
- [55] J. H. Kim, K. T. Oh, K. B. Pyun, C. K. Kim, Y. S. Choi, and J. Y. Yoon, "Design optimization of a centrifugal pump impeller and volute using computational fluid dynamics," *IOP Conference Series: Earth and Environmental Science*, vol. 15, no. 3, Article ID 032025, 2012.
- [56] S.-S. Hong, D.-J. Kim, J.-S. Kim, C. Choi, and J. Kim, "Study on inducer and impeller of a centrifugal pump for a rocket engine turbopump," *Proceedings of the Institution of Mechanical Engineers, Part C: Journal of Mechanical Engineering Science*, vol. 227, no. 2, pp. 311–319, 2013.
- [57] M. Tan, X. He, H. Liu, L. Dong, and X. Wu, "Design and analysis of a radial diffuser in a single-stage centrifugal pump," *Engineering Applications of Computational Fluid Mechanics*, vol. 10, no. 1, pp. 500–511, 2016.
- [58] J.-H. Kim and K.-Y. Kim, "Analysis and optimization of a vaned diffuser in a mixed flow pump to improve hydrodynamic

- performance,” *Journal of Fluids Engineering*, vol. 134, no. 7, Article ID 71104, 2012.
- [59] F. A. Varley, “Effects of Impeller Design and Surface Roughness on the Performance of Centrifugal Pumps,” *Proceedings of the Institution of Mechanical Engineers*, vol. 175, no. 1, pp. 955–989, 2006.
- [60] J. F. Gülich, “Effect of Reynolds number and surface roughness on the efficiency of centrifugal pumps,” *Journal of Fluids Engineering*, vol. 125, no. 4, p. 670, 2003.
- [61] S. A. I. Bellary and A. Samad, “Pumping crude oil by centrifugal impeller having different blade angles and surface roughness,” *Journal of Petroleum Exploration and Production Technology*, vol. 6, no. 1, pp. 117–127, 2015.
- [62] S. A. Bellary, R. Adhav, M. H. Siddique, B. Chon, F. Kenyery, and A. Samad, “Application of computational fluid dynamics and surrogate-coupled evolutionary computing to enhance centrifugal-pump performance,” *Engineering Applications of Computational Fluid Mechanics*, vol. 10, no. 1, pp. 171–181, 2016.
- [63] K. R. Mrinal, M. H. Siddique, and A. Samad, “Performance prediction of a centrifugal pump delivering non-Newtonian slurry,” *Particulate Science and Technology*, vol. 36, no. 1, pp. 38–45, 2018.
- [64] G. W. Burgreen, J. F. Antaki, Z. J. Wu, and A. J. Holmes, “Computational fluid dynamics as a development tool for rotary blood pumps,” *Artificial Organs*, vol. 25, no. 5, pp. 336–340, 2001.
- [65] A. L. Marsden, J. A. Feinstein, and C. A. Taylor, “A computational framework for derivative-free optimization of cardiovascular geometries,” *Computer Methods Applied Mechanics and Engineering*, vol. 197, no. 21–24, pp. 1890–1905, 2008.
- [66] O. H. Frazier, H. A. Khalil, R. J. Benkowski, and W. E. Cohn, “Optimization of axial-pump pressure sensitivity for a continuous-flow total artificial heart,” *The Journal of Heart and Lung Transplantation*, vol. 29, no. 6, pp. 687–691, 2010.
- [67] N. Uriel, A. P. Levin, G. T. Sayer et al., “Left ventricular decompression during speed optimization ramps in patients supported by continuous-flow left ventricular assist devices: Device-specific performance characteristics and impact on diagnostic algorithms,” *Journal of Cardiac Failure*, vol. 21, no. 10, pp. 785–791, 2015.
- [68] R. Hirschi, P. Dupont, F. Avellan, J. Favre, J. Guelich, and E. Parkinson, “Centrifugal pump performance drop due to leading edge cavitation: numerical predictions compared with model tests,” *Journal of Fluids Engineering*, vol. 120, no. 4, p. 705, 1998.
- [69] B. Sanda and C. V. Daniela, “The influence of the inlet angle over the radial impeller geometry design approach with ansys,” *Journal of Engineering Studies and Research*, vol. 18, pp. 32–39, 2012.
- [70] S. Derakhshan, M. Pourmahdavi, E. Abdollahnejad, A. Reihani, and A. Ojaghi, “Numerical shape optimization of a centrifugal pump impeller using artificial bee colony algorithm,” *Computers & Fluids*, vol. 81, pp. 145–151, 2013.
- [71] J. Pei, W. Wang, and S. Yuan, “Multi-point optimization on meridional shape of a centrifugal pump impeller for performance improvement,” *Journal of Mechanical Science and Technology*, vol. 30, no. 11, pp. 4949–4960, 2016.
- [72] J. H. Beveridge and D. A. Morelli, *Evaluation of a Two Dimensional Centrifugal Pump Impeller*, 1950.
- [73] G. Ardizzon and G. Pavesi, “Optimum incidence angle in centrifugal pumps and radial inflow turbines,” *Proceedings of the Institution of Mechanical Engineers, Part A: Journal of Power and Energy*, vol. 212, no. 2, pp. 97–107, 2005.
- [74] R. W. Westra, L. Broersma, K. van Andel, and N. P. Kruyt, “PIV measurements and CFD computations of secondary flow in a centrifugal pump impeller,” *Journal of Fluids Engineering*, vol. 132, no. 6, Article ID 061104, 2010.
- [75] S. A. I. Bellary and A. Samad, “An alternative approach to surrogate averaging for a centrifugal impeller shape optimisation,” *International Journal of Computer Aided Engineering and Technology (IJCAET)*, vol. 9, no. 1, pp. 62–83, 2017.
- [76] Y. Xu, L. Tan, S. Cao, and W. Qu, “Multiparameter and multiobjective optimization design of centrifugal pump based on orthogonal method,” *Proceedings of the Institution of Mechanical Engineers, Part C: Journal of Mechanical Engineering Science*, vol. 231, no. 14, pp. 2569–2579, 2016.
- [77] S. Murata, “Research on the flow in a centrifugal pump impeller,” *Bulletin of JSME*, vol. 5, no. 18, pp. 269–276, 1962.
- [78] M. Gölcü, N. Usta, and Y. Pancar, “Effects of Splitter Blades on Deep Well Pump Performance,” *Journal of Energy Resource Technology*, vol. 129, no. 3, p. 169, 2007.
- [79] H. Liu, “Effects of Blade Number on Characteristics of Centrifugal Pumps,” *Chinese Journal of Mechanical Engineering*, vol. 23, no. 06, p. 742, 2010.
- [80] W. Li, “Mechanism for Onset of Sudden-Rising Head Effect in Centrifugal Pump When Handling Viscous Oils,” *Journal of Fluids Engineering*, vol. 136, no. 7, p. 074501, 2014.
- [81] G. Cavazzini, G. Pavesi, A. Santolin, G. Ardizzon, and R. Lorenzi, “Using splitter blades to improve suction performance of centrifugal impeller pumps,” *Proceedings of the Institution of Mechanical Engineers, Part A: Journal of Power and Energy*, vol. 229, no. 3, pp. 309–323, 2015.
- [82] B. Jafarzadeh, A. Hajari, M. M. Alishahi, and M. H. Akbari, “The flow simulation of a low-specific-speed high-speed centrifugal pump,” *Applied Mathematical Modelling*, vol. 35, no. 1, pp. 242–249, 2011.
- [83] W. Li, “Blade exit angle effects on performance of a standard industrial centrifugal oil pump,” *Journal of Applied Fluid Mechanics*, vol. 4, pp. 105–119, 2011.
- [84] H. Cai and G. Wang, “A new method in highway route design: joining circular arcs by a single C-Bézier curve with shape parameter,” *Journal of Zhejiang University-SCIENCE A*, vol. 10, no. 4, pp. 562–569, 2009.
- [85] M. X. Chen, L. F. Tang, G. Zhou, Z. Y. Dou, X. L. Yang, and X. Y. Du, “Design and study on mortar pump’s impeller based on bezier and mechanical mechanics,” *Applied Mechanics and Materials*, vol. 327, pp. 215–221, 2013.
- [86] Y. Zhang, S. Hu, Y. Zhang, and L. Chen, “Optimization and Analysis of Centrifugal Pump considering Fluid-Structure Interaction,” *The Scientific World Journal*, vol. 2014, Article ID 131802, 2014.
- [87] Y. Zhang, S. Hu, J. Wu, Y. Zhang, and L. Chen, “Modeling and Multi-Objective Optimization of Double Suction Centrifugal Pump Based on Kriging Meta-models,” in *Advances in Global Optimization*, vol. 95, pp. 251–261, Springer International Publishing, 2015.
- [88] J. Zhang, S. Cai, Y. Li, X. Zhou, and Y. Zhang, “Optimization design of multiphase pump impeller based on combined genetic algorithm and boundary vortex flux diagnosis,” *Journal of Hydrodynamics*, vol. 29, no. 6, pp. 1023–1034, 2017.
- [89] W. Wang, S. Yuan, J. Pei, and J. Zhang, “Optimization of the diffuser in a centrifugal pump by combining response surface method with multi-island genetic algorithm,” *Proceedings of the Institution of Mechanical Engineers, Part E: Journal of Process Mechanical Engineering*, vol. 231, no. 2, pp. 191–201, 2017.

- [90] H. Miyamoto, Y. Nakashima, and H. Ohba, "Effects of splitter blades on the flows and characteristics in centrifugal impellers," *JSME International Journal*, vol. 35, no. 2, pp. 238–246, 1992.
- [91] M. Zangeneh, A. Goto, and H. Harada, "On the design criteria for suppression of secondary flows in centrifugal and mixed flow impellers," *Journal of Turbomachinery*, vol. 120, no. 4, pp. 723–735, 1998.
- [92] G. Kergourlay, M. Younsi, F. Bakir, and R. Rey, "Influence of splitter blades on the flow field of a centrifugal pump: test-analysis comparison," *International Journal of Rotating Machinery*, vol. 2007, Article ID 85024, 13 pages, 2007.
- [93] P. R. Khlopenkov, "Optimization of centrifugal pumps," *Hydrotechnical Construction*, vol. 16, no. 10, pp. 533–539, 1982.
- [94] N. Arndt, A. J. Acosta, C. E. Brennen, and T. K. Caughey, "Experimental investigation of rotor-stator interaction in a centrifugal pump with several vaned diffusers," *Journal of Turbomachinery*, vol. 112, no. 1, pp. 98–108, 1990.
- [95] D. Bonaiuti and M. Zangeneh, "On the Coupling of Inverse Design and Optimization Techniques for the Multiobjective, Multipoint Design of Turbomachinery Blades," *Journal of Turbomachinery*, vol. 131, no. 2, p. 021014, 2009.
- [96] S.-S. Yang, H.-L. Liu, F.-Y. Kong, B. Xia, and L.-W. Tan, "Effects of the radial gap between impeller tips and volute tongue influencing the performance and pressure pulsations of pump as turbine," *Journal of Fluids Engineering*, vol. 136, no. 5, Article ID 054501, 2014.
- [97] S. F. Xie, Y. Wang, Z. C. Liu, Z. T. Zhu, C. Ning, and L. F. Zhao, "Optimization of centrifugal pump cavitation performance based on CFD," *IOP Conference Series: Materials Science and Engineering*, vol. 72, no. 3, p. 032023, 2015.
- [98] K. M. Guleren, "Automatic optimization of a centrifugal pump based on impeller–diffuser interaction," *Proceedings of the Institution of Mechanical Engineers, Part A: Journal of Power and Energy*, pp. 1–15, 2018.